Fall 12-2017

Anodic Catalysts for Anion Exchange Membrane Fuel Cells

Aaron Joseph Roy
University of New Mexico - Main Campus

Recommended Citation

Roy, Aaron Joseph. "Anodic Catalysts for Anion Exchange Membrane Fuel Cells." (2017). https://digitalrepository.unm.edu/cbe_etds/71

Aaron J. Roy
Candidate

Chemical and Biological Engineering
Department

This dissertation is approved, and it is acceptable in quality and form for publication:

Approved by the Dissertation Committee:

Plamen Atanassov, Chairperson

Fernando H. Garzon

Ivana Gonzales

Svitlana Pylypenko

Anodic Catalysts for Anion Exchange Membrane Fuel Cells

by

Aaron Roy

B.S., Chemical Engineering, The University of New Mexico, 2011

M.S., Chemical Engineering, The University of New Mexico, 2013

DISSERTATION

Submitted in Partial Fulfillment of the
Requirements for the Degree of

Doctor of Philosophy
Engineering

The University of New Mexico
Albuquerque, New Mexico

December 2017

DEDICATION

Dedicated to my brothers, Jared and Greg.

ACKNOWLEDGMENTS

I would like to thank my academic advisor, Professor Plamen Atanassov, for his guidance and support throughout my academic and research pursuits. I also want to thank my committee members, Professor Fernando Garzon, Professor Ivana Gonzales, and Professor Svitlana Pylypenko, for their time, commitment, and most importantly for imparting upon me their extensive wisdom and experience.

Thank you to my colleagues and collaborators who have contributed substantially to this work: Professor Kateryna Artyushkova, Dr. Tristan Asset, Professor Alexey Serov, Dr. Ulises Martinez, Morteza Rezaei Talarposhti, Professor Ivana Gonzales, and Dr. Lok-kun Tsui.

ANODIC CATALYSTS FOR ANION EXCHANGE MEMBRANE FUEL CELLS

By

Aaron Roy

B.S., CHEMICAL ENGINEERING, THE UNIVERSITY OF NEW MEXICO, 2011

M.S., CHEMICAL ENGINEERING, THE UNIVERSITY OF NEW MEXICO, 2013

PH.D., ENGINEERING, THE UNIVERSITY OF NEW MEXICO, 2017

Abstract

With a limited availability of energy resources from petroleum and other fossil fuels, as well as growing concerns relating to the environmental implications of fossil fuel emissions, non-carbon fuels which can be utilized in proton and anion exchange membrane fuel cells (PEMFC’s/AEMFC’s), such as hydrogen and hydrazine hydrate (HH), are becoming more attractive as alternative fuels. Historically, platinum and platinum group metal catalysts (PGM) have been used as cathode and anode catalyst materials for both PEMFC’s and AEMFC’s. Although these catalysts are the highest performing catalysts available for the conversion of hydrogen energy in fuel cells, the limited availability and high costs of these materials make their commercialization prohibitive, and therefore the development of PGM-free catalysts, composed of inexpensive Earth-abundant materials, is needed.

Oxygen reduction reaction (ORR), which occurs at the cathode of AEMFC's and PEMFC's, typically requires larger amounts of catalyst due to the slow kinetics of ORR compared to hydrogen oxidation reaction (HOR). However, in the case of AEMFC's the kinetics of ORR are significantly more facile due to differing kinetic mechanisms in alkaline media. As a result, the development of PGM-free cathode catalysts for AEMFC's has been significant in recent decades, while the development of HOR and HH oxidation catalysts is still needed.

The most well-known and extensively studied anode catalyst for AEMFC's is nickel, due to the stability and intrinsic catalytic activity of Ni towards HOR in alkaline media. Based on this, the aim of the research described in this dissertation has been to tune the catalytic activity of Ni for HOR as well as HH oxidation in alkaline media to match the catalytic performance of PGM catalysts. It has been found that alloying Ni with secondary metals (Zn, Mo, and Cu), can tune the electronic environment of Ni in such a way which results in drastically improved catalytic activity towards anodic reactions in alkaline media. Additionally, the use of carbon support materials for Ni alloys has been found to provide the additional benefit of decreasing the mass transfer resistance of the catalyst. Presented in this dissertation are the results of this research.

Table of Contents

List of Figures

List of Tables

Chapter 1

Introduction – Non-Carbon Fuels for Alkaline Exchange Membrane Fuel Cells

The interest in fuel cells has been growing over the past decades as a response to the forecast depletion of fossil energies. Arguably of more immediate importance is related to the growing environmental and economic implications of fossil fuel emissions. Currently, significant efforts are underway to reduce emissions of greenhouse gasses, mainly CO_2, using renewable energy technologies such as wind and photovoltaics. However, the high demand for energy and the inability of such renewable energy technologies to provide on-demand power create a need for grid load-leveling. Therefore, the need for energy storage to more efficiently utilize renewable energy technologies is vast. Facing these challenges, one promising solution is hydrogen energy storage where energy generated by wind and photovoltaics can be stored by the electrolysis of water to generate H_2. Stored H_2 energy can then be consumed in hydrogen fuel cells as demand is needed. The hydrogen fuel cell is also an ideal technology for mobile power generation, such as automobiles, due to high energy conversion efficiency, and if the hydrogen is generated using renewables the net carbon emissions from such technologies is zero.

Indeed, fuel cells enable a more efficient fuel-to-electricity conversion than internal combustion engines. Low-temperature fuel cells are extremely promising technologies for a wide range of applications, such as portables electronic devices, electric vehicles, or stationary power supplies. However, they must overcome several challenges to become commercially viable. For example, the development of proton exchange membrane fuel cells (PEMFCs) and direct alcohol fuel cells (DAFCs) presents issues linked to the anodic and cathodic electrocatalysts. Their catalysts materials are typically based on Pd and Pt

[1,2], which implies cost and availability issues. Reducing the noble metal content in fuel cells is mandatory, and this can be achieved by (i) using tailored nanostructured materials, such as core-shell or alloy solid/hollow nanoparticles [3–8], or by (ii) focusing on non-noble materials. In that latter strategy, recent but nonetheless impressive progresses have been obtained with catalysts of the carbon-nitrogen-iron family for the oxygen reduction reaction (both in alkaline and acidic conditions) [9–12].

On the anode side, the most studied fuels to feed these systems still present drawbacks: hydrogen gas is expensive to produce in a sufficiently clean manner to store and transport, and there are still no active PGM-free catalysts capable to oxidize hydrogen efficiently. Oxygenated organic molecules (alcohols, aldehydes, organic acids, etc.) are easily produced, stored and transported, but their oxidation proceeds with very sluggish kinetics even on noble catalysts, adversely affecting the DAFC performances-to-catalyst cost ratio [1,2]. The choice of potential fuels is however wider in alkaline than in acidic medium, which enables potential fuels beyond molecular hydrogen and alcohols. In particular, non-carbon fuels of the boron (e.g. $NaBH_4$, NH_3BH_3) and nitrogen-derived family (N_2H_4) are of interest, owing to their large theoretical energy density, ease of storage/transport and faster overall oxidation kinetics than for their carbon-containing competitors [13–20].

By far, the largest obstacle in the commercialization of AEMFC's is the high cost of electrode materials. Therefore, it is of considerable interest to address the lack of PGM-free catalysts for hydrogen oxidation and hydrazine oxidation at the anode, replacing costly precious metals with low-cost and Earth abundant materials. In previous works [20], nickel metal alloys, specifically zinc, have demonstrated state-of-the-art activity towards hydrazine oxidation. Derived from this previous work, the objectives of this project were aimed at addressing the lack of PGM-free catalyst for AEMFC’s by further developing anodic nickel based catalysts alloyed with secondary metals (W, Mo, and Cu) to improve the activity of nickel towards anodic reactions in alkaline environments. To meet this objective, the project has been divided into three sub tasks. Firstly, the development of carbon supported Ni alloys at the laboratory scale to allow for the screening and selection of the most active formulations. Second, synthesis methods were optimized and tailored allowing for the commercial scale manufacture of the most active catalyst formulations. The final task was to integrate the most active formulations into anion exchange membrane electrode assemblies (MEA’s) to demonstrate state-of-the-art power density in a working device, where the initial target power density for HOR performed by a PGM-free anode was 100 $mWcm^2$.

Chapter 2

Methods

X-Ray Diffraction

The Ni catalyst crystal phase was characterized using X-ray diffraction. Diffraction patterns were obtained using a Rigaku Smartlab diffractometer equipped with a D-Tex Ultra silicon strip detector in Bragg-Brentano focusing geometry. Cu K-α was used as the X-ray source with a K-β receiving slit filter. The catalyst was mounted on a zero-background quartz holder and scanned from 10°-140° in 2θ at a scan rate of 7°/min. MDI JADE 2010 software was used to perform whole-pattern-refinement using phase data from the ICSD database as a reference.

Electron Microscopy

Transmission electron microscopy Transmission electron microscopy (TEM) as well as energy dispersive spectrometry (X-EDS) were performed on a JEOL 2010 microscope, equipped with a LaB6 filament and operated at 200 kV accelerating voltage (point-to-point resolution of 0.19 Å). The TEM micrographs were used to characterize the distribution of the metal nanoparticles on the carbon powder support and the particle sizes. The local or global Mo and Ni atomic percentages were determined by X-EDS using Oxford Inca control software. The acquisition was performed at the classical acceleration voltage of 200 kV on selected areas of the samples, over dozens (local analysis) to thousands (global analysis) of particles. The quantitative analyses were performed on Ni Ka and Mo Ka signal lines using the K factor provided by Oxford Inca software.

Scanning electron microscopy was performed on a Hitachi S-800 instrument using an accelerating voltage of 2 kV.

FTIR

The in situ FTIR (Fourier-Transform Infrared Spectroscopy) experiments were performed at room temperature, after activation in 1 M KOH (50 cyclic voltammetry between $0.5 < E < 0.7$ V vs. RHE at $v = 100$ mVs^{-1}), using a Nicolet 6700 spectrometer, bearing a MCT (mercury cadmium telluride) detector cooled with liquid nitrogen. The background spectrum was collected at $E = 0.17$ V vs. RHE. All the other spectra were taken during a 1 mVs^{-1} linear sweep voltammograms between $0.17 < E < 0.73$ V vs. RHE. The IR absorption spectra were calculated as $A = \log(R/R_0)$ where R and R_0 represent the reflected intensity corresponding to the sample and the reference beam, respectively. A Teflon cell was used for the in situ FTIR experiments, with a ZnSe hemisphere as the IR window, an Ag/AgCl in saturated KCl as the reference electrode, a platinum wire as the counter-electrode and a glassy carbon disk coated with 3 mL of the aqueous suspension of catalyst described above as the working-electrode. Similarly, to Ref. [26,48], the working electrode was pressed against the IR window, to form an electrolyte (0.1 M KOH + 0.5 wt. % hydrazine aqueous solution) layer of a few micrometers in thickness.

XPS

The X-ray photoelectron spectroscopy (XPS) analyses were performed using a Kratos AXIS-Ultra DLD photoelectron spec-trometer using a monochromatic Al Ka source operating at P = 225 W. No charge compensation was necessary. The survey of the sample was done first, followed by the recording of high-resolution spectra of C 1s, O 1s, Ni 2p and Mo 3d for three areas on the sample. All spectra processing was done in CasaXPS. Atomic % were calculated using sensitivity factors provided by the manufacturer. The inelastic mean free path for Ni 2p electrons with kinetic energy of 600 eV is 0.8 nm, while that for Mo 3d electrons with higher kinetic energy of 1250 eV is 1.6 nm. To calculate the atomic ratios for Mo and Ni coming from exactly the same depth, the relationship between the probability of a detected electron originating from a particular depth, d, and inelastic mean free path, l has been used: P(d) = exp(-d/l). Using this equation, the fractions of the total Ni 2p and Mo 3d signal at different depths were calculated. For example, at sampling depth of 1.6 nm, 95% of the Ni 2p electrons and 51% of Mo 3d electrons contribute to total signal. The atomic ratio of Ni/Mo at 1.6 nm is, thus, obtained by dividing the 0.95 Ni at. % by 0.51 Mo at%. The same was done for all other depths. Curve fitting was carried out using individual peaks of constrained width and shape. A 70% Gaussian/30% Lorentzian line shape was used for the curve-fits.

Three Electrode Cell Measurements

NiZn/Ketjenblack for Hydrazine Oxidation

UNM: Electrochemical analysis for synthesized catalysts was performed using the Pine Instrument Company electrochemical analysis system. The rotational speed reported was 1600 RPM, with a scan rate of 20 mVs^{-1}. The electrolyte was 1 M KOH (ACS grade, EMD) saturated in N_2 at 60°C. A platinum wire counter electrode and a Hg/HgO reference (1 M KOH) with used. Working electrodes were prepared by mixing 10 mg of the catalyst with 1.595 g Tetrahydrofuran (HPLC grade, Honeywell) with 315 mg anionic ionomer (2.0 wt.%, Tokuyama Corp.) The mixture was sonicated before 3 μL was applied onto a glassy carbon disk with a sectional area of 0.196 cm^2. The loading of catalyst on the electrode was 76.5 μgcm^{-2}.

NiMo/KB for Hydrazine Oxidation

All the electrochemical experiments were carried out in a three-electrode cell, using a Hg/HgO with 1 M KOH (measured at $E_{ref} = 0.905$ V vs. RHE) as reference, a platinum wire as counter- electrode and a Pine E5HT HotSpot glassy carbon rotating disk electrode as working electrode. The catalytic inks were prepared by mixing 10 mg of catalyst, 315 mg of ionomer solution (A3, Tokuyama corp.) and 1.595 mg of tetrahydrofuran (THF) solution. The thin-layer working electrodes were prepared by depositing 3 mL of this aqueous solution on the glassy carbon disk, yielding the desired thin-layer working electrode. All the catalysts were firstly activated in 1 M KOH by performing 50 cyclic voltammetry between $-0.5 < E < 0.7$ V vs. RHE at $v = 100$ mVs^{-1}. The electro-oxidation of hydrazine oxidation was performed in a 1 M KOH + 5 wt. % hydrazine electrolyte at $T = 333$ K. Cyclic voltammograms were performed between $0.5 < E < 0.7$ V vs. RHE at $v = 20$ mVs^{-1}.

NiMo/Ketjenblack for Hydrogen Oxidation

Electrochemical measurements were performed in 0.10 M NaOH electrolyte in a three-electrode glass cell thermostated at 25 °C using a Biologic SP-300 potentiostat. The counter electrode (Pt wire) and the reference electrode (Hg|HgO|0.10 M NaOH) compartments were connected to the working electrode compartment via a glass frit and a Luggin capillary, respectively. If not otherwise stated, all electrode potentials reported in the manuscript are referred to the reversible hydrogen electrode (RHE). Before each experiment, the glassware was cleaned by soaking in an H_2SO_4:H_2O_2 (1:1 v/v) mixture and then thoroughly washed with ultrapure water (ELGA, 18.2 MΩ cm, TOC < 2 ppb).

The electrocatalytic activity of NiMo/KB was measured using a thin film approach where a catalyst suspension in isopropanol (1.0 mg mL^{-1}) was drop-cast on a polished base of a glassy carbon (GC) rod (5 mm diameter) and dried under a gentle N_2 flow for 60 min. After immersion in the electrochemical cell and before measuring its electrocatalytic activity, the NiMo/KB electrode was conditioned by cycling in the potential interval from -0.20 to 0.40 V at a sweep rate (v) 20 mVs^{-1} in a N_2-saturated 0.1 M NaOH electrolyte in order to reduce Ni oxide species formed on the surface during the catalyst passivation and storage in air. The electrochemical surface area (ECSA) of Ni was estimated from the cyclic voltammetry (CV) curve obtained in the potential interval between -0.06 and 0.40 V at v = 20 mVs^{-1}. The entire value of the anodic charge corresponding to a monolayer α-Ni(OH)$_2$ formation and the 0.514 mCcm^{-2} conversion coefficient were considered after subtraction of the charge related to the Ketjenblack (KB) carbon support. The HOR exchange currents were derived from the anodic scans of linear sweep voltammograms obtained in H_2-saturated 0.1 M NaOH at the sweep rate of 5 mVs^{-1} in the potential interval between -0.06 and 0.40 V by the linearization of the micro polarization region.

NiCu/Ketjenblack-DENKA Black for Hydrogen Oxidation

Cyclic Voltammetry was performed in a 3-electrode cell consisting of a glassy carbon rotating disk electrode (RDE) as the working electrode, graphite counter electrode, and an eDAQ Hydroflex^{TM} reference electrode. Catalyst inks were prepared using 5 mg of catalyst, 150 μL of 0.5 wt.% Nafion in deionized water and 850 μL isopropyl alcohol. After sonication for 30 minutes, an appropriate loading of catalyst (100 μg, 200 μg, 300 μg, 400 μg, and 500 μg) was dispersed onto the RDE and allowed to air dry. Cyclic voltammetry tests were performed in 0.1M KOH solution saturated in N_2 or H_2 with a rotation speed of 425, 900, 1600, and 2500 RPM.

MEA

Membrane electrode assemblies (MEA) were prepared by the CCM method. 100 mg of the catalyst was combined with 0.96 ml of isopropanol, 0.24 ml of Tetrahydrofuran and 0.2 mL of a 2 wt.% anionic ionomer solution (Tokuyama Corp.). The ink was then sonicated for 5 min. After sonication, ZrO2 beads (Diameter = 2.0 mm, Nikkato) were added and the mixture was agitated for 15 min. The prepared ink was directly sprayed onto an anionic electrolyte membrane (Tokuyama Corp.) to form the catalyst electrode on the membrane. The membrane was then pressed for 5 min at room temperature to bind the catalyst layers to the membrane. Specific operating conditions can be found in later sections.

Ammonia Generation Experiments

The characterization of ammonia generation was performed by detection of NH_4+ by ion chromatography (881 Compact IC pro, Metrohm) in a fuel cell. The fuel cell conditions are the following: Anode: 2.6 $mgcm^{-2}$ of catalyst (NiMo supported on carbon) - ink: 100 mg of catalyst; 0.96 mL of IPA; 0.24 mL of THF; 0.2 mL of 5 wt. % A3 ionomer – sprayed directly on the membrane. Cathode: 1 $mgcm^{-2}$ - same ink process – Fe-AAPyr [49–52]. The anodic fuel (1 M KOH + 5 wt.% HH) was supplied at a 2 $mLmin^{-1}$, whereas air gas humidified at 323 K was provided at the cathode at a 500 $mLmin^{-1}$ flow rate.

Chapter 3

Introduction-Hydrazine Oxidation

In contrast to PEM hydrogen fueled vehicles development, researchers from Daihatsu Motor Co. have introduced the idea of an anion-exchange membrane fuel cell with liquid fuels [55-65]. Switching from acidic proton exchange to alkaline, anion-exchange membranes have many benefits, including fast fuel oxidation and oxygen reduction and possible use of cheaper non-platinum group metal catalysts as anode and cathode material for both sides of the MEA. The liquid fuel of choice was HH, which has no carbon atoms and thus will not contribute to increased CO_2 levels, the theoretical electromotive force is 1.56 V and it can be oxidized by number of inexpensive catalysts [66]. To meet the power output requirements of a stack with limited size, the anode material should provide the highest power density, be stable, and selective toward the production of water and nitrogen with no ammonia (NH_3) generation.

To realize this goal, NiZn and NiMo materials were selected for development in this application. Having known intrinsic activity for hydrogen and hydrazine oxidation, methods were developed to disperse NiZn/NiMo on conductive carbon supports to increase electrochemical surface area, and the alloy compositions of these materials were tuned to optimize the selectivity towards water and nitrogen generation in the case of hydrazine oxidation reaction.

Hydrazine Oxidation Mechanism

Hydrazine oxidation as a replacement for alcohol or hydrogen oxidation was extensively studied from the 1960’s to the present day [21–34].

$$\mathrm{N_2H_4 + 4OH^- \rightarrow N_2 + 4H_2O + 4e^-} \qquad \mathrm{E^0 = -0.33\ V\ vs. RHE} \qquad (1)$$

$$\mathrm{O_2 + 2H_2O + 4e^- \rightarrow 4OH^-} \qquad \mathrm{E^0 = 1.23\ V\ vs. RHE} \tag{2}$$

$$\mathrm{N_2H_4 + O_2 \rightarrow N_2 + 2H_2O} \qquad \mathrm{E^0 = 1.56\ V\ vs. RHE} \tag{3}$$

The DHFC (direct hydrazine fuel cell), which completes the oxygen reduction reaction at the cathode, also presents a higher theoretical cell voltage than PEMFC fed with hydrogen: 1.56 V vs. 1.23 V, owing to the very strong reducing behavior of its fuel (Eq. (1)). Insuring DHFCs efficiency is essential to enable their commercialization; in that sense, one should avoid the chemical decomposition of hydrazine into ammonia (NH_3, Eq. (4)), since it leads to incomplete fuel oxidation (lower faradic efficiency), poisoning of the anode catalyst by ammonia (and also of the cathode catalyst if ammonia cross-over proceeds through the membrane), all these phenomena decreasing the voltage and therefore the energy density of the DHFC [18].

$$\mathrm{N_2H_{4,ads} + 2H_2O \rightarrow 2OH_{ads} + 2NH_{3,ads}} \tag{4}$$

Sakamoto et al. [24,25,27] observed that alloying nickel with another metal (e.g. cobalt, lanthanum or zinc) improves the catalysts performances toward hydrazine oxidation, both in the rotating disk electrode (RDE) and membrane electrode assembly (MEA) configurations. For example, unsupported nickel nanoparticles in DHFC anodes combined with a Co-polypyrrole- catalyzed carbon cathode (Co-PPY-C) for the oxygen reduction reaction (ORR) presented a lower maximum power density (389 $mWcm^{-2}$) [24] than unsupported Ni_1Co_1 (423 $mWcm^{-2}$), unsupported Ni_9La_1 (453 $mWcm^{-2}$) and unsupported NiZn (synthesized by spray pyrolysis [26], 486 $mWcm^{-2}$) in identical operating conditions (T = 353 K, anolyte = 1 M KOH + 20% H_2O-N_2H_4). However, Daihatsu Motor Co. reported substantial ammonia production (from several hundred to several thousand ppm) on the catalysts listed above, which is unsuitable for widespread and durable DHFC applications [35]. Consequently, a major challenge for DHFC commercialization is to avoid hydrazine chemical decomposition without reducing the catalyst electrochemical performances (i.e. enable the selective and complete hydrazine oxidation of Eq. (1)). To this goal, one strategy is to investigate other elements that alloy with Ni. It has been shown that the presence of molybdenum in Ni-based catalyst influences their selectivity and efficiency toward several reactions [36, 37]. Based on this, the present study focuses on the synthesis of NixMoy/C catalysts and the analysis of the effect of molybdenum on the catalyst morphology and electrochemical performances.

Methods

Materials Synthesis – NiZn/Ketjenblack

NiZn catalysts supported on high surface area carbon for hydrazine electrooxidation were synthesized by solvent-free impregnation of nickel and zinc precursors by using a high-energy mechanochemical approach. A mechanochemical synthesis approach was selected due to the large volume of powder material attainable, compared to solvent-based impregnation methods requiring large liquid/slurry volumes and considerable time required for drying.

Calculated amounts of nickel and zinc nitrates, in order to achieve the composition of NiZn within the FCC solid solution region, were place in agate ball-mill jar with Ketjenblack (Akzo Nobel) powder. The mixture was ball milled 2.5 hours at 500 RPM. The well mixed material was reduced in 7 at. % H_2 gas (100ccm flow rate) for 4 hours at 450°C in a tube furnace reactor. After cooling down to room temperature, 1 at. % of O_2 was introduced into the furnace in order to prevent self-ignition of pyrophoric material.

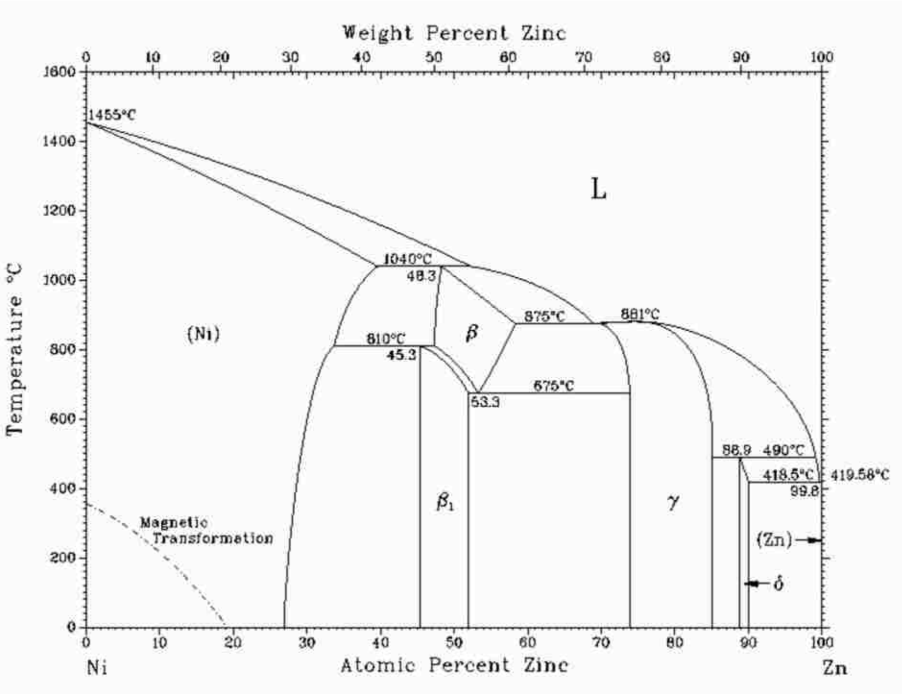

Figure 3.1: Phase diagram for NiZn system. http://www.pfonline.com/articles/a-comparative-study-of-gamma-phase-zinc-nickel-deposits-electroplated-from-various-alkaline-and-acid-systems

Materials Characterization

XRD

X-ray diffraction patterns for the NiZn catalysts are shown in Figure 3.2. Analysis revealed that all three catalysts consist of mainly $Ni_{87}Zn_{13}$ phase (abbreviated here as NiZn). A minor phase, identified as ZnO, was detected in the NiZn catalysts, resulting in various NiZn:ZnO ratios in the overall bulk composition: 85:15, 85:15, and 95:5 (20 wt.%, 40 wt.%, and 60 wt.%, respectively). The presence of zinc oxide in the catalysts can be explained by the extremely high oxophilicity of Zn metal. We observed that even controlled passivation of the reduced samples could not prevent oxide formation upon exposure to air. However, operation of the catalysts in the highly reductive environment of 20 wt.% of HH will lead to ZnO reduction.

MEAs post-mortem analysis is required in order to confirm this hypothesis. Calculation of the particle grain size by Scherrer analysis of the refined patterns gave an average particle domain size for all catalyst in the range of 10–15 nm.

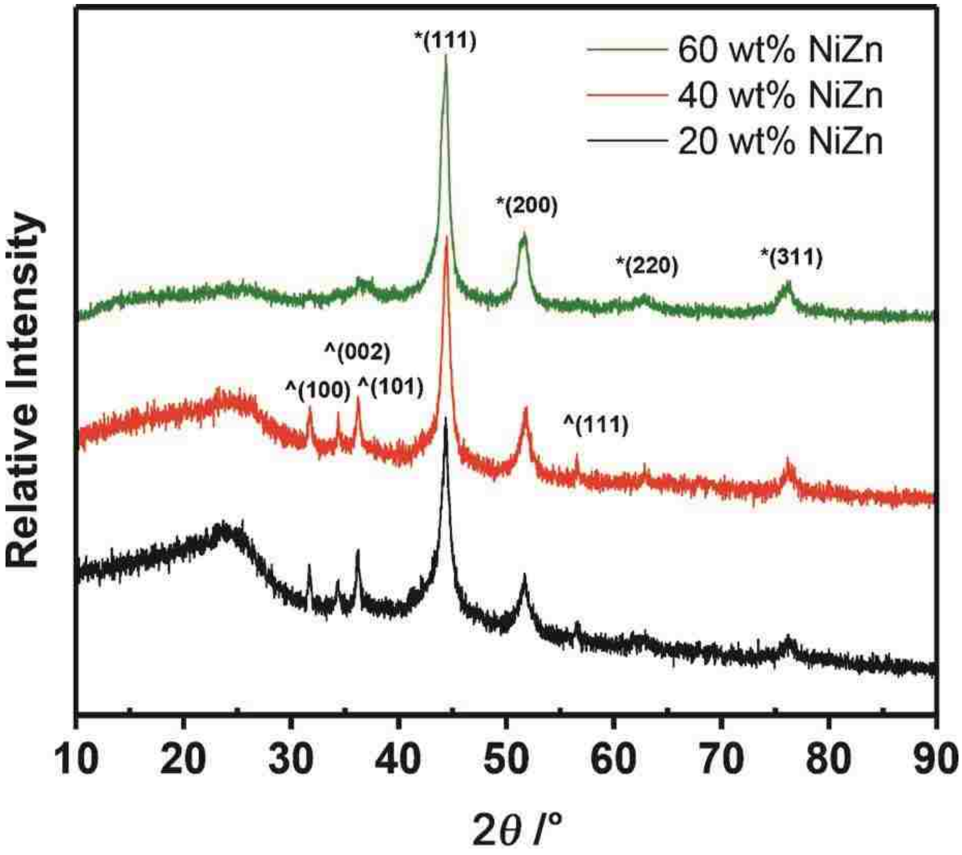

Figure 3.2: XRD data for NiZn catalysts with different loading synthesized by a mechanochemical method.

SEM/TEM

Morphological analysis by SEM and particle size distributions of the supported catalysts by TEM is shown in Figure 3.3 and Figure 3.4 D– F, respectively. SEM images revealed that catalysts preserved a morphology typical for materials synthesized on high surface area Ketjenblack carbons (Figure 3.3 A–C). From the TEM images it is observed that catalysts with 40 wt.% and 60 wt.% are evenly coated on the support surface without significant agglomeration. In the case of low loaded material with 20 wt.% of NiZn the surface was not fully covered, due to a high carbon-to-catalyst ratio (Figure 3.3 D–E). However, it was also confirmed that the catalyst is not agglomerated (Figure 3.3 D).

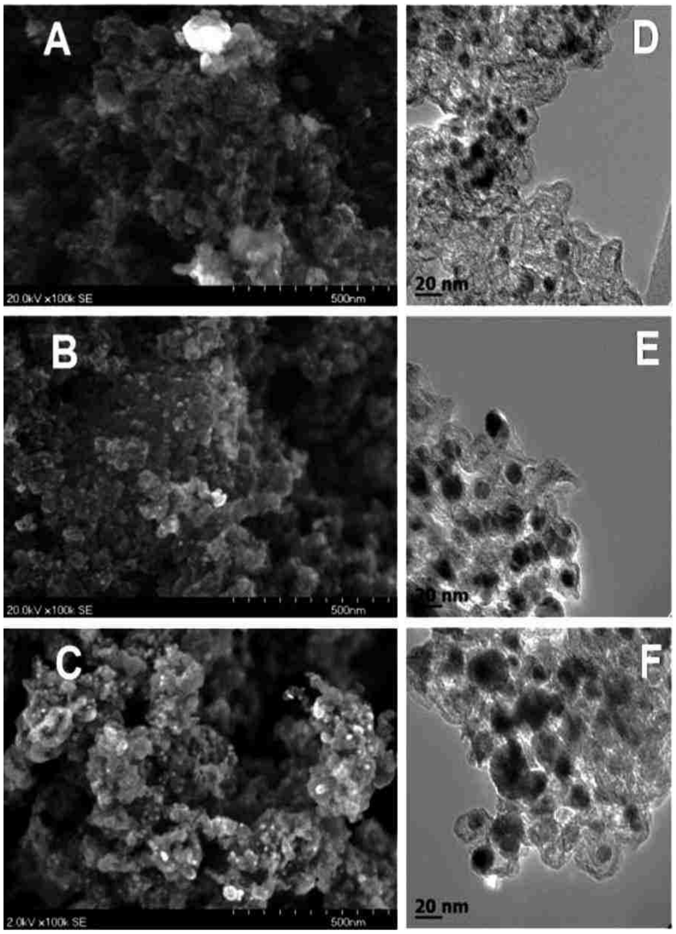

Figure 3.3: SEM (left) and TEM (right) images of $Ni_{87}Zn_{13}$/KB prepared by ball-milling with different loadings: 20 wt.% (A and D), 40 wt.% (B and E), and 60 wt.% (C and F).

The corresponding particle size distributions for the NiZn/KB catalysts are shown in Figure 3.4. These results show the influence of metal loading on the primary particle size of the NiZn alloy. Here, the particle size is shown to increase with increasing metal loadings with average primary particle sizes of 12 nm, 16 nm, and 18 nm for loadings corresponding to 20 wt. %, 40 wt.%, and 60 wt.% respectively. At the higher loading, 60 wt.%, the particle size distribution is skewed towards larger values which suggests agglomeration and sintering of the NiZn alloy due to a saturation of the support.

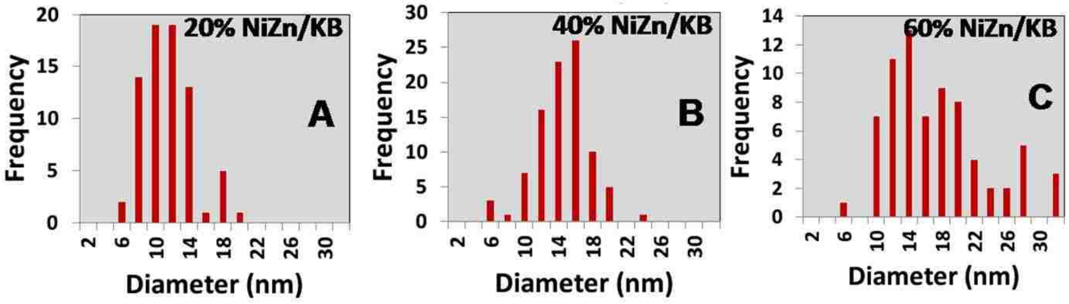

Figure 3.4: Particle size distributions measured from TEM data for NiZn/KB catalysts prepared by high energy ball milling.

Electrochemical Characterization

Hydrazine Oxidation – Cyclic Voltammetry

Previously our group has implemented a spray pyrolysis method for synthesis of unsupported NiZn electrocatalysts [59]. Figure 3.5 compares the electrochemical performance of the supported catalysts with spray-pyrolyzed nickel-based materials. It can be seen in Figure 3.5 that the supported catalysts possess higher overall mass activity and improved onset potential (ca. 0.14 V vs. RHE) compared to unsupported NiZn. Considering that the particle size for unsupported NiZn was in the range of 20–60 nm, the higher electrochemical activity of the NiZn/KB catalysts directly confirms the existence of a particle size distribution (PSD) effect. It is found that the 20 wt.% and 40 wt.% NiZn/KB catalysts have similar onset potentials and a peak activity of ca. 16000 Ag_{NiZn}^{1}, to our knowledge the highest mass activity of electrocatalysts for HH oxidation published.

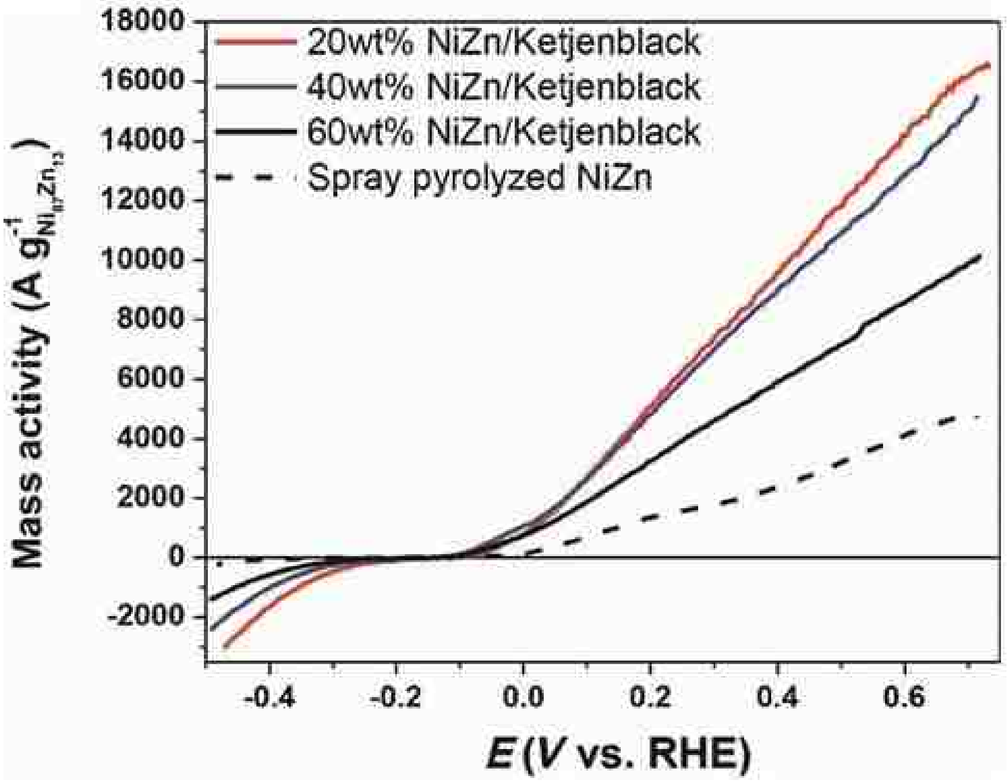

Figure 3.5: Cyclic voltammograms of NiZn catalysts with different metal loading compared to unsupported spray-pyrolyzed NiZn. Conditions: catalyst total loading 20 mg, 1M KOH, 5 wt.% hydrazine hydrate, 60 °C, N_2 purge, 1600 r.p.m.

MEA

To confirm the high activity of the supported NiZn/KB catalysts, single-cell MEA tests were performed with a Fe-aminoantipyrine-derived catalyst as cathode material synthesized by a sacrificial support method (SSM) [13–23]. Despite the fact the in RDE experiments 20 wt.% NiZn/KB had a slightly higher peak activity with respect to MEA building, the 60 wt.% catalyst was selected for fuel cell testing. The low density of 20 wt.% NiZn/KB results in a significantly thicker catalyst layer with poorly developed triple-phase boundary. Figure 3.6 compares the activities of a supported and an unsupported NiZn catalyst.

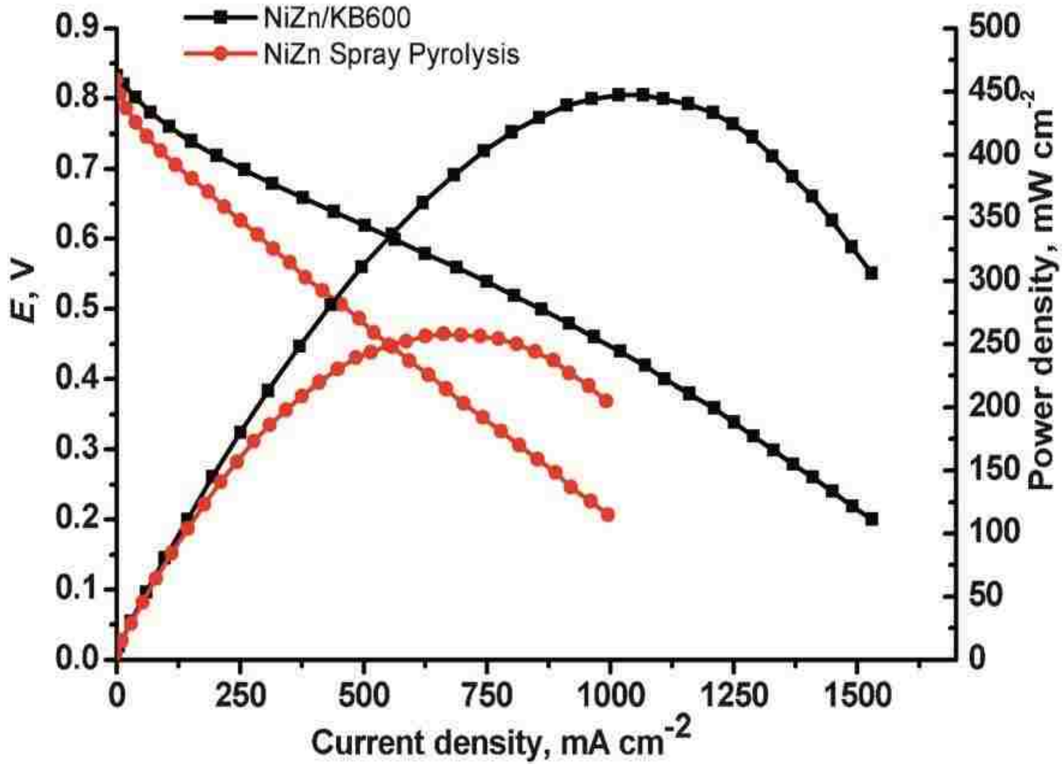

Figure 3.6: MEA performance of two different NiZn materials. Conditions: catalyst loading 2 mgcm^{-2} (anode), 1 mgcm^{2} (cathode); T_{cell} =80 °C, HH flow rate=2 mLmin^{-1} (20 wt%), air flow rate=500 cm^{3}-min^{-1}.

It is clear that a two-fold increase of activity in peak current density can be achieved by using carbon supports. The higher performance of NiZn/KB vs. NiZn in RDE tests can be explained by the particle size effect. However, in MEA tests the situation is more complex. Factors to consider include possible mass transfer limitations of HH to the active sites of the catalyst, the removal of gases from the catalytic layer, and possible interactions between ionomer and catalyst. Additionally, the unsupported catalyst has a surface area one order of magnitude less than NiZn/KB. The increase of surface area in supported materials results in an increased retention time of HH in contact with the active sites of the catalyst, resulting in an increase of power density [78]. It should be noted that peak current density for 60 wt.% NiZn/KB of 450 $mWcm^2$ (HH/air) is the highest ever reported.

Materials Synthesis - NiMo/C

Carbon-supported NiMo catalysts were synthesized using a wet impregnation procedure. First, calculated amounts of molybdenum precursor (Aldrich, $(NH_4)_6Mo_7O_{24}*4H_2O$), nickel precursor (Aldrich, $N_2NiO_6*6H_2O$) and urea (Aldrich CN_2H4_O) were dissolved in deionized water. Appropriate amounts were added to obtain a specific nickel/molybdenum ratio. The theoretical ratios synthesized by the wet impregnation process were: NiMo (1:1); NiMo (2:1); NiMo (3:1); NiMo (4:1); NiMo (9:1) and Ni. Since urea was added to reduce the molybdenum precursor, no urea was added during the synthesis of the pure nickel catalyst. A calculated amount of carbon (Akzo Nobel Ketjenblack EC-600 JD) was dispersed in H_2O + IPA (isopropyl alcohol), to obtain 50 wt. % metal loading. The metal precursors and the carbon powder were then mixed and dispersed using an ultrasonic probe for 5 min., before overnight drying at T = 358 K. This step was followed by 1 h heat-treatment at T = 823 K under 7 at. % H_2 atmosphere (balanced with Ar), with a 15 $Kmin^{-1}$ heating ramp, to complete the metal precursors reduction and form the NiMo alloys. After cooling, the catalyst was passivated by purging in argon followed 3 at. % O_2 at room temperature.

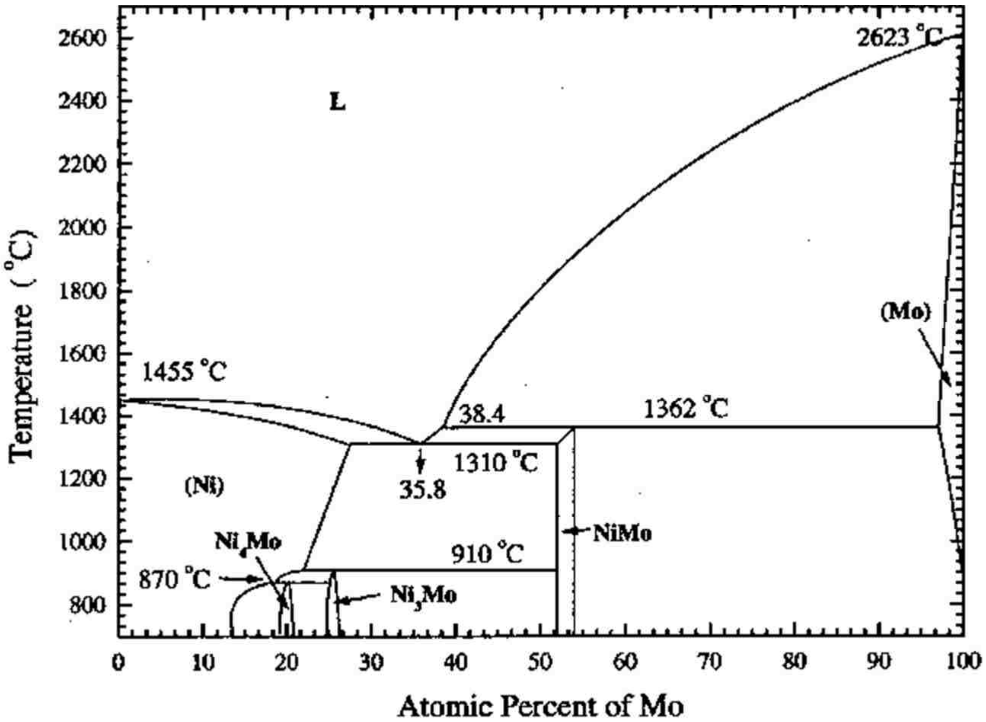

Figure 3.7: Phase Diagram for NiMo System [130].

Materials Characterization

TEM

The materials were then characterized in terms of morphology. Figure 3.8 displays representative TEM images of the synthesized NiMo/C materials. The distribution of the particles on the carbon support is homogeneous for Ni/C, NiMo (9:1)/C, NiMo (4:1)/C and NiMo (3:1)/C: only a few agglomerates could be detected (Figure 3.8 A-D). However, a clear particle distribution break-up is observed for NiMo (2:1)/C and NiMo (1:1)/C, for which two different particle sizes are observed (Figure 4.8 E-F), as well as the presence of large-sized amorphous MoO_2 structures (Figure 3.8 E-F).

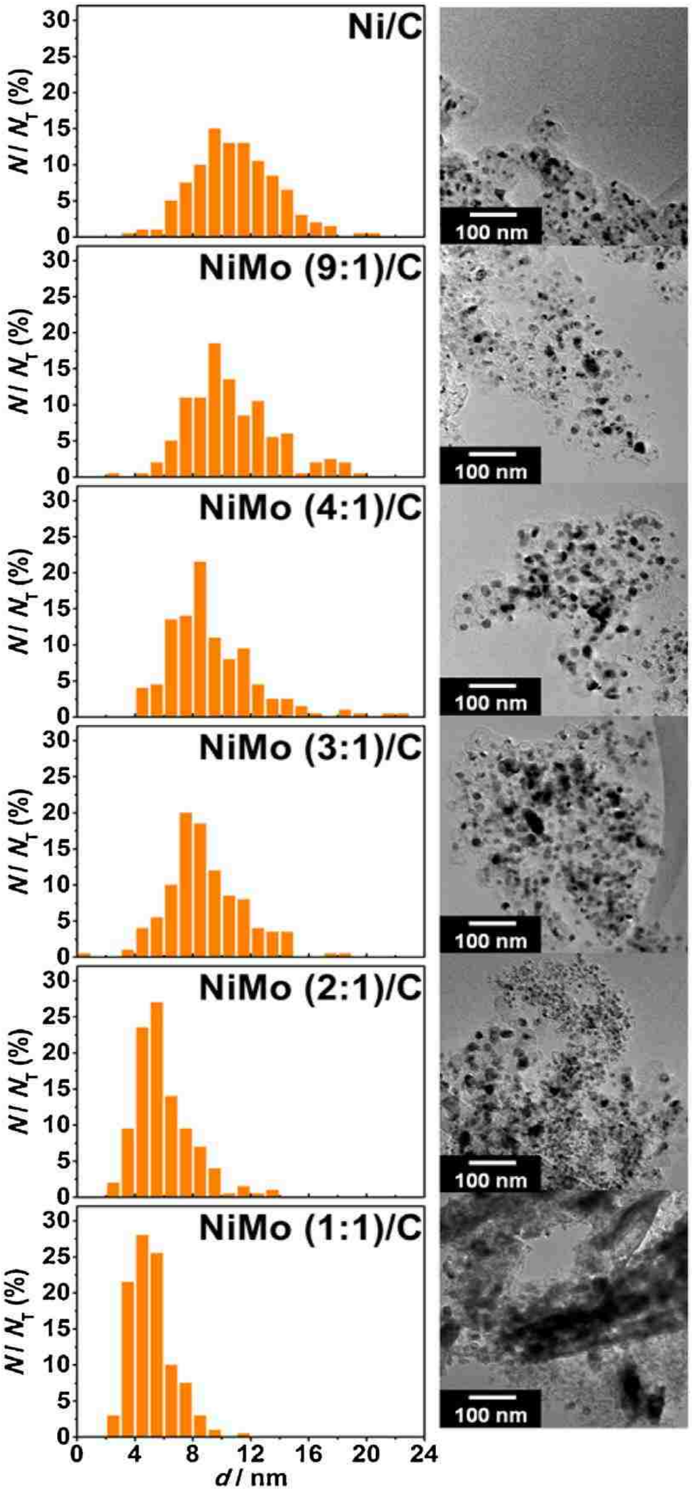

Figure 3.8: Representative TEM pictures and particle size distributions for the NiMo/C electrocatalysts synthesized in this study.

In addition to calculating the number average particle diameter, the particle size distributions were also normalized by particle volume. Normalization by particle volume is informative due to the presence of two solid solutions found in each of the NiMo/C catalysts, Ni-rich and Mo-rich, and is discussed in further detail in later sections (see XRD characterization Figure 3.10 and Table 3.1). The volume normalized particle size distributions also allow for the calculation of the specific surface area, m^2g^{-1} of metal, of the electrocatalysts as shown in Table 3.6.

Table 3.1 Average particle size and standard deviation calculated from TEM images. Data were normalized to the number average as well as volume average particle diameter.

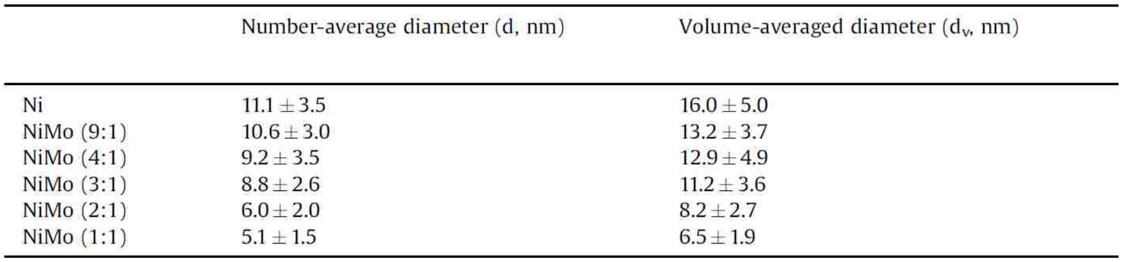

	Number-average diameter (d, nm)	Volume-averaged diameter (d_v, nm)
Ni	11.1 ± 3.5	16.0 ± 5.0
NiMo (9:1)	10.6 ± 3.0	13.2 ± 3.7
NiMo (4:1)	9.2 ± 3.5	12.9 ± 4.9
NiMo (3:1)	8.8 ± 2.6	11.2 ± 3.6
NiMo (2:1)	6.0 ± 2.0	8.2 ± 2.7
NiMo (1:1)	5.1 ± 1.5	6.5 ± 1.9

X-EDS

The local distribution of Ni and Mo in the synthesized electrocatalysts was examined with X-EDS analyses. One must be aware that atomic compositions determined with X-EDS strongly depend on the thickness of the probed area. whatever this bias, the EDS spectra for each region shown in Figure 3.9 were analyzed and the local elemental compositions were determined (Table 3.2). The results tend to show heterogeneous atomic composition from one particle to the other. Based on these elemental compositions, it became evident that the distribution of Ni and Mo followed a trend where the composition of the alloy can be described as bimodal, indicating the presence of two solid solutions: a Ni-rich solid solution and a Mo-rich solid solution. These data are further corroborated by phase composition determined by XRD pattern refinement (Figure 3.10).

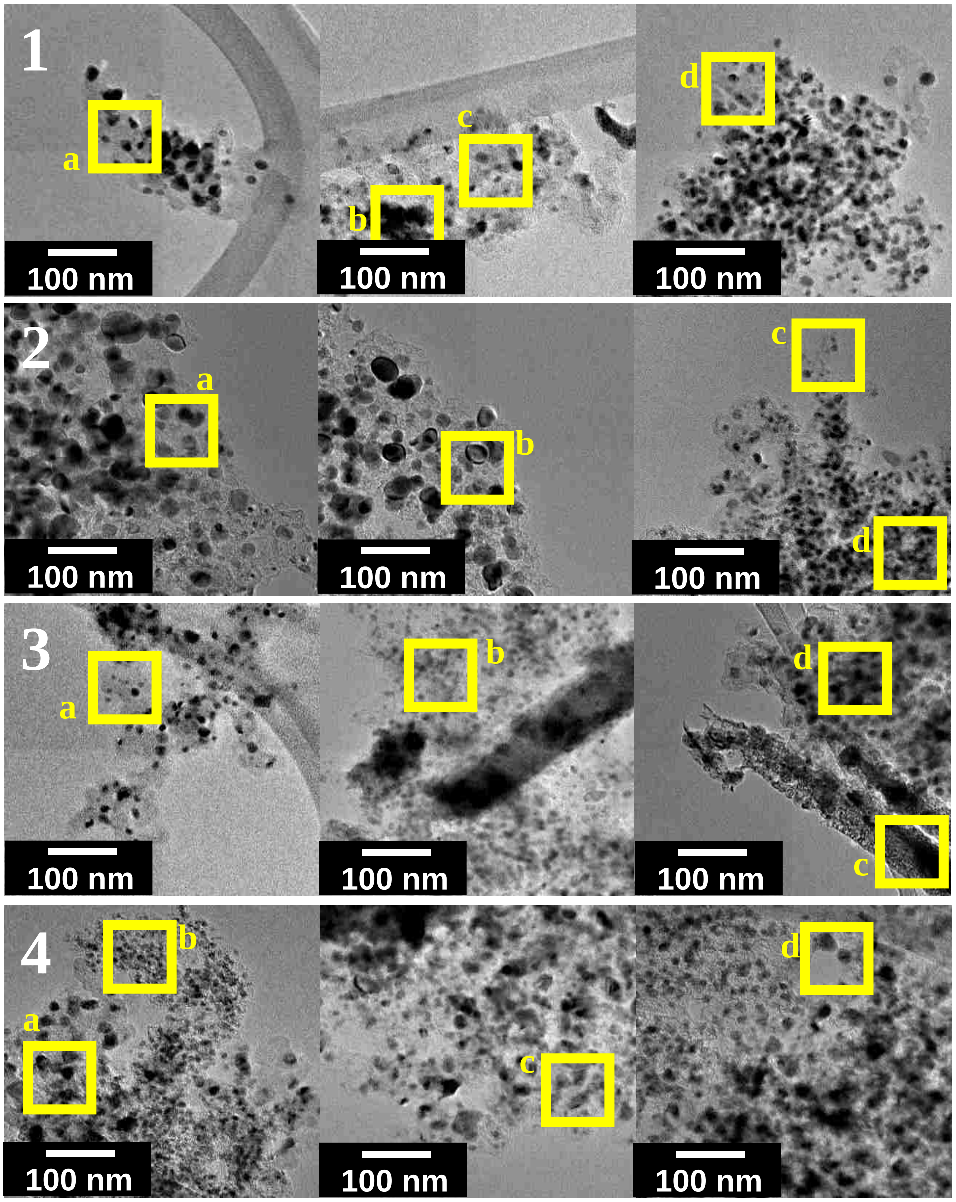

Figure 3.9: TEM pictures used for TEM – X-EDS analysis on (1) NiMo (9:1)/C, (2) NiMo (4:1)/C, (3) NiMo (3:1)/C and (4) NiMo (2:1)/C. The letters correspond to the regions probed with X-EDS and the atomic compositions are presented in Table 3.2.

Table 3.2 : X-EDS evaluation of the nickel and molybdenum content for specific regions of the synthesized NiMo/C electrocatalysts.

		X-EDS
(1) NiMo (9:1)	*a.*	$Ni_{0.95}Mo_{0.05}$
	b.	$Ni_{0.62}Mo_{0.38}$
	c.	$Ni_{0.84}Mo_{0.14}$
	d.	$Ni_{0.97}Mo_{0.03}$
(2) NiMo (4:1)	*a.*	Ni
	b.	Ni
	c.	$Ni_{0.91}Mo_{0.09}$
	d.	$Ni_{0.75}Mo_{0.25}$
(3) NiMo (3:1)	*a.*	$Ni_{0.96}Mo_{0.04}$
	b.	$Ni_{0.91}Mo_{0.09}$
	c.	$Ni_{0.51}Mo_{0.49}$
	d.	$Ni_{0.76}Mo_{0.24}$
(4) NiMo (2:1)	*a.*	$Ni_{0.74}Mo_{0.26}$
	b.	$Ni_{0.50}Mo_{0.50}$
	c.	$Ni_{0.71}Mo_{0.29}$
	d.	$Ni_{0.59}Mo_{0.41}$
NiMo (1:1)		$Ni_{0.50}Mo_{0.50}$
		$Ni_{0.37}Mo_{0.63}$
		$Ni_{0.32}Mo_{0.68}$
		$Ni_{0.42}Mo_{0.58}$

XRD

According to the XRD analyses, Figure 3.10, the compositions of these phases are close to (i) the $(Ni_9Mo)_{0.4}$ solid solution for the Ni-rich and (ii) the $Ni_{0.16}Mo_{0.84}$ solid solution for the Mo-rich. A slight expansion of the lattice constant a (see Table 4.4) was observed compared to $(Ni_9Mo)_{0.4}$ and $Ni_{0.16}Mo_{0.84}$ (i.e. for NiMo (1:1) the experimental and theoretical lattice constants for the $(Ni_9Mo)_{0.4}$ and the $Ni_{0.16}Mo_{0.84}$ phases are 0.356 nm vs. 0.352 nm and 0.423 nm vs. 0.417 nm, respectively). This expansion of the lattice constant demonstrates a higher molybdenum content in the Ni-rich and Mo-rich solid solutions than assumed considering the composition of the pure $(Ni_9Mo)_{0.4}$ and $Ni_{0.16}Mo_{0.84}$ solid solutions.

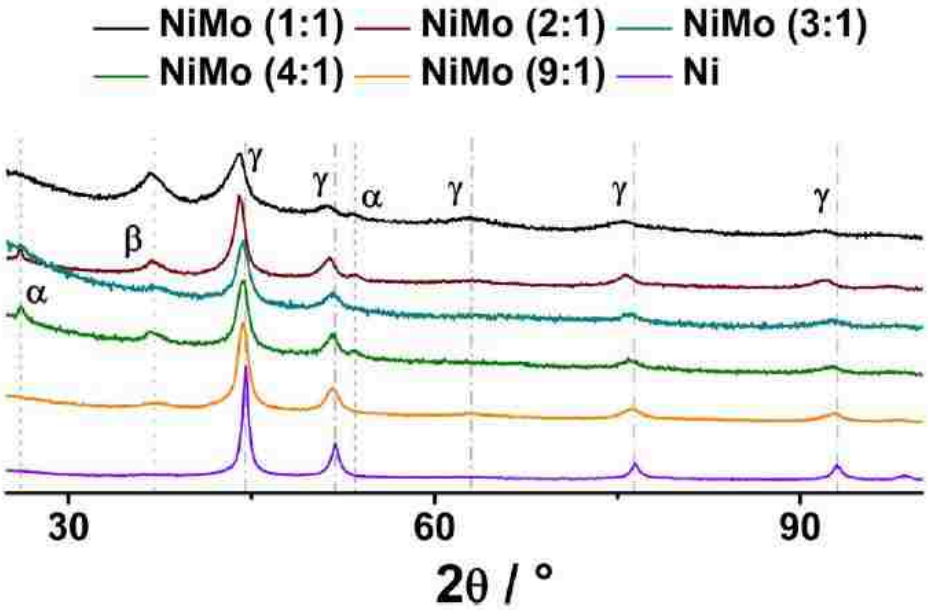

Figure 3.10: XRD patterns of the NiMo/KB electrocatalysts with the peaks for (α) MoO_2, (β) $Ni_{0.16}Mo0.84$ and (γ) $(Ni_9Mo)_{0.4}$.

Table 3.3 Elemental and phases composition determined by X-ray diffraction for the NiMo/C electrocatalysts synthesized in this study. The atomic ratio between brackets is the stoichiometry in the initial metal salt precursor solution.

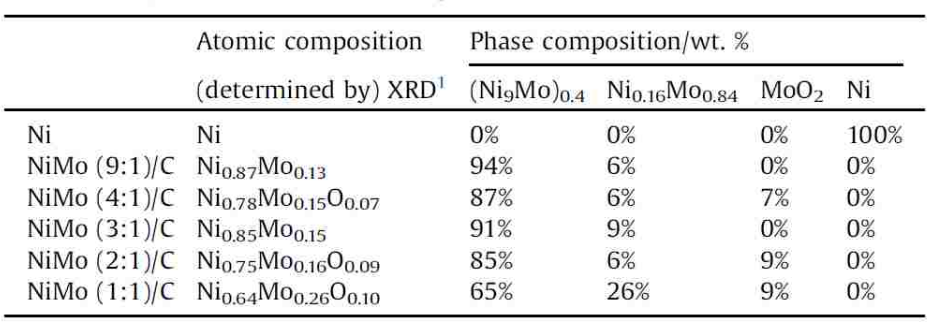

	Atomic composition (determined by) XRD[1]	Phase composition/wt. %			
		$(Ni_9Mo)_{0.4}$	$Ni_{0.16}Mo_{0.84}$	MoO_2	Ni
Ni	Ni	0%	0%	0%	100%
NiMo (9:1)/C	$Ni_{0.87}Mo_{0.13}$	94%	6%	0%	0%
NiMo (4:1)/C	$Ni_{0.78}Mo_{0.15}O_{0.07}$	87%	6%	7%	0%
NiMo (3:1)/C	$Ni_{0.85}Mo_{0.15}$	91%	9%	0%	0%
NiMo (2:1)/C	$Ni_{0.75}Mo_{0.16}O_{0.09}$	85%	6%	9%	0%
NiMo (1:1)/C	$Ni_{0.64}Mo_{0.26}O_{0.10}$	65%	26%	9%	0%

Table 3.4 Crystallite domain size calculated from XRD pattern refinement.

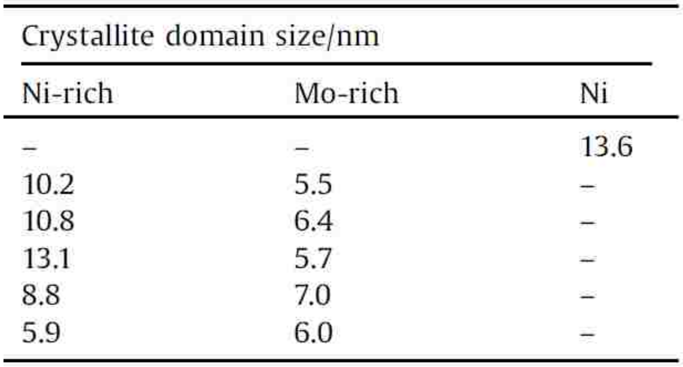

Crystallite domain size/nm		
Ni-rich	Mo-rich	Ni
–	–	13.6
10.2	5.5	–
10.8	6.4	–
13.1	5.7	–
8.8	7.0	–
5.9	6.0	–

The average crystallite size of the Ni-rich and Mo-rich solid solutions are comparable to the volume-averaged nanoparticle diameter (d_v) determined with TEM, within the standard deviation (Table 4.2). In general, the Mo-rich phase presents smaller crystallite size (5.5 to 7 nm) whereas the Ni-rich phase has larger crystallite size (8.8 to 13.1 nm), than the volume-averaged nanoparticle diameter. Only the NiMo (1:1)/C electrocatalyst makes exception to this trend: in this case, the size of the Ni-rich and the Mo-rich crystallites are similar (5.9 and 6.0 nm), and close to the volume-averaged diameter of the nanoparticles (d_v = 6.5 ±1.5 nm).

Table 3.5 Lattice parameter and expansion of the lattice parameter *vs.* $(Ni_9Mo)_{0.4}$ and $Ni_{0.16}Mo_{0.84}$ for the Ni-rich and Mo-rich phases determined by X-ray diffraction for the NiMo/C electrocatalysts synthesized in this study.

	a (Ni-rich) (nm)	Expansion of *a* *vs.* $(Ni_9Mo)_{0.4}$	a (Mo-rich) (nm)	Expansion of *a* *vs.* $Ni_{0.16}Mo_{0.84}$
NiMo (9:1)/C	0.353	0.28 %	0.419	0.48 %
NiMo (4:1)/C	0.353	0.28 %	0.420	0.72 %
NiMo (3:1)/C	0.353	0.28 %	0.421	0.96 %
NiMo (2:1)/C	0.356	1.1 %	0.423	1.44 %
NiMo (1:1)/C	0.356	1.1 %	0.423	1.44 %

Thus, based on the TEM, XRD and X-EDS results, the morphology of the NiMo/C electrocatalysts is characterized as follows:

(i) A Ni-rich phase featuring a composition close to the $(Ni_9Mo)_{0.4}$ solid solution and a diameter comprised between 8.8 and 13.1 nm (Figure 3.8 Table 3.2);

(ii) A Mo-rich phase featuring a composition close to the $Ni_{0.16}Mo_{0.84}$ solid solution and a diameter comprised between 5.5 and 7 nm (Figure 3.8 Table 3.2);

(iii) An amorphous (or crystalline, as observed in XRD for NiMo (1:1)/C, NiMo (2:1)/C and NiMo (4:1)/C) MoO_2 phase, such as observed on Figure 3.10).

XPS

X-ray photoelectron spectroscopy was used to access the composition of the surface and near-surface layers. Figure 3.11 provides clear experimental evidences of a Ni surface enrichment: the Ni surface content determined by XPS, i.e. at 0.3 nm depth, is (i) larger than that estimated from XRD analysis (for example for the NiMo (9:1)/C electrocatalyst the Ni surface content was 92 at. % (Fig. 3.11) compared to 87 at. % in average (Table 3.2)) and (ii) decreases while increasing the depth of analysis (Figure 3.11).

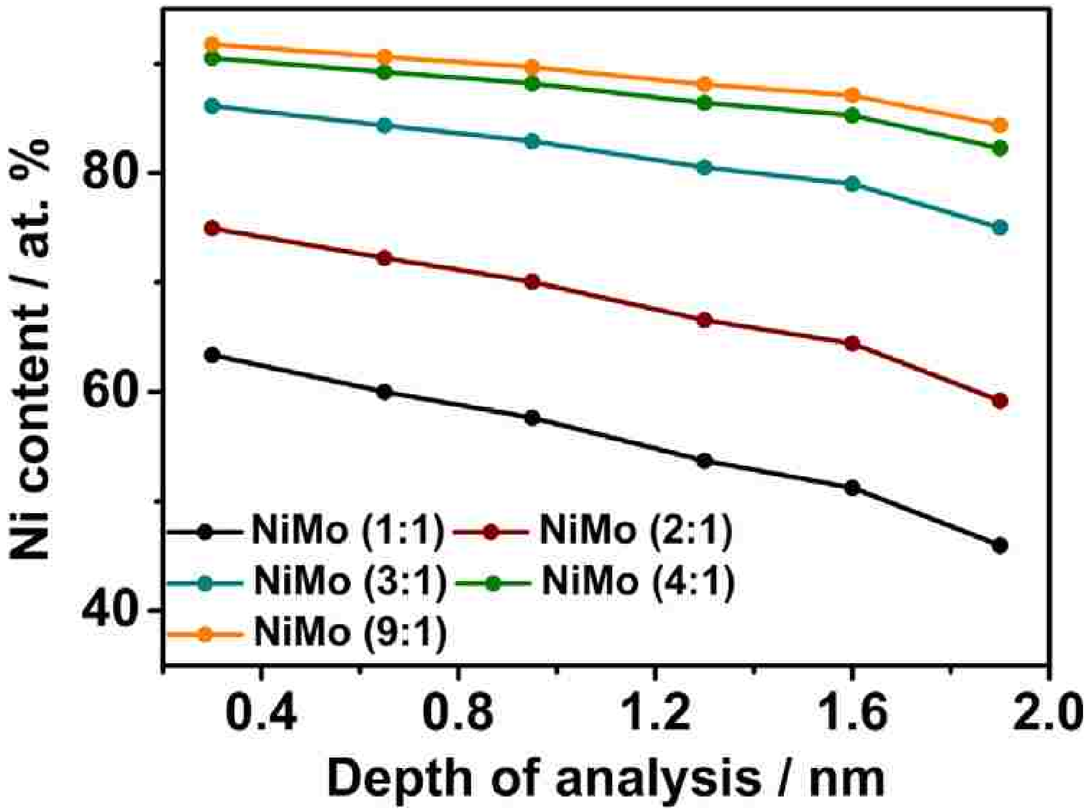

Figure 3.11: Nickel atomic content measured at different depths in the NiMo/C electrocatalysts.

The oxygen species detected by XPS (Table 4.5) were considered as (i) interstitial (e.g. in orthogonal sites for NiO) induced by the synthesis passivation step or as (ii) relevant molybdenum oxides – amorphous and crystalline (also showed by XRD, Figure 3.10 and Table 3.3). The XPS results of Figure 3.11 are representative for inter-particles heterogeneity, supporting the fact that the 'small' nanoparticles (5.5–7 nm) are Mo-rich, whereas the 'large' nanoparticles (9–14 nm) are Ni-rich. As such, Ni-rich nanoparticles are probed by XPS at the lowest depths of analysis (Fig. 3.11) whereas the highest depths of analysis (up to 1.9 nm) include not only the Ni-rich, but also the Mo-rich nanoparticles and the MoO_2 phase.

Table 3.6 Quantification of Ni and Mo elements obtained from XPS for the synthesized Ni_xMo_y/C electrocatalysts.

		Ni 2p (wt. %)			Contribution of Mo - 3d (wt. %)		
	Energy (eV)	852.8	854	855.7 – 856.7	229.1	231.3	232.7
	Species	Ni/NiMo	NiO	Ni_2O_3 / $NiMoO_4$	MoO_2	MoO_{2-3}	MoO_3 / $NiMoO_4$
Ni		17.7 %	42.1 %	40.2 %	-	-	-
NiMo (9:1)		16.3 %	30.8 %	53.0 %	41.9 %	10.4 %	47.8 %
NiMo (4:1)		16.3 %	24.5 %	59.2 %	40.8 %	9.2 %	50.1 %
NiMo (3:1)		17.2 %	26.4 %	56.5 %	50.1 %	11.6 %	38.3 %
NiMo (2:1)		17.6 %	20.5 %	61.9 %	37.6 %	9.7 %	52.6 %
NiMo (1:1)		12.1 %	11.6 %	76.3 %	38.3 %	8.2 %	53.5 %

Non-distinguishable species are separated by a slash. These results consist of integrations on the sample depth, from 0 to 2 nm for Ni and 0 to 5 nm for Mo. The highest contribution is coming from the near surface.

Electrochemical Characterization

Hydrazine Oxidation – Cyclic Voltammetry

The materials were further characterized with regards to their catalytic activity towards the electrooxidation reaction of hydrazine. Figure 3.12 shows that the mass activity of the Ni/C catalyst synthesized in this study is 14-fold larger than for the Ni/C electrocatalyst (3.74 kAg_{metal}^{-1} vs. 250 Ag_{metal}^{-1} at E = 0.2 V vs. RHE) synthesized in references [24–26].

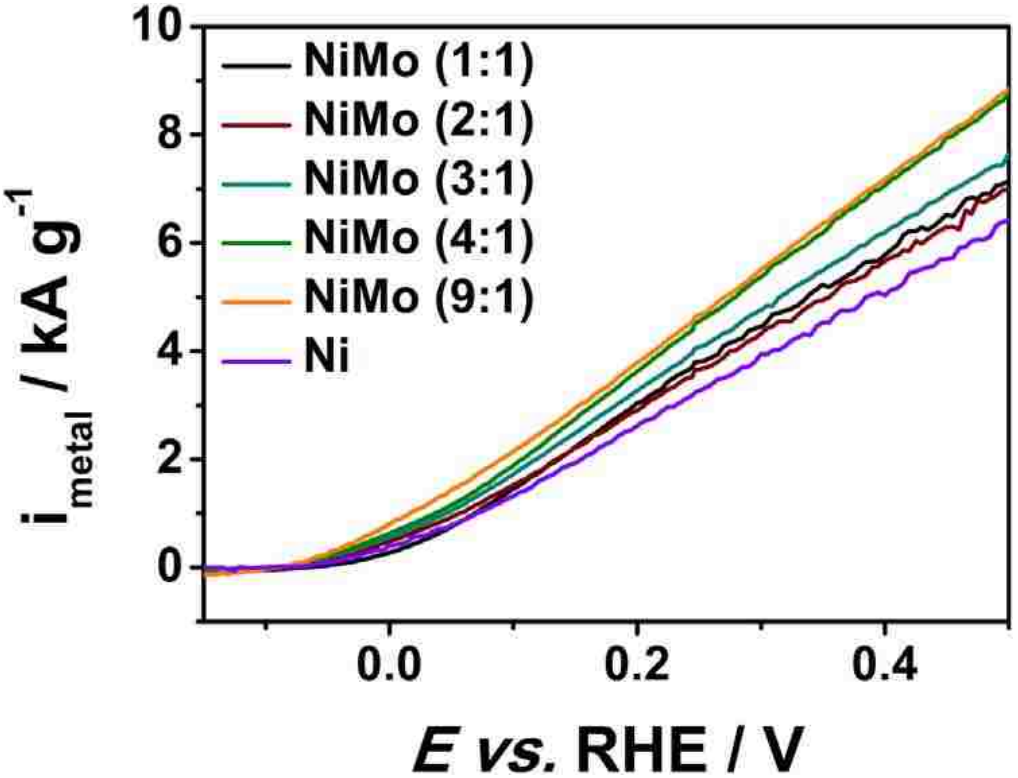

Figure 3.12: Positive-going potential scan of hydrazine hydrate oxidation measured on the NiMo/C electrocatalysts. Experimental conditions: 1 M KOH + 5 wt. % hydrazine hydrate, T = 333 K, ω = 1600 rpm, potential scan rate ν = 20 mVs^{-1}.

Obviously, these differences cannot be accounted for by the different hydrazine concentrations employed in these studies (1 M in Sakamoto et al. works [25,27] vs. 1.56 M here). Instead, one may assume that a high nickel oxide content inhibited the catalytic activity of the Ni/C catalysts in references. [25,27]. The oxide level is very low in the present study: the oxides observed by XPS (Table 3.5) are induced by the passivation step and removed during the catalyst electrochemical activation. This demonstrates the clear advantage of the present wet impregnation synthesis process, which avoids the formation of a thick oxide layer thanks to the use of urea as an oxide ‘scavenger’.

Table 3.7 Mass activity of the NiMo/C electrocatalysts for the electrooxidation of hydrazine hydrate. Experimental conditions: 1 M KOH + 5 wt. % Hydrazine hydrate, T = 333 K, ω = 1600 rpm, potential scan rate ν = 20 mVs^{-1}.

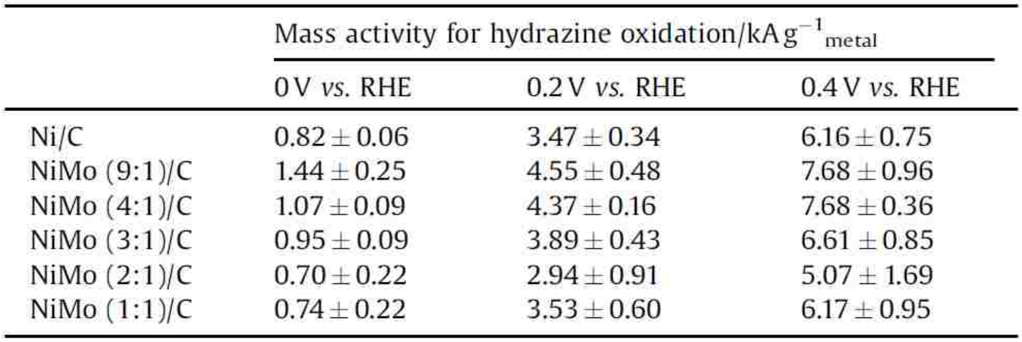

	Mass activity for hydrazine oxidation/kA g^{-1}$_{metal}$		
	0 V *vs.* RHE	0.2 V *vs.* RHE	0.4 V *vs.* RHE
Ni/C	0.82 ± 0.06	3.47 ± 0.34	6.16 ± 0.75
NiMo (9:1)/C	1.44 ± 0.25	4.55 ± 0.48	7.68 ± 0.96
NiMo (4:1)/C	1.07 ± 0.09	4.37 ± 0.16	7.68 ± 0.36
NiMo (3:1)/C	0.95 ± 0.09	3.89 ± 0.43	6.61 ± 0.85
NiMo (2:1)/C	0.70 ± 0.22	2.94 ± 0.91	5.07 ± 1.69
NiMo (1:1)/C	0.74 ± 0.22	3.53 ± 0.60	6.17 ± 0.95

All the NiMo/C catalysts with a low molybdenum content (i.e. <15 at. %, Table 3.2) feature higher mass activity than Ni/C, regardless of the potential region considered (E = 0 V vs. RHE, 0.2 V vs. RHE or 0.4 V vs. RHE, Table 3.7). Those activities are also higher than reported in the literature (1.7 kAg$_{metal}^{-1}$ for $Ni_{0.5}Mn_{0.5}$/C vs. 1.2 kAg$_{metal}^{-1}$ for $Ni_{0.7}$Fe0.3/C, 1.4 Ag$_{metal}^{-1}$ for $Ni_{0.4}Zn_{0.6}$/C and 0.7 kAg$_{metal}^{-1}$ for $Ni_{0.9}La_{0.1}$/C at E = 0.2 V vs. RHE) [25–27]. The activity values presented by Martinez et al. [26, 5] (4 kAg$_{metal}^{-1}$ for an unsupported $Ni0_{.87}Zn_{0.13}$ catalyst at E = 0.4 V vs. RHE) are approaching the present ones. However, a dramatic decrease of the catalysts activity for the electrooxidation of hydrazine is noticed with increasing the Mo content (Table 3.7). Interestingly, and despite a higher molybdenum content than NiMo (2:1)/C, the NiMo (1:1)/C electrocatalyst features similar performances to the Ni/C catalyst at E = 0.2 and 0.4 V vs. RHE. Besides, the residual quantity of crystalline molybdenum oxides does not have any significant effect on the mass activity for hydrazine electrooxidation, since no correlation was observed between the current measured at E = 0 V vs. RHE, E = 0.2 V vs. RHE and E = 0.4 V vs. RHE (Table 3.7) and the oxide content (Table 3.3).

Therefore, the mass activity enhancement observed for the NiMo/C catalysts with low molybdenum content (i.e. <15 at. %) could be induced by (i) the reduction of the nanoparticles size compared to Ni/C (see. Figure 3.8 and Table 3.3), i.e. an increase of the active surface area of the electrocatalyst or/and (ii) a positive effect of the molybdenum as discussed below. It is worth noting that low molybdenum content (<13 at. %, e.g. NiMo (9:1)/C) leads to a lowering of the overpotential for HH oxidation (see. Figure 3.12) compared the overpotential of Ni/C. However, the slightest increase in the molybdenum content (e.g. from 13 at. % to 15 at. %) appears to increase the overpotential, suggesting that there is an optimum for the Mo content. This assumption is further supported if one considers the electrocatalysts specific activity (i.e. normalized by the specific surface area determined from the TEM micrographs, Table 3.8). A dramatic decrease (i.e. from 27 ± 5 $\mathrm{Am}_{\mathrm{metal}}^{-2}$ for NiMo (9:1) to 7 ±2 $\mathrm{Am}_{\mathrm{metal}}^{-2}$ for NiMo (1:1) at 0 V vs. RHE) is observed for molybdenum contents ≥15 at. %. It is worth noting, however, that the residual amorphous and crystalline oxide content observed in NiMo (2:1) and NiMo (1:1) (see. Figure 3.8) may account for an overestimated specific surface area (Table 3.8).

Catalyst Specific Surface Area

The catalysts specific surface area was determined using the TEM micrographs, by determining the surface-average diameter (d_S), n_i being the number of particles of diameter d_i:

$$d_s = \frac{\sum_1^N n_i d_i^3}{\sum_1^N n_i d_i^2} \qquad (5)$$

The specific surface area and the surface-averaged diameter are linked by the following equation (S being the specific surface area in $m^2g^{-1}_{metal}$; ρ_{alloy} the volumetric mass of the metal, with respect to its composition and d_s being the surface-averaged diameter):

$$S = \frac{6}{\rho_{alloy} \times d_s} \tag{6}$$

For comparison purposes, the current at 0 V *vs.* RHE was normalized by the specific surface area (see Table 3.8).

Table 3.8 : Determination of the specific surface area ‘S’, and the specific activity (SA) at 0 V *vs.* RHE from the catalyst composition determined by XRD and the surface-averaged diameter ‘d_s’ of the nanoparticles.

	Atomic composition	d_s, nm	ρ_{alloy} (gm^{-3})	S ($m^2 g_{metal}^{-1}$)	SA (Am_{metal}^{-2}) 0 V *vs.* RHE
Ni	Ni	13.7 ± 4.3	8.9 × 10^6	49.2	17 ± 1
NiMo (9:1)	$Ni_{0.87}Mo_{0.13}$	12.3 ± 3.5	9.1 × 10^6	53.6	27 ± 5
NiMo (4:1)	$Ni_{0.78}Mo_{0.15}O_{0.07}$	11.4 ± 4.3	9.1 × 10^6	57.8	19 ± 2
NiMo (3:1)	$Ni_{0.85}Mo_{0.15}$	10.4 ± 3.1	9.1 × 10^6	63.4	15 ± 1
NiMo (2:1)	$Ni_{0.75}Mo_{0.16}O_{0.09}$	7.4 ± 2.5	9.1 × 10^6	89.1	8 ± 2
NiMo (1:1)	$Ni_{0.64}Mo_{0.26}O_{0.10}$	6.0 ± 1.8	9.3 × 10^6	109.9	7 ± 2

Adsorbed Species and NH_3 Generation

The reaction mechanism and intermediate species for hydrazine oxidation has been studied previously using Infrared Reflectance Adsorption Spectroscopy [5]. Here, *in situ* studies were performed to directly observe the formation, and consumption, of intermediate species as a function half-cell voltage potential for HH oxidation on aerosol derived NiZn (see Chapter 2 for a detailed description of experimental methods). The resulting mechanism elucidated from this study is as follows: First, HH is adsorbed on the NiZn surface. Following adsorption, band troughs appear at -0.39 V: 3225 cm^{-1}, 1646 cm^{-1}, and 801 cm^{-1}. These bands belong to NH and $(OH)^-$ species and are shown to decrease with increasing cell voltage, indicated the consumption of these species. Simultaneously, the appearance of band peaks at 2775 cm^{-1}, 1900 cm^{-1}, and 1080 cm^{-1}, are observed indicating the generation of these species. Referencing these bands to literature, [84-87], these bands associated with the formation of NH_2^+, Ni-H stretch, and N-N stretch respectively (summarized in Table 3.9).

Table 3.9 IRRAS band assignments of intermediate species for hydrazine hydrate oxidation. Band assignments were referenced from literature, [a] [87] and [b] [84-86].

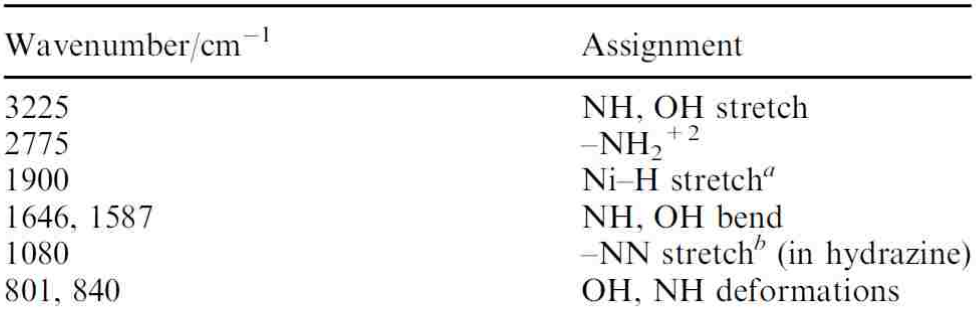

Wavenumber/cm^{-1}	Assignment
3225	NH, OH stretch
2775	$-NH_2^{+2}$
1900	Ni–H stretch[a]
1646, 1587	NH, OH bend
1080	–NN stretch[b] (in hydrazine)
801, 840	OH, NH deformations

These results indicate, that for NiZn, HH oxidation proceeds via a two-step reaction mechanism following the initial adsorption of HH. First, HH adsorbs to the Ni active site releasing water and forming N_2H_{2ads} species. Next, N_2H_{2ads} is dehydrogenated forming H_{ads} on neighboring active sites resulting in N_2H_{2ads}. These intermediate reactions are shown in equations 5-7.

$$N_2H_4 * H_2O \rightarrow N_2H_{4,ads} + H_2O \tag{7}$$

$$N_2H_{4,ads} \rightarrow 2H_{ads} + N_2H_2^{+2}{}_{ads} \tag{8}$$

$$2H_{ads} + N_2H_2^{+2}{}_{ads} + 4OH^- \rightarrow N_2 + 4H_2O + 4e^- \tag{9}$$

NiZn/Ketjenblack - Hydrazine Hydrate Oxidation Mechanism

IRRAS

As the mechanism of HH oxidation on unsupported NiZn was previously hypothesized from *in situ* infrared adsorption spectroscopy (IRRAS) experiments [59]. These same experiments were performed with supported NiZn/KB and confirmed that the observed mechanism is not visibly altered by the inclusion of carbon and a different synthesis method. Figure 3.13 shows the appearance and disappearance of species critical to the reaction mechanism. Notable is a decreased signal from N-H/O-H (3225 cm^{-1}) indicating species consumption and increased signals from $-NH2^{2+}$ (2775 cm^{-1}), Ni-H (1900 cm^{-1}), and HNH/HOH (1646 cm^{-1}) indicating the presence of intermediate oxidation species. The presence of N-N (1080 cm^{-1}), which is characteristic of HH, is also noted. These same trends (increasing/decreasing signals) were observed for unsupported catalysts, suggesting that the reaction pathway, equations 5-7, is the same for supported catalysts synthesized by mechanochemical methods.

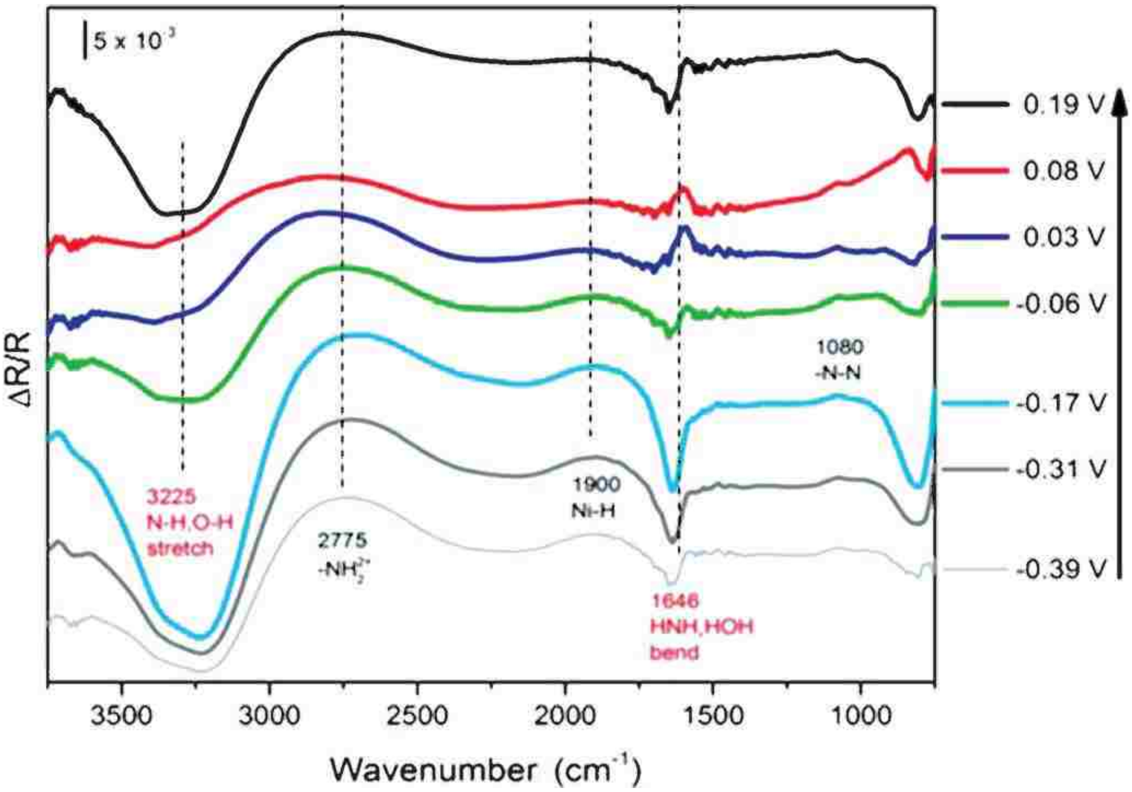

Figure 3.13: In situ IRRAS with simultaneous linear voltammetry. 60 wt.% NiZn, 1M KOH + 5 wt.% HH, room temperature, no rotation, 76.5 mg-cm^{-2} catalyst, 1 mVs^{-1}, V vs. reversible hydrogen electrode (RHE).

As was reported by Martinez et al. [59], the principle finding is related to the formation of Ni-H stretch at 1900 cm^{-1} eluting to the formation of H_{ads} species as described by equation 8. This result indicates the formation of Lewis base sites on Ni when alloyed with Zn, a result not observed for other Ni alloys, namely NiCo, studied for hydrazine oxidation reaction. This is a significant finding in that it suggests that Lewis base sites formed on NiZn alloy act as electron pair donor sites, which ultimately promote the adsorption and dehydrogenation of HH which can explain the improved catalytic activity of HH oxidation on NiZn over NiCo [59]. As HH oxidation on supported NiZn has been determined to follow the same mechanism as the unsupported NiZn, the improved activity observed for supported NiZn (Figure 3.5) is directly related to particle size and pore size effects, leading to improvements in the diffusion limiting current.

NiMo NH_3 Generation

In Situ FTIR

In situ FTIR analyses (Figure 3.14) were performed to investigate the mechanism of hydrazine electrooxidation on the NiMo surface. The NiMo (1:1)/C catalyst presents a band ascribed to ammonia deformation at 960 cm^{-1}. Its contribution decreases with an increase in potential, therefore demonstrating lower ammonia production at high potential (Figure 3.14). Even though ammonia is produced in higher proportions on Ni/C than on NiMo (1:1)/C (see. Table 3.10), no band was observed at 960 cm^{-1}, suggesting that the adsorption conformation of ammonia differ on the Ni/C electrocatalyst surface. It is worth nothing that the increase in potential results in a faster consumption of the N_2H_4 on the surface, and thus a reduction of the band intensity observed at 1080 cm^{-1} (2) for Ni/C and NiMo (1:1)/C.

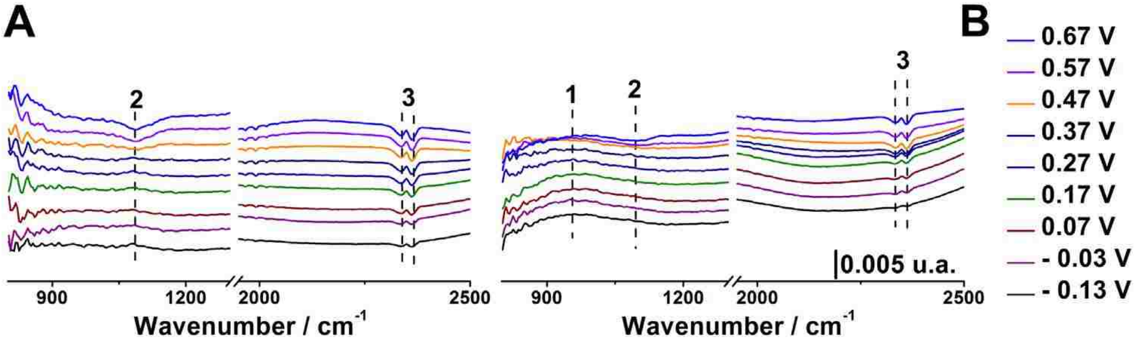

Figure 3.14: In situ FTIR spectra measured during hydrazine hydrate electrooxidation on (A) Ni/C and (B) NiMo (1:1)/C electrocatalysts. All electrode potentials are referred to the RHE scale. Experimental conditions: 1 M KOH + 0.5 wt. % N_2H_4 Potential sweep rate ν = 1 mV s^{-1}. The numbers are relevant for the species described in Table 3.9. The bands labeled 1, 2, and 3 are ascribed to ammonia deformation, N-N stretch, and atmospheric CO_2 respectively.

Table 3.10 Detection of ammonia generation by ion chromatography during the hydrazine hydrate oxidation experiments on the NiMo/C electrocatalysts.

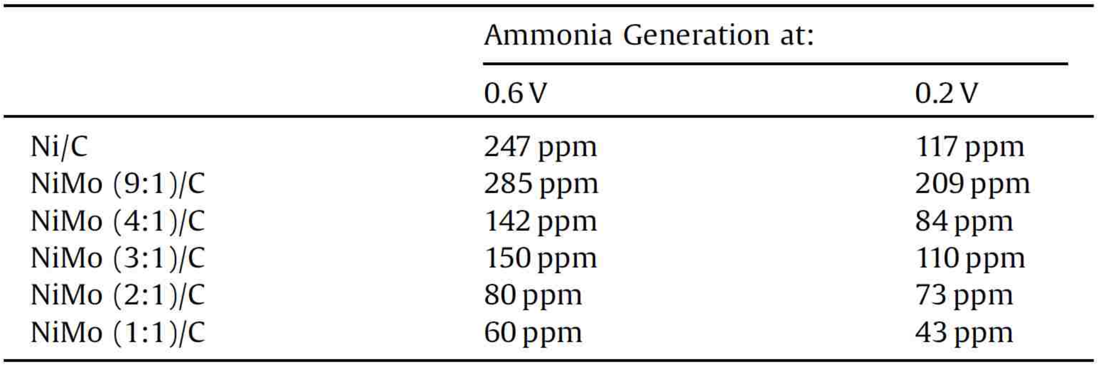

	Ammonia Generation at:	
	0.6 V	0.2 V
Ni/C	247 ppm	117 ppm
NiMo (9:1)/C	285 ppm	209 ppm
NiMo (4:1)/C	142 ppm	84 ppm
NiMo (3:1)/C	150 ppm	110 ppm
NiMo (2:1)/C	80 ppm	73 ppm
NiMo (1:1)/C	60 ppm	43 ppm

DFT

Density functional theory (DFT) calculations were performed to provide further insights into the effect of molybdenum on the hydrazine adsorption conformation and ammonia production. Since (Ni9Mo)0.4 and Ni0.16Mo0.84 are presenting known properties close from the Ni-rich and Mo-rich phases, they were discussed in the following part. The adsorption energies of hydrazine on the Ni (111), $(Ni_9Mo)_{0.4}$ (111) and $Ni_{0.16}Mo_{0.84}$(111) surfaces are given in Table 3.11 and the corresponding optimized geometries are shown in Figure 3.15. It is shown that the adsorption energies of hydrazine increase with the surface molybdenum content (Table 3.11). The adsorption energy of hydrazine is _0.81 eV on the Ni (111) surface, -0.92 eV on the $(Ni_9Mo)_{0.4}$ (111) surface and -1.48 eV on the $Ni_{0.16}Mo_{0.84}$ (111) surface. Thus, hydrazine is 0.67 eV more stable on the $Ni_{0.16}Mo_{0.84}$ (111) surface than on the Ni (111) surface (Table 3.10). In addition, hydrazine adsorbs on the $Ni_{0.16}Mo_{0.84}$ (111) surface in a bridge position between two Mo atoms, with N-Mo distances of 2.33 Å and 2.29 Å, while on both the Ni (111) and $(Ni_9Mo)_{0.4}$ (111) surfaces, hydrazine adsorbs in a top position with one nitrogen adsorbed on the surface and the other one oriented towards the solution (Fig. 3.15). Therefore, the DFT calculations suggest that the Mo content in the surface/subsurface layers must significantly impact the catalysts performances, as detailed below.

Table 3.11 Adsorption energies (ΔE_{ad}) of hydrazine (N_2H_4) and ammonia (NH_3) on the Ni (111), $(Ni_9Mo)_{0.4}$ (111) and $Ni_{0.16}Mo_{0.84}$ (111) surfaces.

System	$\Delta E_{ad}(N_2H_4)$/eV	$\Delta E_{ad}(NH_3)$/eV
Ni(111)	−0.81	−0.78
$(Ni_9Mo)_{0.4}$(111)	−0.92	−0.85
$Ni_{0.16}Mo_{0.84}$(111)	−1.48	−0.89

The Ni-rich phase is mainly responsible for the enhanced catalytic properties, since an increased Ni-rich content leads to increased catalytic performances (Table 3.7 and Fig. 3.12). However, DFT calculations have shown that Mo-containing Ni-rich surfaces and, to a larger extent, Mo-rich surfaces stabilize the N-N bond and avoid ammonia production (i.e. fuel losses). However, this stronger N_2H_4 binding and different adsorption position is detrimental to the catalyst activity (Table 3.11). This may be rationalized by considering the Sabatier principle, which states that the adsorption of the reactive species should be neither too strong nor too weak.

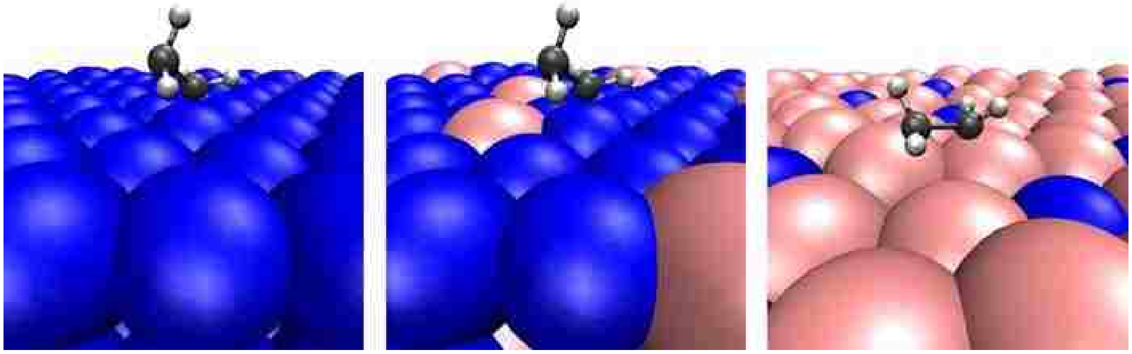

Figure 3.15: Geometries of hydrazine molecule in gauche conformation adsorbed on the Ni (111), $(Ni_9Mo)_{0.4}$ (111) and $Ni_{0.16}Mo_{0.84}$ (111) surfaces as calculated using DFT with PBE functional.

Fuel Cell

Ammonia generation measurements performed in direct hydrazine fuel cell (see Chapter 2 for the detailed process) support the fact that molybdenum stabilizes the N-N bond (Table 3.11), since the lowest ammonia production is observed for the catalysts with highest molybdenum content, NiMo (1:1)/C. It can also be emphasized that ammonia production is reduced at high cell voltage, both on Ni/C and NiMo/C, possibly due to a modification of the hydrazine electrooxidation mechanism. Such hypothesis is supported by the change in the NH_3 absorption observed for NiMo (1:1)/C with the potential variation (Figure 3.14).

Conclusion

Previous work elucidating the high catalytic activity of NiZn catalysts, as well as the reaction mechanism, for HH oxidation was further developed to increase the Ni mass activity by supporting highly dispersed NiZn nanoparticles on Ketjenblack carbon. The effect of the support in reducing mass transfer resistance resulted in peak current density in half cell measurements of 16000 Ag^{-1}_{metals} and peak power density in alkaline MEA of 450 $mWcm^{-2}$. At the time of publication, these results were the highest reported activity for a PGM-free HH oxidation catalyst in alkaline media.

Carbon-supported NiMo catalysts were synthesized using the wet impregnation process, with the addition of urea to avoid the formation of MoO_2. The NiMo/C catalysts were composed of 3 distinct phases (i) Ni-rich/C nanoparticles, (ii) Mo-rich/C nano-particles and, for NiMo (4:1), NiMo (2:1) and NiMo (1:1) (iii) amorphous and/or crystalline MoO2/C. The NiMo/C catalysts with a low molybdenum content (<15 at. %) present better catalytic performance for the hydrazine electrooxidation than Ni/C due to a positive effect of the molybdenum. Increasing the molybdenum content led to depreciated catalytic performance, thereby demonstrating the existence of an optimum molybdenum content for hydrazine electrooxidation. In situ FTIR measurements and DFT calculations suggest that the presence of molybdenum stabilizes the adsorbed hydrazine, thereby avoiding its decomposition into ammonia. The NiMo (1:1)/C catalyst presents similar mass activity for hydrazine electrooxidation than the Ni/C catalyst at E = 0.2 and 0.4 V vs. RHE but its ammonia generation is 4 times lower at a fuel cell voltage of 0.6 V.

Chapter 4

Introduction-Hydrogen Oxidation

Fuel Cell Vehicles (FCV) entered our everyday life in 2015 with the official announcement by Toyota Motor Corp. on selling the first commercial Mirai FCV [88]. Currently, all major car manufacturers are planning to release FCVs in the near future. It should be noted that behind this commercial breakthrough there are decades of research in the field of proton exchange membrane fuel cells (PEMFCs). To create a high-performance fuel cell system, a substantial effort has been made in the development of polymer membranes and ionomers, catalysts, membrane electrode assemblies (MEA), stack components, and balance of plant (BOP) units to complete the successful fuel cell system.

Recently, a parallel pathway of the fuel cell development has opened, the one based on using anion exchange membranes (AEMs) instead of PEMs. This new avenue has attracted the attention of a number of research groups [89-102]. This technology will allow to substantially decrease the device cost by replacing expensive platinum catalysts on both sides of MEAs by platinum group metal-free (PGM-free) catalysts. The cathodic reaction of the oxygen reduction is believed to follow different mechanism in acid and alkaline electrolytes. [88-91] While platinum-based catalysts dominate in performance in PEMFC, a substantial number of PGM-free catalysts demonstrate higher oxygen reduction activity in alkaline electrolytes. Over the last decade, a list of promising platinum-free [103-106] and platinum group metal-free (PGM-free) catalysts [107-114] have been developed for the AEMFC cathodes. In contrast, anodic hydrogen oxidation reaction (HOR) is much slower in alkaline media as compared to HOR in acidic electrolyte [115]. To date, the development of Pt-free palladium or nickel-based catalysts still presents a challenge [116].

Introducing PGM-free anode catalysts would complete the materials' set for the AEMFC and would reveal its full economic potential as the first materials unlimited low-temperature FC technology entirely based on Earth-abundant element base.

The following sections detail the development of one such PGM-free catalysts for HOR, where similar to catalysts previously discussed, the catalytic activity of carbon supported Ni was tuned through alloying small amounts of oxyphilic metals, Mo and Cu, to enhance the oxidizing capability of the Ni catalyst.

Mechanism of Hydrogen Oxidation

The kinetic mechanism for HOR on Ni can be modeled using the Tafel-Heyrovsky-Volmer kinetic mechanism for the hydrogen electrode reactions and a two-steps mechanism for Nickel oxidation and reduction. The hydrogen oxidation reaction in alkaline medium involves the Tafel (eq. 10) or the Heyrovsky (eq.11) step on free Ni sites:

$$H_2 + 2Ni \rightleftharpoons 2\ Ni\text{-}H_{ad} \qquad (10)$$

$$H_2 + OH^- + Ni \rightleftharpoons Ni\text{-}H_{ad} + H_2O + e^- \qquad (11)$$

The formation and oxidation of the adsorbed hydrogen intermediate H_{ad} can also occur according to the Volmer reaction in alkaline medium:

$$Ni\text{-}H_{ad} + OH^- \rightleftharpoons H_2O + e^- + Ni \qquad (12)$$

The formation of $Ni\text{-}(OH)_2$ is modelled using a simplified two steps process:

$$OH^- + Ni \rightleftharpoons Ni\text{-}OH_{ad} + e^- \qquad (13)$$

$$OH_{ad} + OH^- \rightleftharpoons Ni\text{-}(OH)_{2,ad} + e^- \qquad (14)$$

Methods

Materials Synthesis

NiMo/Ketjenblack

PGM-free 50wt% NiMo/Ketjenblack catalyst was synthesized by thermal reduction of nickel and molybdenum precursors on the surface of Ketjenblack (KB). A mixture of nickel nitrate and ammonium molybdate was dissolved in a small volume of water and impregnated on the carbon support (Ketjenblack surface area ~ 1200 m^2g^{-1}). Considering previous studies on the influence of Mo on the electrocatalytic activity of Ni in the hydrogen *evolution* reaction (HER), [92-94] the atomic ratio between Ni and Mo was selected as 90:10, a composition which insures the resulting alloy is within the solid solution region. The mixture was placed in an oven at T=85°C and water was allowed to evaporate. The dry composite mixture was ground with mortar and pestle. The fine powder was reduced in a 7 at. % hydrogen atmosphere (flow rate of 100 sccm) at T=550 °C for 60 minutes. Considering that finely divided Ni is pyrophoric, before exposing the catalyst to the ambient, it was passivated in a He flow containing 2% of O_2 at room temperature for 8 hours. This powder was used for physical-chemical and electrochemical tests. Pd/XC72R (30wt% of Pd) electrocatalysts was synthesized by Soft Alcohol Reduction Method (SARM) published previously [91]. The weighted amount of Vulcan XC72R was dispersed in water by magnetic stirrer followed by addition of calculated amount of $Pd(NO_3)_2*xH_2O$ in order to obtain 30wt% of palladium on XC72R. The ethanol solution (100% pure) in 3x volumetric excess was introduced into the slurry of XC72R and palladium nitrate under vigorous stirring. After stirring for 1 hour, the slurry was centrifuged and washed with DI water. Obtained 20 wt.% Pd/XC72R was dried in air at T=85 ◦C for 6 hours and used as a cathode in MEA manufacturing.

Materials Characterization

XRD

The X-ray diffraction pattern for NiMo/KB shown in Figure 4.1 suggests that NiMo/KB comprises three phases: Ni metal (FCC), $NiMo_4$ (FCC), and MoO_2 (monoclinic). The Ni metal phase accounts for ca. 80wt.% of the metal-containing phases. Its lattice parameter, calculated from the pattern refinement, is 3.529 nm. Comparing this result with the lattice parameter of pure Ni (FCC), 3.524 nm, it can be concluded that this phase has little to no substitution of Mo into the lattice. However, a small amount of $NiMo_4$ was found which accounts for approximately 2 wt.% of the total metal-containing phases. MoO_2 accounts for approximately 18 wt.% of the metal-containing phases. The XRD pattern shows no evidence of crystalline Ni oxide/hydroxide phases. The average crystallite domain size of Ni, found by fitting the peak broadening, is 19 nm. Poor angular resolution of the peaks corresponding to $NiMoO_4$ and MoO_2 phases indicates that they are not highly crystalline and the presence of amorphous mixed oxides ($NiMoO_x$) in amounts below the detection limit cannot be excluded.

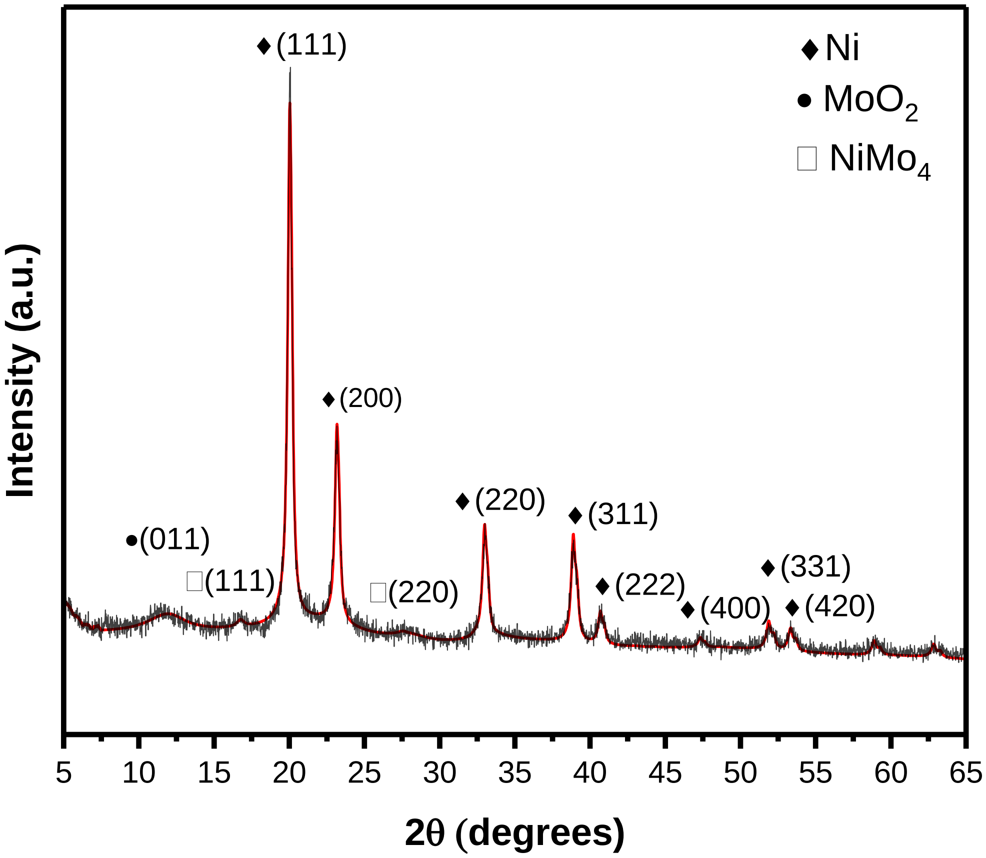

Figure 4.1: X-ray diffraction pattern for NiMo/KB. Reflections of the indexed phases used in the pattern refinement are shown. The calculated pattern refinement is shown in red.

As discussed in the previous chapter, the addition of urea as a reducing agent for molybdenum species was demonstrated to aid in (i) the reduction of molybdenum oxides and (ii) the production of solid solutions of Ni and Mo. A considerable draw-back from this method is related to catalyst yields due to the evolution of gasses during the pyrolysis of urea. As such, considerable spill-over occurs in the reaction vessel eliminating a majority of the catalyst. Therefore, it is not a feasible synthetic method for yielding the quantity of homogenous catalyst needed for the MEA testing presented herein. For these reasons, urea was not added to the synthesis of NiMo/KB, which explains the presence of Mo and NiMo oxides.

XPS

XPS analysis was carried out on the NiMo/KB catalysts to investigate the surface composition of the metal and metal oxide phases, the results are presented below. Table 4.1 shows the surface elemental and chemical composition of NiMo/KB catalyst derived from the analysis of XPS data. The fitted XPS profiles are shown in Figure 4.2.

Table 4.1 The elemental composition obtained by XPS. Distribution of different types of Ni and Mo present in relative percentage.

	C 1s	O 1	Mo 3d	Ni 2p	*Ni/Mo*
Total, at %	91.1	7.0	0.92	0.97	*1.05*
	Ni metal	**NiO**	**$Ni(OH)_2$**	**$NiMoO_x$**	
Ni, rel %	19.0	30.2	39.4	11.4	
	Mo metal	**MoO_2**	**MoO_2/ $Mo(OH)_2$**	**Mo (V) %**	**$NiMoO_x$/ MoO_3 %**
Mo, rel %	2.7	13.6	18.1	7.2	58.4

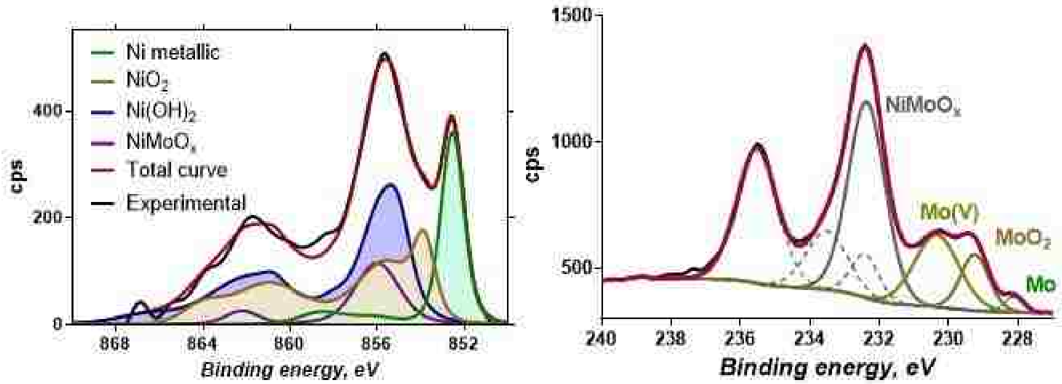

Figure 4.2: Fitted XPS spectra for (left) Ni 2p and (right) Mo 3d spectra.

The atomic percent ratio of Ni to Mo is close to 1 indicating high surface enrichment in molybdenum. Ni is present mainly in oxidized form with some metallic component and a small amount of nickel molybdenum oxide $NiMoO_x$. Mo is present mainly as mixed oxide with small amounts of Mo(IV), and Mo(V) detected. With Mo being segregated to the surface and its chemical state identified as mainly $NiMoO_x$, we can conclude that while in the bulk particles are mostly comprised of metallic Ni, their surface is rich in oxidized Mo and Ni species.

Electrochemical Characterization

Cyclic Voltammetry

To access the intrinsic HOR activity of NiMo/KB and compare it with that of the state-of-the-art Pt-free HOR catalysts, CVs were measured in N_2- and H_2-saturated 0.1 M NaOH electrolyte at various sweep rates, catalyst loadings, and electrode rotation rates, Figure 4.4. The electrocatalytic activity of the NiMo/KB catalyst towards HOR is evidenced by the higher currents detected in the interval from 0 to 0.3 V vs. RHE in H_2 compared to the N_2 atmosphere (Figure 4.3).

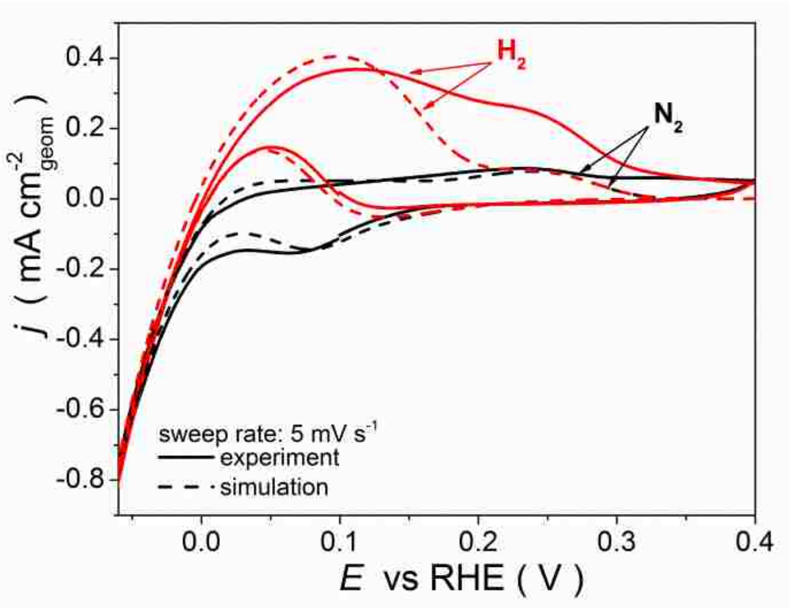

Figure 4.3: Comparison of the experimental (solid line) and simulated (dashed line) cyclic voltammograms for NiMo/KB (with a loading of 100 µg cm^{-2}) in N_2- (black) or H_2-saturated (red) 0.1 M NaOH at a sweep rate of 5 mV s^{-1}. All the curves are presented after the subtraction of the KB carbon contribution.

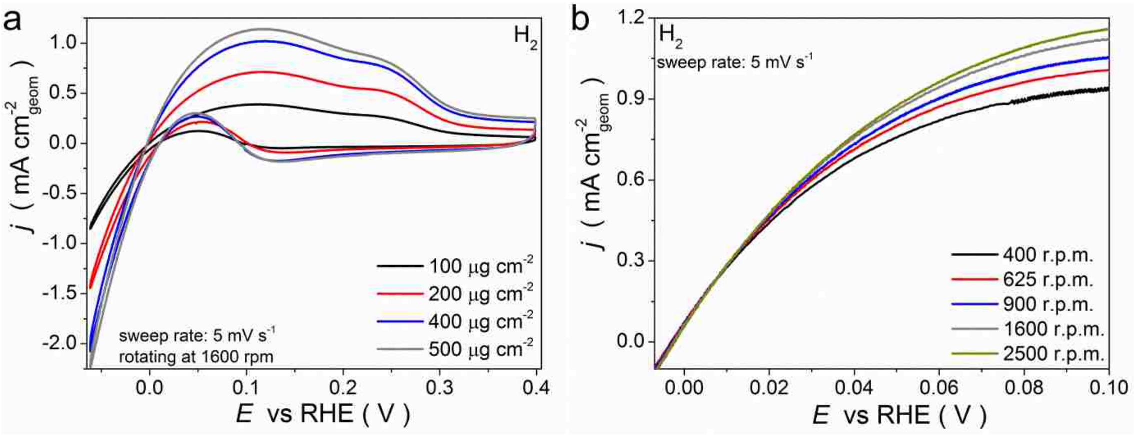

Figure 4.4: (a) Cyclic voltammograms obtained for NiMo/KB with various loadings in H_2-saturated 0.1 M NaOH at a sweep rate of 5 mVs^{-1} and rotating speed of 1600 RPM; (b) Linear sweep voltammograms obtained for NiMo/KB (with a loading of 500 µg cm^{-2}) in H_2-saturated 0.1 M NaOH at a sweep rate of 5 mVs^{-1} and various rotating speeds.

One may see that the HOR currents decay at potentials above ~0.12 V without reaching the diffusion limiting value observed for Pt electrodes [125], due to blocking of the Ni surface by α-$Ni(OH)_2$ [123]. Note however that this surface blocking is reversible, and the potential reversal allows to restore the HOR activity (positive and negative potential scans in Figure 4.4). The increase of the catalyst loading on the surface of the GC electrode results in an expected increase of the anodic currents (Figure 4.4a), and in their rotating speed dependence (Figure 4.4b), the latter confirming the high activity of the NiMo/KB in the HOR. However, as can be seen from Figure 4.4a currents do not increase proportionately to the catalyst loading, which may be attributed to mass transport losses in the thick catalyst layer. Therefore, the intrinsic activity of NiMo/KB was determined from the micro polarization region from -10 to 10 mV (see Figure 4.5) at the catalyst loading of 100 µg cm^{-2}. Exchange current densities in the HOR normalized either to the ECSA or to the metal mass are presented in Table 4.2 along with the best Pt-free catalysts published up to now. [115, 126, 127, 128]. One may notice that the mass-weighted activity of the NiMo/KB catalyst demonstrates the value, which is higher than any of the PGM-free catalysts reported until now and is comparable to the mass activity of Pd/C catalyst with the similar particle size. The surface-weighted activity of NiMo/KB is twice as high as the activity of electrodeposited CoNiMo alloy [127], comparable to the activity of Ni on N-CNT (the highest reported for PGM-free HOR catalysts) [126], but is somewhat lower than the one reported for commercial carbon-supported Pd nanoparticles [128]. From Table 4.2 it can also be seen that the activity of NiMo/KB shows a 12-fold enhancement compared to polycrystalline Ni [123].

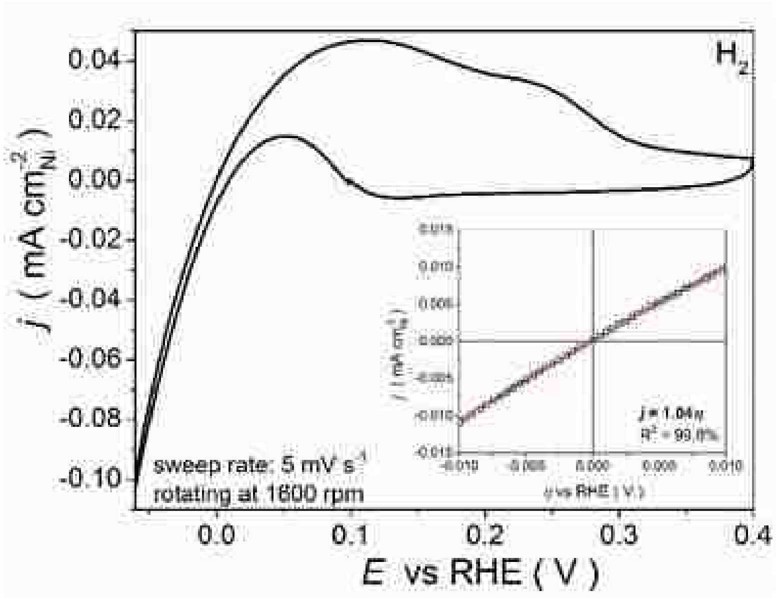

Figure 4.5: Cyclic voltammogram obtained for NiMo/KB (with a loading of 100 µg cm^{-2}) in H_2-saturated 0.1 M NaOH at a sweep rate of 5 mV s^{-1} and rotating speed of 1600 r.p.m. Inset demonstrates how the exchange current density is calculated from the micropolarization region, according to the equation $j = \frac{j_0 nF}{RT}\eta$.

Table 4.2 Specific activities of Pt-free catalysts towards HOR in alkaline media.

Sample	T / °C	m_{M+C} / µg cm^{-2}	A_{ECSA} / cm^2_M	j_0 / µA cm$^{-2}_{ECSA}$	i_o / A g_M^{-1}	Reference
NiMo/KB	25	100	1.6 ± 0.2	27 ± 2	4.5 ± 0.2	This work
Ni/N-CNT	r.t.	350	6.2	28	3.5	[126]
Ni/CNT	r.t.	350	5.2	9.2	1.0	[126]
CoNiMo	r.t.	-	-	15	-	[127]
Ni_{pc}	25	-	0.5	2.2	-	[123]
20% Pd/C Premetek Co	20	100	3.0 ± 0.2	52 ± 2	38 ± 4	[127]
20% Pd/C (d_n^{TEM}= 34±13 nm)	20	100	0.28 ± 0.8	118 ± 5	5 ± 1	[127]
Pd/C	40	50	1.0 ± 0.2	60 ± 20		[115]

MEA

The Catalyst Coated Membrane (CCM) method is a preferred method of fabrication of alkaline exchange MEAs, as a lamination of alkaline MEA components by hot pressing is not possible. The fuel cell test results are shown in Figure 4.6.

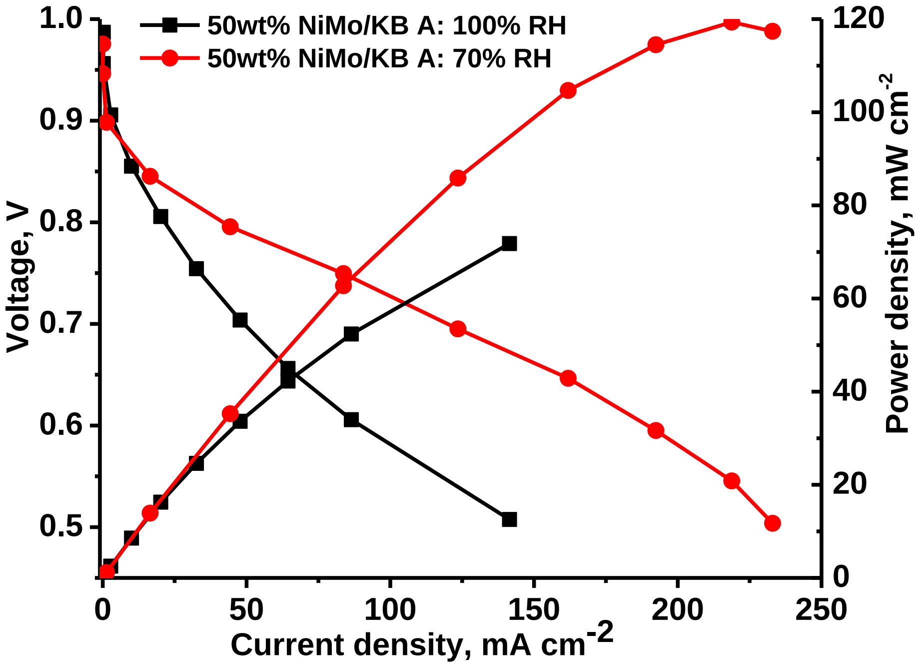

Figure 4.6: Fuel cell performance of MEA with NiMo/KB anode. Conditions: T_{cell}=70°C, RH=70 and 100°C, H_2 backpressure = 20 psi_g, Anode: NiMo/KB, 4 mg cm^{-2}, Cathode: Pd/C, 0.2 mg $cm^{-2}{}_{(Pd)}$.

The peak power density in case of the experiment at 100% RH on anode was ~70 $mWcm^{-2}$ while decreasing relative humidity to 70% resulted in an increase of the power density up to 120 $mWcm^{-2}$ at 0.5 V. Up to the authors best knowledge, this value is the highest from published in open literature. Previously the MEA performance of MEA completely free of PGM was reported by L. Zhuang group [89, 90]. Using NiW/C anode catalyst the researchers obtained ~35 mW cm^{-2} (at 0.5V and 60°C) [90]. The increase in the performance with the decrease of RH on the anode side can be explained by reducing the flooding effect, which occurs due to the electrochemical reactions in alkaline media:

$$2H_2 + 4OH^- \rightarrow 4H_2O + 4e^- \quad (15)$$

$$O_2 + 2H_2O + 4e^- \rightarrow 4OH^- \quad (16)$$

As it can be seen from Eq. 15 water is formed on the anode and having less humidification resulted in less water flooding at the anode. It should be noted that the reverse water balance in AEMFC compared to PEMFCs, evolution of water at the anode for AEMFC, requires a through re-design of anodic and cathodic catalyst layers to improve the mass transfer during operation.

MEA Tomography

Figure 4.7a shows a cross-section (tomograph) of the AEMFC operating at RH = 61%, the NiMo/KB anode catalyst layer is shown as the brightest zone in the cross-sectional image. It is evident from the three-dimensional volume rendering (Figure 4.7a, middle) that the catalyst layers and GDLs, as well, as channels have no liquid water present when the cell was operated at this lower humidity condition. This is also confirmed by the in-plane tomographs (Figure 4.7a, right), where the GDLs and catalyst layers' cracks are found to be free of liquid water. Figure 4.7b shows the corresponding tomographs and volume of the imaged AEMFC while operating the cell at 100 % RH. Both GDLs and the anode catalyst layer are found to be completely flooded. The three-dimensional volume rendering (Figure 4.7b, middle) also shows water present everywhere (gray areas) except in the channels. Comparing in-plane cross-section tomographs for RH = 100% (Figure 4.7b, right) to that of RH = 61% (Figure 4.7a, right), it is seen how water floods the GDLs and is present within some of the larger cracks of the catalyst layer. For clarity, segmented water within the GDLs is shown by Figure 4.7c (middle). The size resolution of micro-CT does not allow to resolving water within the nanopores of the catalyst layer, however averaging grey-scale value for the layer shows that it is entirely water-filled.

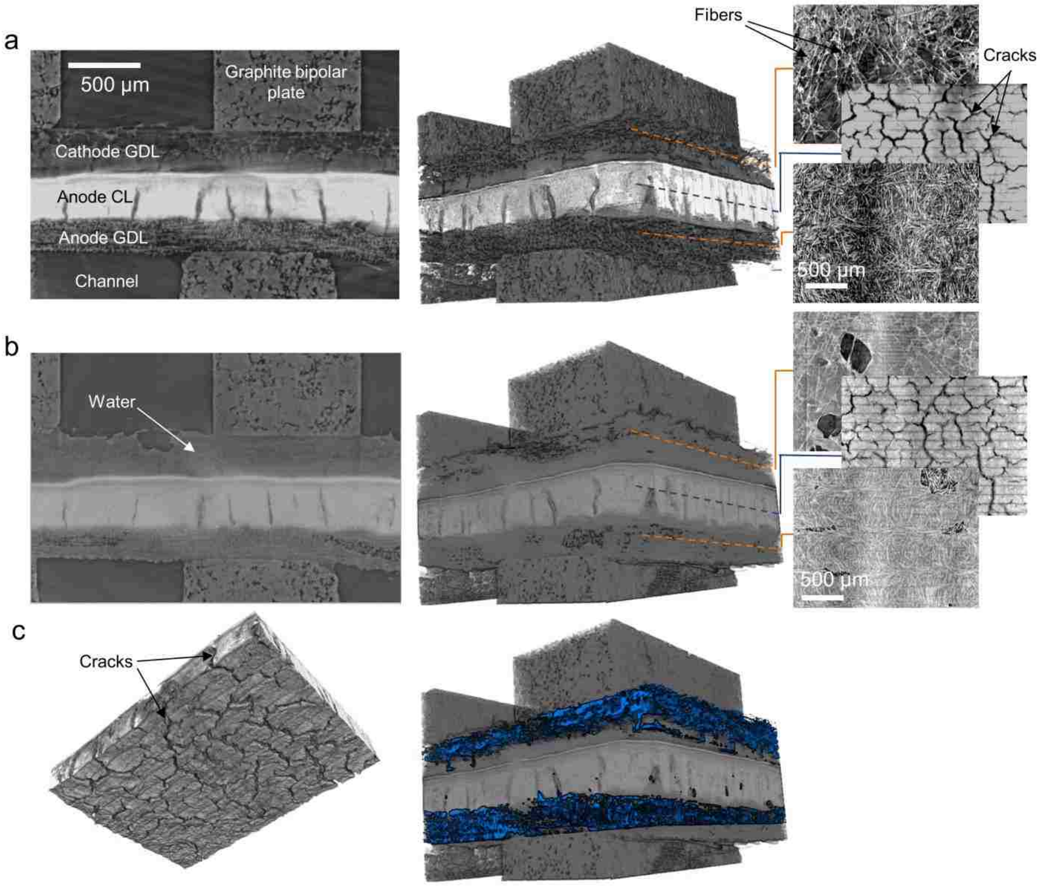

Figure 4.7: Cross-section tomograph of the MEA assembled within the in-operando X-ray CT cell with a) RH = 61% and b) RH = 100%, the images in the middle are volume-rendered views with in-plane cross-section tomographs (right). c) Volume-rendered view of the anode catalyst layer (left) and segmented view of water within the GDLs (middle).

The flooding observed while operating the cell near OCV at RH = 100% is due to the morphological and surface properties the NiMo/KB catalyst layer. For different catalysts but at similar test conditions and higher current densities (30 – 50 $mAcm^{-2}$), water droplets appeared at the interfaces and channels of the electrode producing water, shown in Figure 4.8b. For both AEMFCs and PEMFCs, no significant water flooding was observed as shown in Figure 4.8, whereas for NiMo/KB catalyst layer AEMFC water completely filled both GDLs. The most probable reason is local condensation within the catalyst layer, and given its thickness (250 μm), the layer acts as a water sponge, absorbing a significant amount of water that is further moved into the anode and cathode GDLs driven by the difference in capillary pressure between the catalyst layer and GDLs.

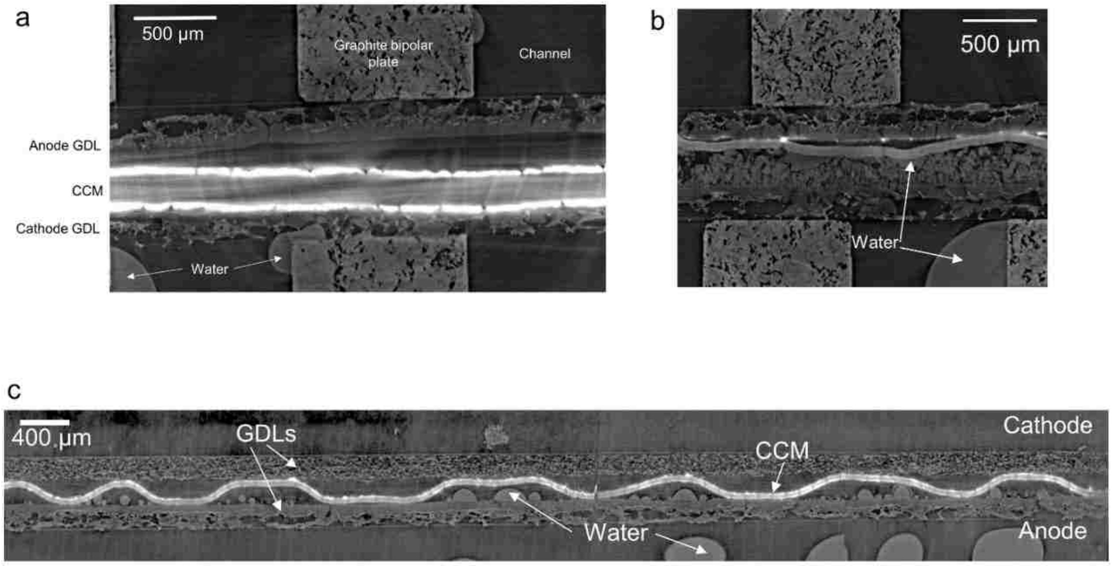

Figure 4.8: a) A cross-section tomograph of PEMFC with PGM MEA operating at 50 mA cm^{-2} and 100% RH, T = 30^{o}C, H_2/Air b) a cross-section tomograph of PGM-free cathode PEMFC operating at 30 mA cm^{-2}, 100% RH, T = 30^{o}C, H_2/air, and c) along-the-channel cross-section tomograph of PGM AEMFC at 30 mA/cm^{2}, 100% RH, T = 30^{o}C, H_2/O_2.

The morphology of the catalyst layer shows interconnected cracks with an average of 8.4 cracks/mm and average crack width of 12 µm. The volume-rendered structure of the anode catalyst layer is shown by Figure 4.7c (left), where the bottom surface showing the cracks is the side facing the MPL. These cracks act as low capillary pressure regions for water removal from the catalyst layer, and as is seen in Figure 4.7b (right) many of them are water-filled. The presence of water in the cathode GDL is encouraging, as it is needed as a reactant in ORR, however too much of water in both GDLs will result in mass-transport losses due to limited gas solubility and diffusion through liquid. This was confirmed by polarization curve in Figure 4.6, where decreasing RH on the anode side to 70% resulted in significant power density gain at higher current densities. Thick, hierarchicallystructured catalyst layers, with large water-storage capacity, is more susceptible to performance loss due to flooding (at high RH) rather than dehydration (at moderate RH).

MEA Durability

The durability data of MEA fabricated with NiMo/KB electrocatalysts is shown on Figure 4.9. As it can be clear seen the current density slowly increased at potential hold of 0.7V to maximum value of 55 mA cm^{-2}. Such a MEA activation was achieved for ~30 hours.

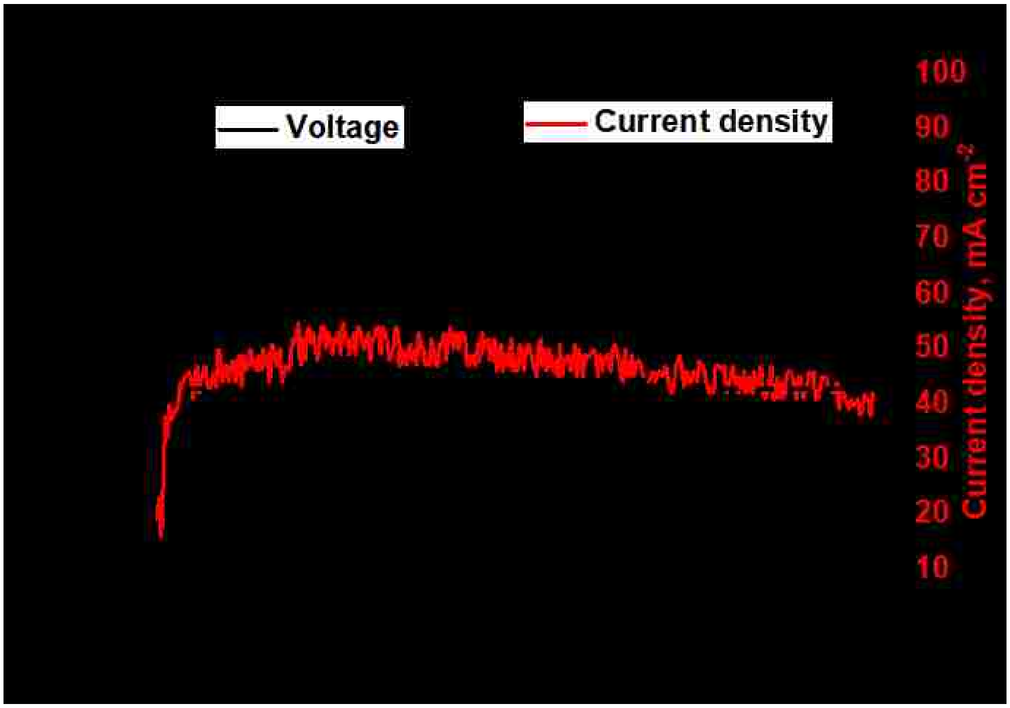

Figure 4.9: Durability study at potentiostatic hold of MEA with NiMo/KB anode. Conditions: T_{cell} = 60 °C, RH = 100 °C, H_2 backpressure = 20 psi_g, Anode: NiMo/KB, 4 $mgcm^{-2}$, Cathode: Pd/C, 0.2 $mgcm^{-2}{}_{(Pd)}$.

The performance slowly decreased to the level of Beginning of Life (BOL) after 80 hours of hold and this current density was stable for an additional 20 hours. The MEA activity started to decline insignificantly between 100 and 115 hours of experiment.

XPS analysis performed on the catalyst layer after the hold test shows significant chemical changes. First, Mo depletion from the surface was observed indicating that Mo had been leached from Ni. Second, the chemical state of Ni and remaining Mo indicates the metals exist in a significantly more oxidized state, as compared to beginning of life composition. To understand these findings, one must consider possible corrosion mechanisms of Ni and Ni alloys in alkaline environments. The Pourbaix diagram for nickel predicts a broad passivation region in pH ranges above 7. Here, Ni is expected to form a passivation layer of Ni oxides and hydroxides in the potential region of HOR in alkaline environments. Although this passivation is not expected result in losses of Ni due to chemical dissolution, the formation of the passivation layer will result in a loss of electrochemically active surface area, see Figure 4.3. This corrosion mechanism explains the XPS findings in that the Ni loses almost all metallic character, where the end of life state of Ni is almost entirely Ni oxide and hydroxide.

A second corrosion mechanism is a result of the chemical stability of Ni alloys. As previously mentioned, the strategy of increasing the mass activity of Ni towards anodic reactions has been to alloy Ni with more oxyphilic metals, such as Zn and Mo. Due to the larger oxidation potential of the alloying metal, galvanic corrosion becomes a concern. In the case of NiMo, Mo may become preferentially oxidized during HOR in alkaline environments. Unlike Ni, the Pourbaix diagram for Mo, as well as Zn, predict the formation of unstable oxyanions such as $(MoO_4)^{2-}$. These oxyanions do not form a passivation layer, rather they are subject to dissolution into the alkaline media upon formation. Therefore, the loss of Mo observed by XPS following the potential hold test can be explained by galvanic corrosion mechanisms which over time can lead catalyst deactivation.

Conclusion

PGM-free carbon supported NiMo electrocatalysts were synthesized and comprehensively characterized. The experimental parameters of the synthesis were selected to obtain relatively small catalyst particles at a high loading of active material on the Ketjenblack support. Judging from the intrinsic mass-weighted catalytic activity in the reaction of hydrogen electrooxidation (4.5 Ag^{-1}_{NiMo}) established by the RDE, NiMo/KB outperforms PGM-free catalysts reported elsewhere. For the first time, the peak power density obtained in fuel cell tests with AEM MEA achieved the value of 120 $mWcm^{-2}$, the highest power density reported with PGM-free anode catalysts to date. The comprehensive *in situ* imaging analysis was performed for the first time for alkaline exchange membrane fuel cell and revealed the complexity of water management in PGM-free thick anode layer. This catalyst material not only moves the state-of-the-art in PGM-free catalysts towards practically acceptable values but also charts the path for future improvements in the materials design. X-ray Micro-CT provide insight on the role of water formation, and transport of liquid water is critical in making the PGM-free AEMFC a choice technology for several product categories: portable, automotive and combined-heat-and-power generation. The fabricated electrodes were found to be durable in the aggressive potential hold conditions (0.7V) with insignificant activity losses after 115 hours of tests.

Chapter 5

NiCu/Ketjenblack -DENKA Black for Hydrogen Oxidation Reaction

In the pursuit of developing PGM-free anode catalysts for HOR, researchers have focused on nickel based catalysts due to the intrinsic catalytic activity towards HOR of Ni [133-135]. However, the reversible formation of $Ni(OH)_2$ under HOR conditions significantly hinders the mass activity of Ni towards HOR. NiCu supported on carbon has shown the most promise as a replacement for platinum at the anode for AEMFC's, with the highest reported mass activity exhibited for the composition $NiCu_{0.05}$ [136]. The role of Cu in the segregation and ECSA of Ni has been investigated [136-137], and exploration into the use of Ni supported on carbon nanotubes has been explored in efforts to improve the mass activity of Ni towards HOR [138].

In the previous sections, the development of NiMo supported on carbon was demonstrated to possess improved mass activity for HOR compared to Ni/C. It has been suggested that alloying Ni with Mo can reduce the binding energy of $-OH_{ads}$ on Ni sites. The reduction of this binding energy leads to increased reaction rates and an overall decrease in the overpotential for HOR. However, no detectable amounts of Mo were present in the bulk Ni phase, rather there is a segregation of Mo, in the form of Mo and NiMo oxides while XPS revealed the Ni surface is enriched in $NiMoO_x$.

When NiMo/C alloys were studied for hydrazine oxidation, it was clearly evident that alloying Ni with Mo dramatically improved the Ni mass activity for HH oxidation, with maximum activity occurring with Ni:Mo ratios near 9:1. However, the scalability of the synthesis of NiMo/C prepared by this method is poor, to say the least, due to spill-over during pyrolysis with urea. Here, the primary role of urea used in the NiMo synthesis is as a reducing agent, reducing Mo and Ni oxides rapidly and at temperatures where Mo carbide formation is less favorable. Therefore, replacing Mo with a metal less prone to carbide formation, such as Cu, will allow for the elimination of urea and thus improve the scalability of Ni alloys supported on carbon.

One final consideration is the solubility of Ni with the alloying metal. Figure 5.1 shows the phase diagram for the Ni-Cu system. Unlike the Ni-Mo and Ni-Zn system, the Ni-Cu system possesses full solubility within a single FCC phase.

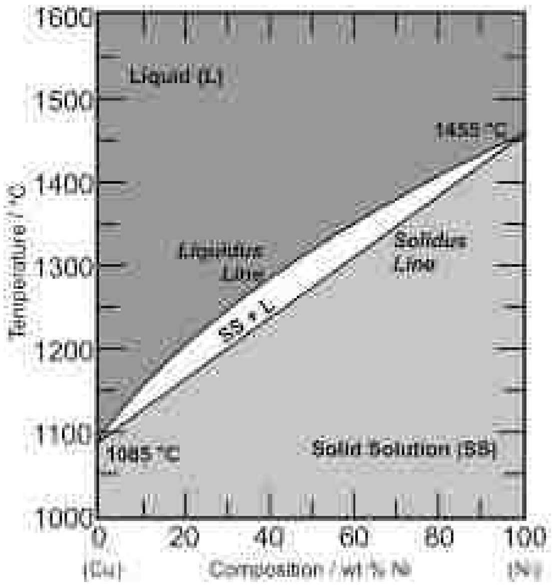

Figure 5.1: Phase diagram for the NiCu system.
http://www.spaceflight.esa.int/impress/text/education/Solidification/Phase_Diagrams.html

Although NiMo are fully soluble in the composition range used previously, segregation during processing leads to inhomogeneity of the Ni and Mo composition throughout the catalyst, which may result in regions of immiscibility (Figure 3.7). Therefore, the use of Cu as the alloying metal with Ni will not only lead to improved HOR activity, it will also lead to a more homogenous catalyst and make for a more facile and scalable synthesis.

Urea Method

First attempts of synthesizing NiMo/KB which were free of residual oxides were unscusseful. It was found that at temperatures below 600 °C were insufficient in reducing Mo oxides to metallic form during the pyrolysis in 7 at% H_2 of the metal precursors impregnated on carbon. Here, it must be recalled that removing the metal oxides by increasing the temperature is impossible, owing to the thermodynamic affinity of molybdenum with carbon above T = 741 K, which yields hexagonal molybdenum carbide (Mo_2C) [53]. Besides, neither MoO_2 nor Mo_2C are stable in the electrochemical conditions of a DHFC anode. Preventing their presence is consequently essential. Luhrs et al., [54] observed that urea was able to directly reduce molybdenum oxides into metallic molybdenum at high temperature under inert atmosphere, following a carbothermal reduction process (Eq. (13)) on MoO_2, where the CO group involved is provided by urea.

$$\mathrm{MoO_x + CO \rightarrow MoO_x + CO_2} \tag{17}$$

For this reason, urea was used to avoid the formation of crystalline molybdenum oxide (MoO_2). The duration of the heat-treatment was kept short (t = 1 h), assuming molybdenum reduction presents faster kinetics than molybdenum carbide formation at T = 600 °C or below. No crystalline molybdenum carbides and only residual levels of crystalline oxides were observed by X-ray diffraction after the synthesis (Figure 3.10), which supports this assumption (Table 3.3). The different peaks observed by XRD present patterns that are related to three identified structures, i.e. $(Ni_9Mo)_{0.4}$, $Ni_{0.16}Mo_{0.84}$ and MoO_2 (Figure 3.10).

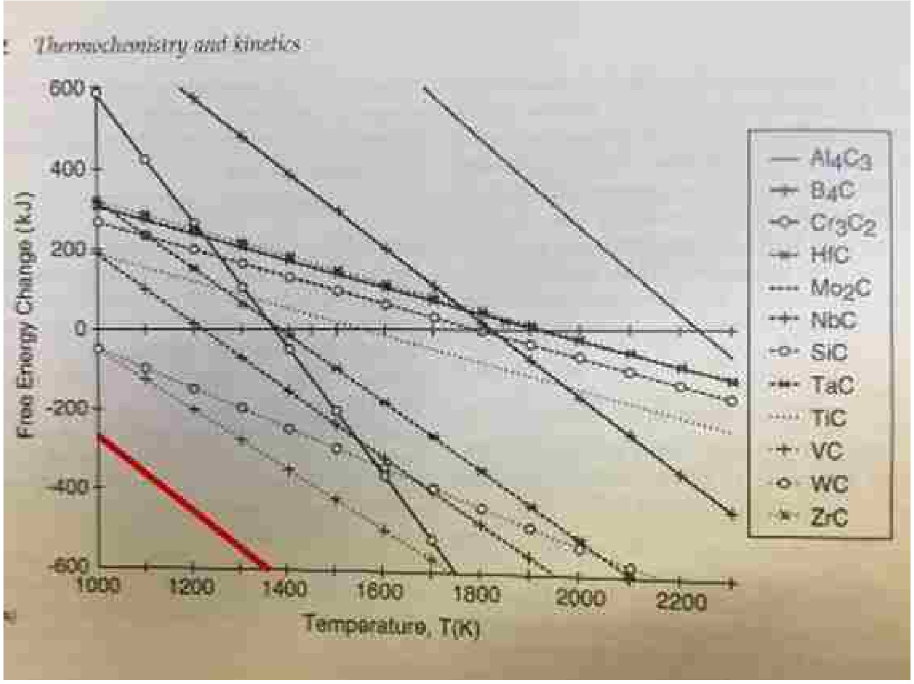

Figure 5.2: Free energy change as a function of temperature for the carbothermal reduction of various transition metals forming the metal carbides. The free energy change of reaction for Mo_2C is indicated in red [53].

NiCu/Ketjenblack Synthesis

NiCu/KB was synthesis using a wet impregnation method. First, Ni and Cu nitrates were dissolved in a minimal volume of deionized water then impregnated onto dried Ketjenblack carbon. After drying at ~50 °C for 18 hours, the material was finely ground using a mortar and pestle. Next, the catalyst starting material was pyrolyzed in 7 at. % H_2 at a temperature of 550 °C, where the ramp rate was 10 °Cmin^{-1}. After cooling to room temperature, the reactor was opened at one end and oxygen was allowed to diffuse in to passivate the freshly synthesized NiCu/KB.

NiCu/Ketjenblack Characterization

XRD

Analysis of the X-ray diffraction pattern for NiCu/KB shows a single FCC Ni phase with a lattice constant of 3.52 Å and an average crystallite size of 27 nm, calculated from whole pattern refinement. For comparison of the lattice parameter for pure Ni, a reference sample of 50 wt% Ni/KB was prepared and analyzed. Here, the lattice constant was also calculated as 3.52 Å. Applying Vegard’s rule, the amount of Cu in solid solution with Ni can be calculated from the linear combination of the pure FCC lattice constants of Ni [98-001-4691] and Cu [98-001-3667], being 3.516 Å and 3.615 Å respectively. The resulting lattice constant for a ratio of Ni to Cu of 95:5 is 3.520 Å. Due to random errors, the lattice expansion due to alloying Ni with Cu could not be measured, however the absence of amorphous or crystalline Cu phases suggests all copper is incorporated into the FCC Ni phase. The presence of amorphous Ni oxide and hydroxide phases is also evident in the Ni/KB XRD pattern, ~37° in 2-theta. Here, the Ni phase is clearly alloyed with copper and was done so without the addition of urea. Consequently, the yield from this synthesis is ~90% of theoretical and no spill-over occurred during pyrolysis.

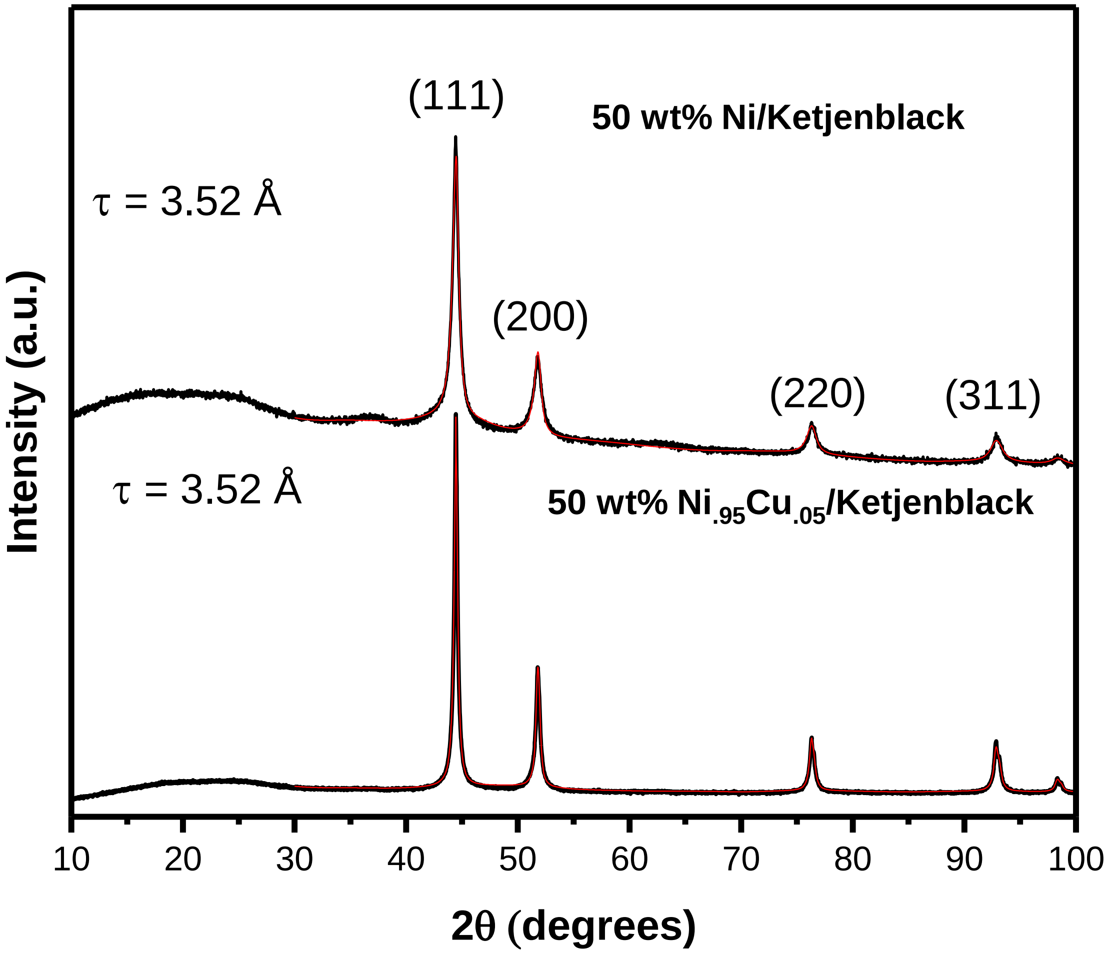

Figure 5.3: X-ray diffraction pattern for NiCu/KB (bottom) and Ni/KB (top) prepared by thermal reduction at T=550°C. The peak intensities are normalized to the (111) reflection. Pattern fits are overlaid on experimental data (red).

TEM

The morphology of the NiCu catalyst was investigated by TEM, where it was observed that the NiCu particles range in size from 8 nm to > 50 nm with an average particle size of 22 nm and standard deviation of 9 nm. Figure 5.4 (A, B, and D) show the NiCu nanoparticles are well dispersed on the carbon support with some agglomeration of the larger size particles, as shown in Figure 5.4.

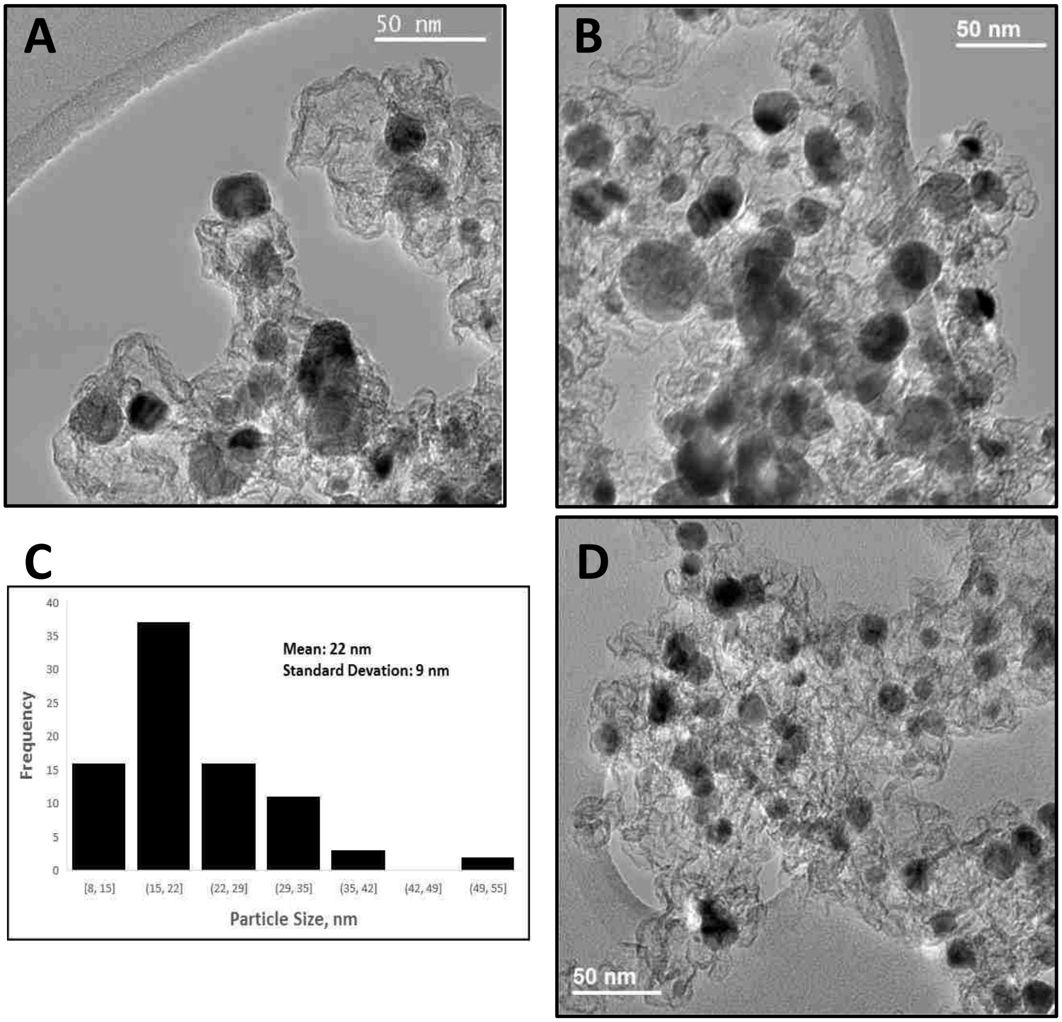

Figure 5.4: TEM images (A, B, and C) of $Ni_{0.9}Cu_{0.1}$/Ketjen Black and (C) corresponding particle size distribution of NiCu nanoparticles

Cyclic Voltammetry

Cyclic voltammetry was used to characterize the intrinsic activity towards HOR for NiCu/KB. All voltammograms are shown after subtraction of the capacitance current associated with Ketjenblack, as measured in 0.1M KOH with a scan rate of 5 mVs^{-1}. Figure 4A shows a comparison of 100 μg of metal loading on the working electrode in N_2 vs H_2 saturated electrolyte, confirming the activity of NiCu/KB towards HOR. At anodic potentials greater than 0.15 V vs. RHE, the decreasing limiting current observed is due to the formation of $Ni(OH)_2$, which passivates the catalyst surface and hinders HOR. This finding is consistent with previously reported observations [134].

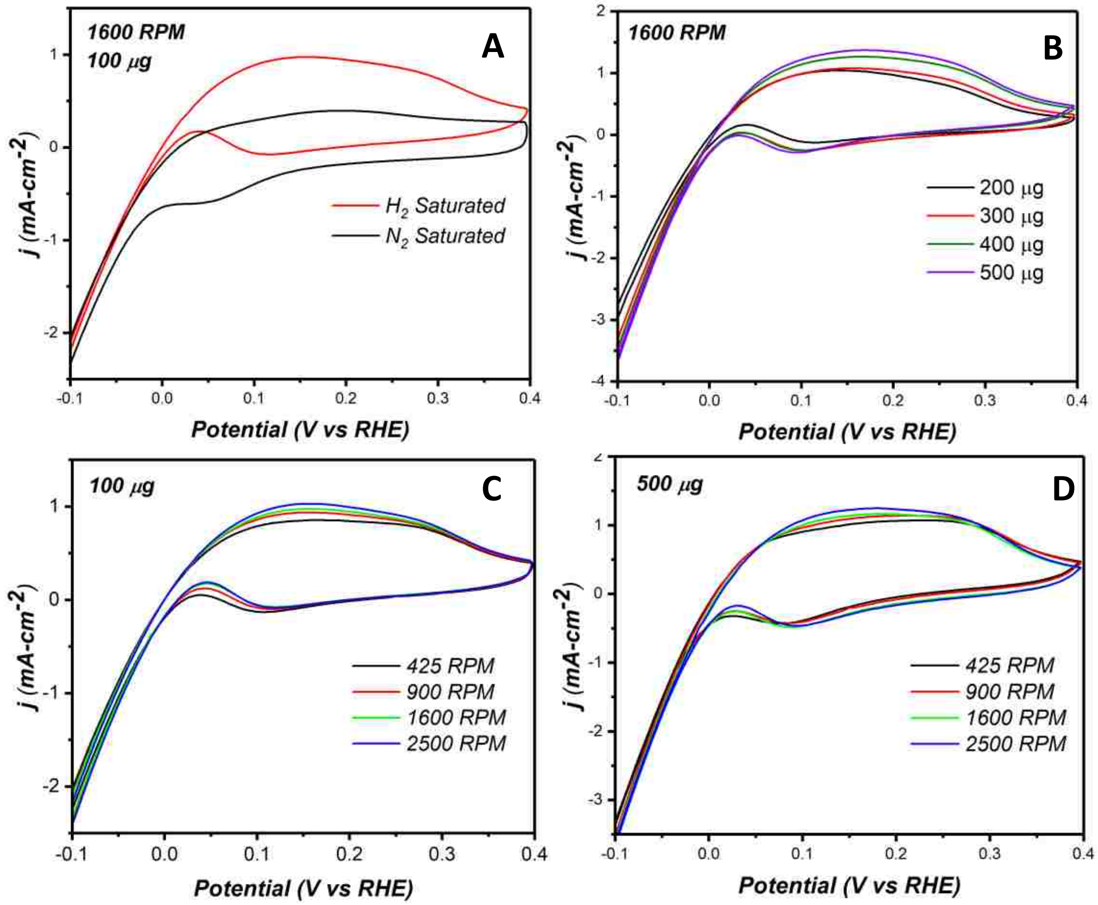

Figure 5.5: Cyclic Voltammetry Data showing: A) 100 μg loading of catalyst in N_2 and H_2 saturated 0.1M KOH, B) 200 μg – 500 μg loading of catalyst in H_2 saturated 0.1M KOH, C) 100 μg loading of catalyst in H_2 saturated 0.1M KOH at various rotation speeds, and D) 500 μg loading of catalyst in H_2 saturated 0.1M KOH at various rotation speeds. All data are shown after the subtraction of the capacitance current due to the carbon support.

MEA

The NiCu/KB was then tested in MEA, where the method of CCM preparation and testing was identical to that which is described for NiMo/KB. Using the same ionomer and conductive membrane, essentially replacing only the anode catalyst (from NiMo/KB to NiCu/KB) a nearly 3-fold increase in peak power density was achieved (Figure 5.6). This result in is strong agreement with the CV results reported earlier, predicting a 3-fold increase in activity based on the mass transfer limiting currents observed in the half-cell reaction.

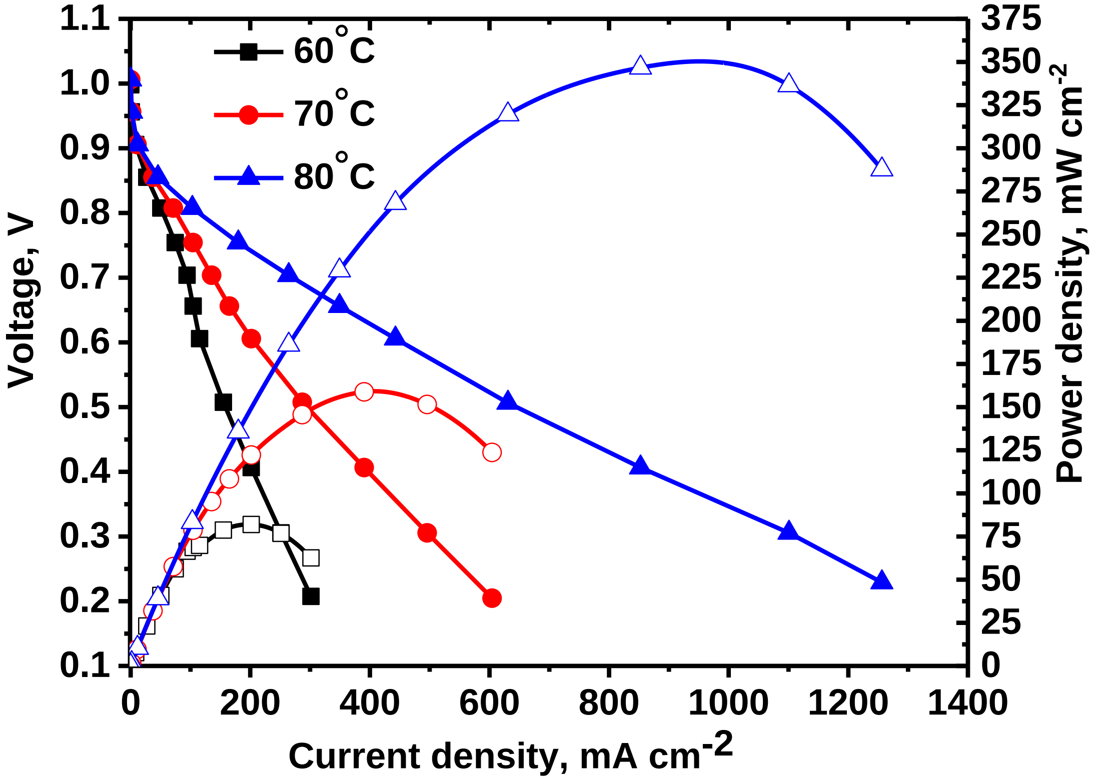

Figure 5.6: Fuel cell performance of MEA with NiCu/KB anode. Conditions: T_{cel1} = 70 °C, RH = 70 and 100°C, H_2 backpressure = 20 psi_g, Anode: NiCu/KB, 4 mgcm^{-2}, Cathode: Pd/C, 0.2 mgcm$^{-2}{}_{(Pd)}$

XPS

Figure 5.7 shows high-resolution Ni 2p and Cu 2p spectra obtained for Ni/KB and NiCu/KB samples. Elemental composition and relative distribution of nickel species are shown in Figure 5.7 C. The mixed sample has a smaller amount of oxygen detected, which is also reflected in the absence of hydroxides in NiCu/KB sample. The main peak in both

Ni/KB and NiCu/KB is due to nickel oxide. Content of metallic Ni, however, is much larger for alloyed sample and hydroxides are absent. Cu is mainly present as metallic Cu with a small amount of oxides detected.

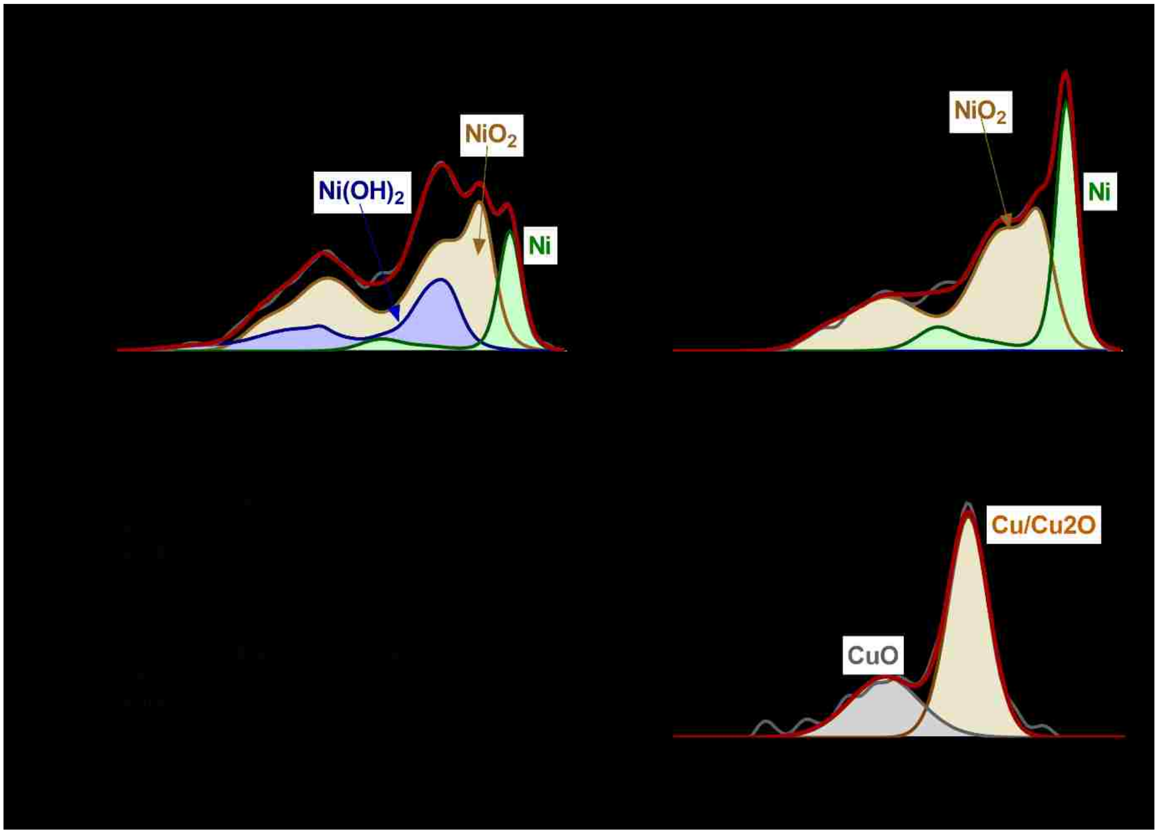

Figure 5.7: High resolution XPS spectra. Ni 2p for (A) Ni/KB and (B) NiCu/KB, (D) Cu 2p for NiCu/KB. (C) Elemental composition and Ni speciation.

NiCu/Ketjenblack Conclusion

It has been demonstrated that alloying of Ni with Cu leads to improved kinetics for HOR, consistent with what is reported in literature. The MEA performance of NiCu/Ketjenblack has shown significant gains in fuel cell performance as compared to NiMo/Ketjenblack, with a peak power density of 350 mWcm^2, as compared to 120 mWcm^2 for NiMo/Ketjenblack. The result sets a new benchmark for MEA performance of PGM-free anode catalysts for AEMFC's and establishes a platform from which future research efforts can build from in pursuit to achieve a sustainable hydrogen energy economy.

Influence of the Carbon Support

To investigate the influence of the carbon support, a commercially available carbon (DENKA Black) with complex graphitization and a larger fraction of low strain carbon than is typical for amorphous carbons, such as Ketjenblack, has been investigated as a more suitable support for NiCu. Here, DENKA carbon has been studied as a means of stabilizing more reduced NiCu, due to the Lewis basicity of π-π stacking in the graphitic layers, to prevent the formation of parasitic $Ni(OH)_2$ during HOR in alkaline conditions. A modification to the urea method was also tested, where samples were prepared with a reducing agent, 4-aminoantipyrine (AApyr). AApyr was chosen due to the more controlled decomposition under pyrolyitic conditions, as compared to urea, leading to less spill-over and higher catalysts yields.

NiCu/DENKA Black Synthesis

The synthesis for NiCu/DENKA was prepared with similar procedures used for NiCu/KB, with only a few modifications. AApyr, 150 $mg/g_{catalyst}$ was dissolved along with the metal nitrates prior to impregnation onto the carbon support. The temperature time trajectory was also modified to control the rate of decomposition of AApyr. Once dried, the catalyst starting material was pyrolyzed in 7 at. % H_2, N_2 balance, at 550 °C. The reactor was heated at a rate of 10 ° $Cmin^{-1}$ to 150 °C, then 2 °$Cmin^{-1}$ to 250 °C and held for 30 min, followed by 5 °$Cmin^{-1}$ to 550 °C and held for 1 hr.

NiCu/DENKA Black Characterization

TEM

High resolution TEM imaging was performed to characterize the particle and carbon morphology. Figure 5.8 shows TEM micrographs for NiCu/DENKA-AApyr and NiCu/Ketjenblack. For all catalyst samples, the NiCu particles show no segregation as the particles are well dispersed onto the carbon supports. However, a clear distinction between the carbon supports was apparent where a significant amounts of low strain (graphitic) carbon was found in the DENKA supported catalyst. This ordered carbon is shown in Figure 5.8(A, B) where fringes are clearly present in the DENKA carbon. The inset in Figure 1A shows the electron diffraction pattern obtained by Fast Fourier transform (FFT) of a selected area of a NiCu particle. The diffraction pattern was indexed as the (111) and (200) reflections of FCC Ni, demonstrating that the NiCu particles are imbedded into the low strain DENKA carbon. Similarly, NiCu particles are shown imbedded into the amorphous Ketjenblack support, Figure 5.8(B, C).

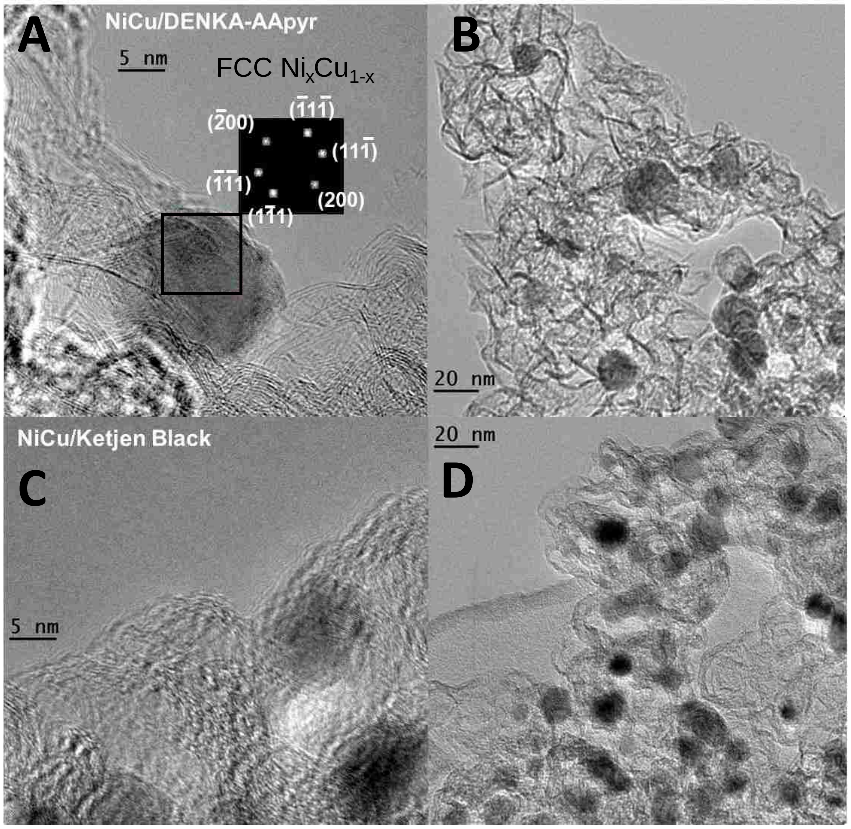

Figure 5.8: A) HRTEM image of A, B) NiCu/DENKA, and C, D) NiCu/Ketjenblack. Inset for Figure 1A shows the selected area FFT of a NiCu particle indexed as the (111) and (200) reflections of FCC Ni.

XRD

The bulk composition of the NiCu/carbon catalysts was determined by X-ray diffraction, shown in Figure 5.9A. Whole pattern refinement was performed, and the calculated diffraction patterns are overlaid in green. All catalysts show a single FCC Ni phase with no crystalline oxides. Bulk oxides are not desired as the activity towards HOR for Ni oxide/hydroxide is much less than for metallic NiCu [136]. The lattice constant for NiCu in each catalyst was determined to be 3.52 Å, which is ~0.1 % expansion in the lattice constant compared to pure FCC Ni. Although this expansion is consistent with the linear combination of the Ni and Cu lattice constants for 5 at. % Cu (3.516 Å and 3.615 Å respectively), random errors prevent the exact determination of Cu content. The average crystallite size was calculated by fitting the peak broadening and the results are summarized in Table 5.1.

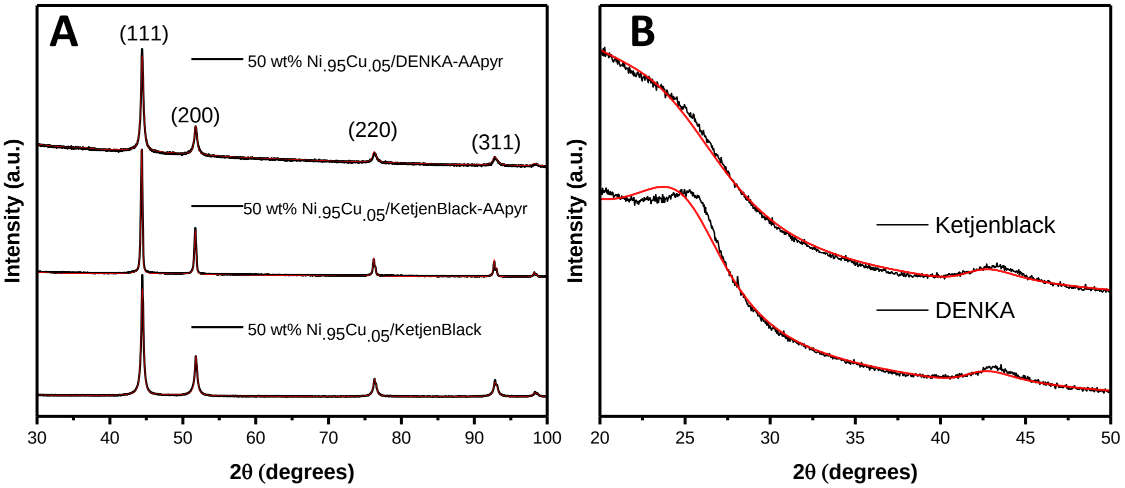

Figure 5.9: A) XRD patterns for NiCu supported on: DENKA-AApyr, Ketjenblack-AApyr, and Ketjenblack, and B) XRD patterns for DENKA and Ketjenblack. Calculated patterns from pattern refinement are overlaid in green.

Table 5.1: Lattice constants and average crystallite size for NiCu supported on Ketjenblack and DENKA determined by XRD pattern refinement.

	Lattice Constant (Å)	Average Crystallite Size (nm)
NiCu/DENKA-AApyr	3.52	21
NiCu/Ketjenblack-AApyr	3.52	61
NiCu/Ketjenblack	3.52	33

To analyze and compare structural parameters of Ketjenblack and DENKA, CarbonXS GUI was used to refine the x-ray diffraction patterns of the carbon supports [137]. CarbonXS GUI is a modified version of CarbonXS, a Fortran 77 program developed in 1993 by Shi, Reimers, and Dahn [138], with a graphical user interface which runs on

Windows 7, MAC OSX, and Linux. The program models 2D layers of carbon allowing for the refinement of structural parameters, including: in plane lattice constant (L_c), interlayer spacing (d_{002}), lateral coherence (L_a), the number of layers in the vertical direction (M), and the fraction of low strain carbon (g). Figure 2B shows diffraction patterns for Ketjenblack and DENKA, obtained with a continuous scan rate of 0.8 °/min, with the calculated patterns obtained from CarbonXS GUI overlaid in green. The graphitic (002) peak (~26° in 2θ) shows less line broadening for DENKA compared to Ketjenblack, indicating a larger stacking number for DENKA carbon than for Ketjenblack (162.4 and 93.6 respectively) [139]. Additionally, DENKA has a higher amount of low strain carbon than Ketjenblack, where $g_{DENKA} = 0.354$ compared to $g_{Ketjenblack} = 0.239$. Table 5.2 shows the refined structural parameters for DENKA and Ketjenblack carbons obtained from Carbon XS GUI.

Table 5.2: Structural parameters for DENKA and Ketjenblack calculated from XRD pattern refinement performed in CarbonXS GUI.

Structural Parameter	DENKA	Ketjenblack	Units
L_c	2.46	2.47	Å
$d_{(002)}$	3.46	3.47	Å
L_a	51.6	60.9	Å
M	162.4	93.6	# of Layers
g	0.354	0.239	Fraction of Low Strain Carbon

XPS

The near surface composition of the NiCu catalysts was studied using XPS, here the penetration depth for Ni 2p and Cu 2p is 2.4 nm and 2 nm respectively. It should be noted that for particles on the order of 5 nm, the XPS spectra should be considered as representative of the bulk composition. The XPS spectra for Ni 2p was fitted to three Ni species: NiO_2, $Ni(OH)_2$, and metallic Ni. Figure 5.10(A, B) show that the content of Ni oxide and hydroxide species is much larger on the Ketjenblack support as compared to that of NiCu supported on DENKA-AApyr. Similarly, the Cu 2p spectra show much larger amounts of reduced Cu for samples supported on DENKA-AApyr.

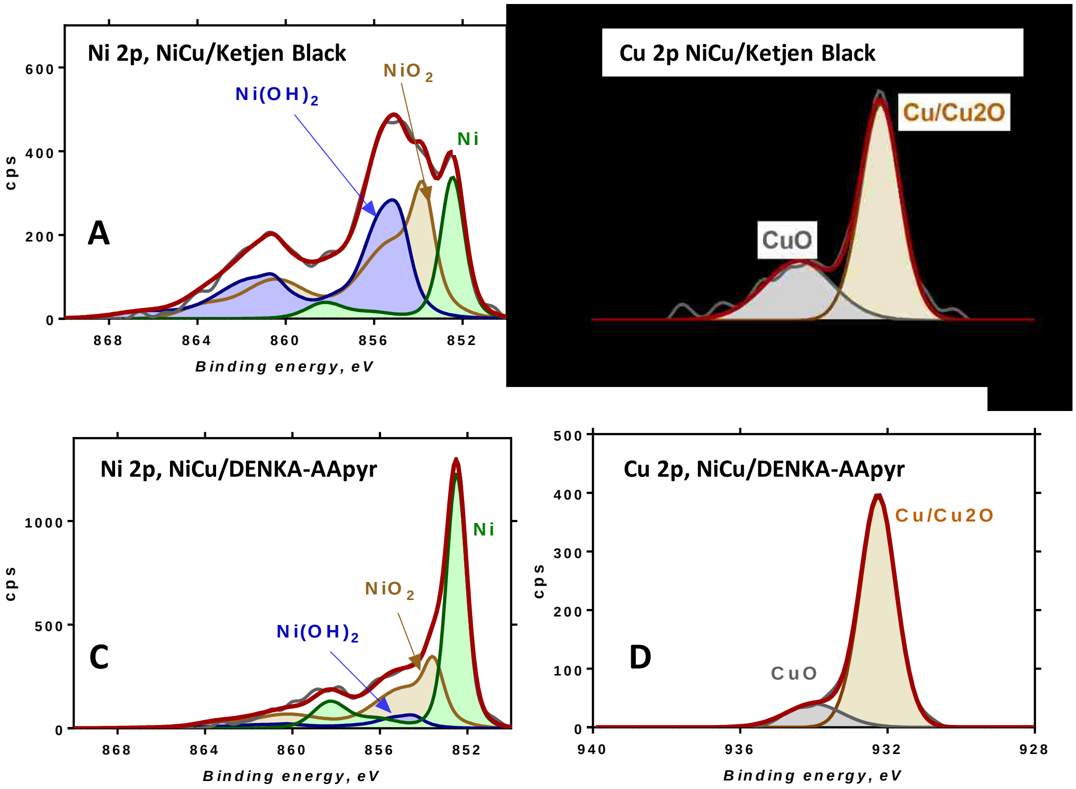

Figure 5.10: XPS spectra showing A) Ni 2p spectra for NiCu/Ketjenblack, B) Cu 2p for NiCu/Ketjenblack, C) Ni 2p for NiCu/DENKA-AApyr, and D) Cu 2p for NiCu/DENKA-AApyr. The raw data are shown outlined in grey, the fitted spectra shown outlined in red, and the fitted peaks shown in the shaded regions.

Cyclic Voltammetry

HOR activity for the NiCu/catalysts, characterized by cyclic voltammetry, is shown in Figure 5.11. The hydrogen adsorption region (0.0 – 0.15 V vs RHE) show larger hydrogen adsorption for NiCu/DENKA and DENKA-AApyr compared to NiCu/Ketjenblack. The difference between hydrogen adsorption on NiCu/DENKA vs NiCu/Ketjenblack can be explained by the reaction rate of hydrogen adsorption being several orders of magnitude lower on non-noble metals covered by an amorphous oxide film than for the pure metal, where the reaction follows a Volmer mechanism with the adsorption energy for M-H being much stronger for the metal compared to the metal oxide [140-141]. The exchange current densities between the HER and HOR also show a trend of lower overpotential for HOR for NiCu supported on DENKA and DENKA-AApyr than for NiCu/Ketjenblack, with the maximum current density for HOR on NiCu/DENKA-AApyr being more than twice that of NiCu/Ketjenblack. These trends in HOR activity on NiCu/carbon catalysts, along with results obtain from XPS analysis, indicate that the activity of NiCu towards HOR is greatly influenced by the metallic content of the metal species.

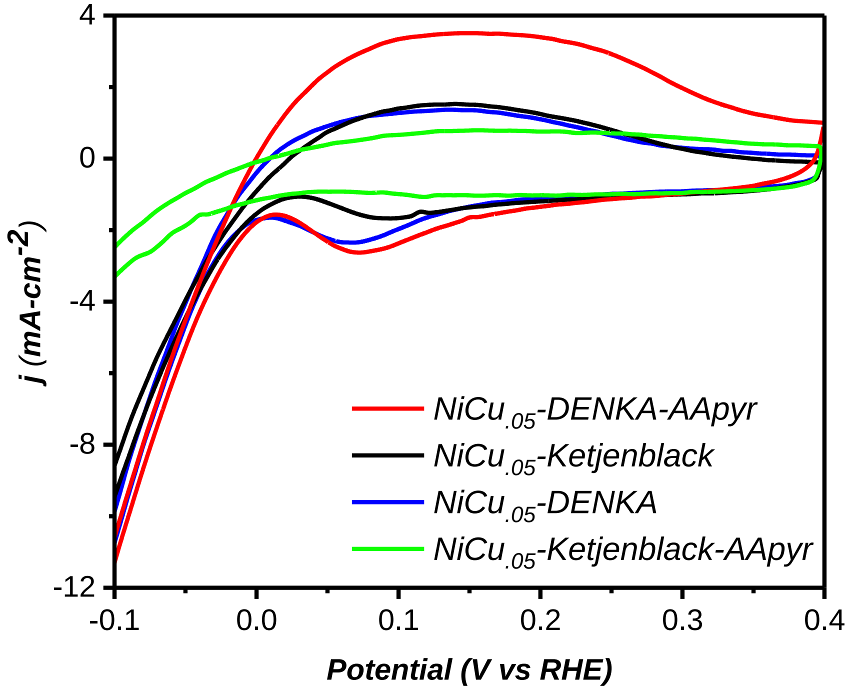

Figure 5.11: Cyclic voltammograms performed in H_2 saturated O.1M KOH with a rotation rate of 1600 RPM for various NiCu/carbon catalysts. All experiments were performed with a loading of 100 μg of metals on the working electrode.

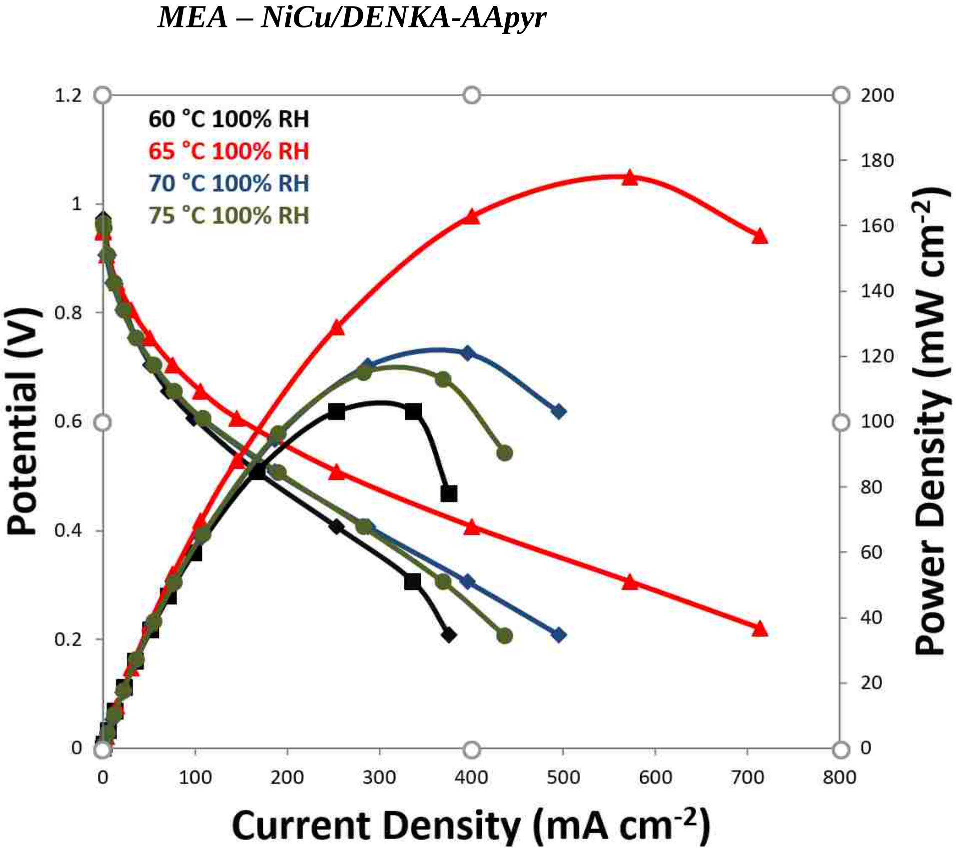

Figure 5.12: Fuel cell performance of MEA with NiCu/DENKA-AApyr anode. Conditions: RH=100 and 100 °C, H_2 backpressure = 20 psi_g, Anode: NiCu/DENKA-AApyr, 4 $mgcm^{-2}$, Cathode: Pd/C, 0.4 $mgcm^{-2}{}_{(Pd)}$

Figure 5.12 shows power curves obtained for NiCu/DENKA-AApyr at temperatures from 50-75 °C. The MEA performance was found to peak at 70 °C, above which rapid degradation was observed and the performance was not recoverable. This result is likely due to the degradation of the ionomer during the ion exchange reaction, where ammonia was used as the hydroxyl source rather than KOH in an attempt to reduce sedimentation of residual KOH. This method of activation, although thought to induce chemical degradation of the ionomer, was shown to decrease the break-in period for the MEA, requiring less than 24 hrs. to achieve full activation whereas previously the break-in occurred over the course of several days.

The key result here lies in the dramatic improvement in power density as a function of temperature, as compared to NiMo/KB, where an approximate 40% increase in power density was demonstrated at temperatures near 60-65 °C.

NiCu/DENKA Black Conclusions

The influence of the carbon support for NiCu HOR catalysts was examined. DENKA Black, a commercial carbon with complex graphitization, was used as a support material for NiCu and compared to Ketjenblack. A reducing agent, 4-aminoantipyrine, was used *in situ* to prevent the formation of amorphous Ni oxides and hydroxides. X-ray diffraction analysis of the carbon supports revealed a larger fraction of low strain carbon in DENKA, as compared to Ketjenblack, with a larger stacking number of carbon layers in the vertical direction. XPS analysis revealed that the Ni and Cu species are more reduced (lower amounts of amorphous oxides and hydroxides) for NiCu supported on DENKA-AApyr than for NiCu/Ketjenblack. Cyclic voltammetry revealed a correlation between the metallic content of the catalyst and activity towards HOR, where hydrogen adsorption and HOR activity are significantly improved on the NiCu catalysts containing lower amounts of oxides and hydroxides. These results illustrate how the activity of PGM-free NiCu catalysts for HOR in alkaline media can be tuned and improved by stabilizing reduced Ni and Cu species on carbons containing a larger fraction of low strain (graphitic) carbon. The effect is likely due to the Lewis-basicity resulting from π-π stacking in the low strain carbon layers.

Chapter 6

Concluding Remarks

Carbon Supported NiZn for Hydrazine Oxidation

Unsupported NiZn for hydrazine oxidation has previously been shown to possess increased mass activity compared to Ni, as well as a lower the overpotential, for hydrazine oxidation. Improving upon this work, it has been demonstrated that the use of a carbon support can drastically improve the activity of NiZn by increasing the electrochemical surface area of NiZn and lowering the mass transfer resistance of the catalyst. A two-step kinetic mechanism was proposed and subsequently proven using infrared adsorption spectroscopy during *in situ* half-cell measurements. As a result, a better understanding of the reaction pathway has enabled a more deliberate methodology to be adopted in the design of hydrazine oxidation catalysts to improve the selectivity and thus, the utility of the fuel.

NiMo for Hydrazine Oxidation

A novel method for the synthesis of carbon supported NiMo nanoparticles was achieved to prevent the formation of undesired oxide and carbide species using an *in situ* reducing agent (urea). The successful alloying of Ni and Mo resulted in highly active catalysts for HH oxidation in alkaline media. Alloying Ni with Mo was proven to stabilize the N-N hydrazine bond to provide greater selectivity of the catalyst towards N_2, resulting in improved utility of the fuel. These results significantly improve the prospect for commercialization of the direct hydrazine fuel cell by replacing PGM electrodes with inexpensive and Earth abundant materials. This work not only makes alkaline fuel cells more affordable, but is also a significant step towards sustainable and environmentally friendly energy.

NiMo for Hydrogen Oxidation

Drawing inspiration from knowledge gained by the previous studies of NiMo for HH oxidation in alkaline media, carbon supported NiMo was adapted for use as a hydrogen oxidation catalyst in AEMFC's. The successful integration of NiMo HOR catalysts in anion exchange MEA's demonstrated world record power density, 120 $mWcm^2$. Furthermore, investigations into water management using *In-operando* X-ray Micro CT imaging offers considerable insight into the challenges of catalyst layer design for AEMFC's. This work is a huge step forward in the development of PGM-free fuel cells and outlines the path forward to realize the wide spread use of alkaline fuel cells as a replacement to fossil fuels and the internal combustion engine.

NiCu for Hydrogen Oxidation

The ability to tune catalytic activity of Ni towards anodic reactions for AEMFC's through alloying with secondary metals such as Zn, Mo, and Cu, has been proven to be an effective and powerful technique in the design of highly active PGM-free anodic catalysts. In the quest to match the catalytic activity of PGM catalysts using Earth abundant and commercially available materials, an additional strategy has been successfully developed which focuses on the influence of the carbon support. DENKA carbon, a type of acetylene black with a high graphitic content, has been used as a replacement for amorphous Ketjenblack. The Lewis basicity of DENKA due to pi-pi stacking in the graphitic layers, was shown to improve the mass activity of NiCu by stabilizing Ni and Cu in a highly reduced form. An *in situ* reducing agent, 4-aminoantipyrine, was used to aid in the reduction of intermediate Ni and Cu oxide phases, in a way which allows for lower synthesis temperatures and high catalyst yields. The use of a graphitized support, along with the *in situ* reducing agent, results in a 3-fold improvement in current density as compared to NiCu supported on Ketjenblack. This result is the highest reported current density achieved for any PGM-free HOR catalyst in alkaline media.

References:

1. H.A. Gasteiger, W. Vielstich, H. Yokohama, Handbook of Fuel Cell, John Wiley Chichester, 2009.
2. W. Vielstich, A. Lamm, H.A. Gasteiger, Handbook of Fuel Cell, Wiley Chichester, 2003.
3. J.X. Wang, C. Ma, Y. Choi, D. Su, Y. Zhu, P. Liu, R. Si, M.B. Vukmirovic, Y. Zhang, R. R. Adzic, J. Am. Chem. Soc. 133 (2011) 13551–13557.
4. Y. Zhang, C. Ma, Y. Zhu, R. Si, Y. Cai, J.X. Wang, R.R. Adzic, Catal. Today 202 (2013) 50–54.
5. K. Kuttiyiel, K. Sasaki, D. Su, M.B. Vukmirovic, N.S. Marinkovic, R.R. Adzic, Electrochim. Acta 110 (2013) 267–272.
6. L. Dubau, M. Lopez-Haro, L. Castanheira, J. Durst, M. Chatenet, P. Bayle-Guillemaud, L. Guétaz, N. Caqué, E. Rossinot, F. Maillard, Appl. Catal. B Environ. 142–143 (2013) 801–808.
7. C. Cui, L. Gan, M. Heggen, S. Rudi, P. Strasser, Nat. Mater. 12 (2013) 765–771.
8. L. Dubau, T. Asset, R. Chattot, C. Bonnaud, V. Vanpeene, J. Nelayah, F. Maillard, ACS Catal 5 (2015) 5333–5341.
9. K. Asawasa, K. Yamamoto, K. Yamada, H. Tanaka, D. Matsumura, K. Tamura, Y. Nishihata, P. Atanassov, Electrochem. Soc. Trans. 33 (2010) 1751–1755.
10. U. Tylus, Q. Jia, K. Strickland, N. Ramaswamy, A. Serov, P. Atanassov, S. Mukerjee, J. Phys. Chem. C 118 (2014) 8999–9008.
11. C. Choi, C. Baldizzone, J. Grote, A. Schuppert, F. Jaouen, K.J. Mayhofer, Angew. Chemie Int. Ed 54 (2015) 12753–12757.
12. P. Gode, F. Jaouen, G. Lindbergh, A. Lundblad, G. Sundholm, Electrochim. Acta 48 (2003) 4175–4187.
13. Z. Li, B. Liu, K. Arai, S. Suda, J. Electrochem. Soc. 150 (2003) A398–A402.
14. R. Raman, N. Choudhury, A. Shulka, Electrochem. Solid-State Lett. (2004) A488-A491.
15. J.B. Lakeman, A. Rose, K.D. Pointon, D.J. Browning, K.V. Lovell, S.C. Waring, J.A. Horsfall, J. Power Sources 162 (2006) 765–772.
16. P.Y. Olu, F. Deschamps, G. Caldarella, M. Chatenet, N. Job, J. Power Sources 297 (2015) 492–503.
17. C. Ponce de Leon, F. Walsh, Ref. Modul. Chem. Mol. Sci. Chem. Eng. Elsevier (2015).

18. K. Yamada, K. Asawasa, K. Yasuda, T. Ioroi, H. Tanaka, Y. Miyasaki, T. Kobayashi, J. Power Sources 115 (2003) 236–242.

19. N.V. Rees, R.G. Compton, J. Solid State Electrochem. 15 (2011) 2095–2100.

20. A. Serov, M. Padilla, A.J. Roy, P. Atanassov, T. Sakamoto, K. Asazawa, H. Tanaka, Angew. Chemie – Int. Ed. 53 (2014) 10336–10339.

21. K. Asazawa, K. Yamada, H. Tanaka, A. Oka, M. Taniguchi, T. Kobayashi, Angew. Chem. Int. Ed. Engl. 46 (2007) 8024–8027.

22. A. Serov, C. Kwak, Appl. Catal. B Environ. 98 (2010) 1–9.

23. V. Rosca, M. Duca, M.T. de Groot, M.T.M. Koper, Chem. Rev. 109 (2009) 2209 – 2244.

24. T. Sakamoto, K. Asazawa, K. Yamada, H. Tanaka, Catal. Today 164 (2011) 181–185.

25. T. Sakamoto, K. Asazawa, J. Sanabria-Chinchilla, U. Martinez, B. Halevi, P. Atanassov, P. Strasser, H. Tanaka, J. Power Sources 247 (2014) 605–611.

26. U. Martinez, K. Asazawa, B. Halevi, A. Falase, B. Kiefer, A. Serov, M. Padilla, T. Olson, A. Datye, H. Tanaka, P. Atanassov, Phys. Chem. Chem. Phys. 14 (2012) 5512–5517.

27. T. Sakamoto, K. Asazawa, U. Martinez, B. Halevi, T. Suzuki, S. Arai, D. Matsumura, Y. Nishihata, P. Atanassov, H. Tanaka, J. Power Sources 234 (2013) 252–259.

28. B. Filanovsky, E. Granot, I. Presman, I. Kuras, F. Patolsky, J. Power Sources 246 (2014) 423–429.

29. K. Asazawa, T. Sakamoto, S. Yamaguchi, K. Yamada, H. Fujikawa, H. Tanaka, K. Oguro, J. Electrochem. Soc. 156 (2009) B509–B512.

30. J. Sanabria-Chinchilla, K. Asazawa, T. Sakamoto, K. Yamada, H. Tanaka, P. Strasser, J. Am. Chem. Soc. 133 (2011) 5425–5431.

31. N.V. Rees, R.G. Compton, Energy Environ. Sci. 4 (2011) 1255–1260.

32. S. Karp, L. Meites, J. Am. Chem. Soc. 84 (1962) 906–912.

33. M. Petek, S. Bruckenstein, J. Electroanal. Chem. Interfacial Electrochem. 47 (1973) 329–333.

34. M. Fleischmann, K. Korinek, D. Pletcher, J. Electroanal. Chem. Interfacial Electrochem. (1972) 499–503.

35. T. Sakamoto, H. Kishi, S. Yamaguchi, D. Matsumura, K. Tamura, A. Hori, Y. Horiuchi, A. Serov, K. Artyushkova, P. Atanassov, H. Tanaka, J. Electrochem. Soc. (2016) in press.

36. J. Barrault, C. Batiot, L. Magaud, M. Ganne, World Congr Oxid. Catal. 3 (1997) 375–382.

37. M.P. Astier, G. Dji, S.J. Teichner, Appl. Catal. 72 (1991) 321–329.

38. J.P. Perdew, K. Burke, M. Ernzelhof, Phys. Rev. Lett. 77 (1996) 3865–3868.

39. J.P. Perdew, K. Burke, M. Ernzelhof, Phys. Rev. Lett. 78 (1997) 1396–1400.

40. P.E. Blöchl, Phys. Rev. 50 (1994) 17953–17979.

41. G. Kresse, D. Joubert, Phys. Rev. B 59 (1999) 1758–1775.

42. G. Kresse, J. Hafner, Phys. Rev. B 47 (1993) 558–561.

43. G. Kresse, J. Hafner, Phys. Rev. B 49 (1994) 14251–14269.

44. G. Kresse, J. Furthmüller, Comput. Mat. Sci. 6 (1996) 15–50.

45. G. Kresse, J. Furthmüller, Phys. Rev. B 54 (1996) 11169–11186.

46. H.J. Monkhorst, J.D. Pack, Phys. Rev. B Condens. Matter. Mater. Phys. 13 (1976) 5188–5192.

47. M. Methfessel, A.T. Paxton, Phys. Rev. B 40 (1989) 3616–3621.

48. D.A. Konopka, M. Li, K. Artyushkova, N. Marinkovic, K. Sasaki, R. Adzic, T.L. Ward, P. Atanassov, J. Phys. Chem. C 115 (2011) 3043–3056.

49. A. Serov, A. Aziznia, P.H. Benhangi, K. Artyushkova, P. Atanassov, E. Gvenge, J. Mater. Chem. A 1 (2013) 14384–14391.

50. A. Serov, M.H. Robson, M. Smolnik, P. Atanassov, Electrochim. Acta 109 (2013) 433–439.

51. M.H. Robson, A. Serov, K. Artyushkova, P. Atanassov, Electrochim. Acta 30 (2013) 656–655.

52. A. Serov, M.H. Robson, M. Smolnik, P. Atanassov, Electrochim. Acta 80 (2012) 213–218.

53. A.W. Weimer, Carbide, Nitride and Boride Materials Synthesis and Processing, Chapman and Hall, London, 1997.

54. C. Luhrs, M. Kane, Z. Leseman, J. Phillips, Metall. Mater. Trans. B 44 (2012) 115–122.

55. T. Sakamoto, P. Deevanhxay, K. Asazawa, S. Tsushima, S. Hirai, H. Tanaka, J. Power Sources 2014, 252, 35 – 42.

56. T. Sakamoto, K. Asazawa, J. Sanabria-Chinchilla, U. Martinez, B. Halevi, P. Atanassov, P. Strasser, H. Tanaka, J. Power Sources 2014, 247, 605 – 611.

57. T. Sakamoto, K. Asazawa, U. Martinez, B. Halevi, T. Suziki, S. Arai, D. Matsumura, Y. B. Nishihata, P. Atanassov, H. Tanaka, J.Power Sources 2013, 234, 605 – 611.

58. S.-I. Yamazaki, Z. Siroma, N. Fujiwara, M. Asahi, K. Asazawa, H. Tanaka, T. Ioroi, Electrochim. Acta 2013, 94, 38 – 41.

59. U. Martinez, K. Asazawa, B. Halevi, A. Falase, B. Kiefer, A. Serov, M. Padilla, T. Olson, A. Datye, H. Tanaka, P. Atanassov, Phys. Chem. Chem. Phys. 2012, 14, 5512 – 5517.

60. J. Sanabria-Chinchilla, K. Asazawa, T. Sakamoto, S. Yamaguchi, K. Yamada, H. Tanaka, P. Strasser, J. Am. Chem. Soc. 2011, 133, 5425 – 5431.

61. K. Asazawa, T. Sakamoto, S. Yamaguchi, K. Yamada, H. Fujikawa, H. Tanaka, K. Oguro, J. Electrochem. Soc. 2009, 156, B509 – B512.

62. K. Asazawa, K. Yamada, H. Tanaka, A. Oka, M. Taniguchi, T. Kobayashi, Angew. Chem. 2007, 119, 8170 – 8173; Angew. Chem. Int. Ed. 2007, 46, 8024 – 8027.

63. K. Yamada, K. Yasuda, T. Ioroi, N. Fujiwara, Z. Siroma, H. Tanaka, Y. Miyazaki, T. Kobayashi, Electrochem. Commun. 2003, 5, 892 – 896.

64. K. Yamada, K. Yasuda, T. Ioroi, H. Tanaka, Y. Miyazaki, T. Kobayashi, J. Power Sources 2003, 122, 132 – 137.

65. K. Yamada, K. Asazawa, K. Yasuda, T. Ioroi, H. Tanaka, Y. Miyazaki, T. Kobayashi, J. Power Sources 2003, 115, 236 – 242.

66. A. Serov, C. Kwak, Appl. Catal. B 2010, 98, 1–9.

67. A. Serov, U. Martinez, A. Falase, P. Atanassov, Electrochem. Commun. 2012, 22, 193 – 196.

68. S. Pylypenko, S. Mukherjee, T. S. Olson, P. Atanassov, Electrochim. Acta 2008, 53, 7875 – 7883.

69. M. H. Robson, A. Serov, K. Artyushkova, P. Atanassov, Electrochim. Acta 2013, 90, 656 – 665.

70. S. Brocato, A. Serov, P. Atanassov, Electrochim. Acta 2013, 87, 361 – 365.

71. A. Serov, M. H. Robson, K. Artyushkova, P. Atanassov, Appl. Catal. B 2012, 127, 300 – 306.

72. A. Serov, M. H. Robson, M. Smolnik, P. Atanassov, Electrochim. Acta 2012, 80, 213 – 218.

73. A. Serov, M. H. Robson, B. Halevi, K. Artyushkova, P. Atanassov, Electrochem. Commun. 2012, 22, 53 – 56.

74. A. Falase, M. Main, K. Garcia, A. Serov, C. Lau, P. Atanassov, Electrochim. Acta 2012, 66, 295 – 301.

75. A. Serov, U. Martinez, P. Atanassov, Electrochem. Commun. 2013, 34, 185 – 188.

76. A. Serov, M. H. Robson, M. Smolnick, P. Atanassov, Electrochim. Acta 2013, 109, 433 – 439.

77. A. Serov, A. Aziznia, P. H. Benhangi, K. Artyushkova, P. Atanassov, E. Gyenge, J. Mater. Chem. A 2013, 1, 14384 – 14391.

78. A. Serov, K. Artyushkova, P. Atanassov, Adv. Energy Mater. 2014, DOI: 10.1002/aenm.201301735.

79. P. S. Ruvinskiy, A. Bonnefont, C. Pham-Huu, E. R. Savinova, Langmuir 2011, 27, 9018.

80. P. S. Ruvinskiy, A. Bonnefont, M. Bayati, E. R. Savinova, Phys. Chem. Chem. Phys. 2010, 12, 15207.

81. A. Schneider, L. Colmenares, Y. E. Seidel, Z. Jusys, B.Wickman, B. Kasemo, R. J. Behm, Phys. Chem. Chem. Phys. 2008, 10, 1931.

82. P.-Y. Olu, C. Barros, N. Job, M. Chatenet, Electrocatalysis 2014, 5, 288 – 300.

83. K. S. Freitas, B. M. Concha, E. A. Ticianelli, M. Chatenet, Catal. Today 2011, 170, 110.

84. J. L. Gland, G. B. Fisher and G. E. Mitchell, Chem. Phys. Lett., 1985, 119, 89–92.

85. P. A. Giguere and I. D. Liu, J. Chem. Phys., 1952, 20, 136–140.

86. T. Tipton, D. A. Stone, K. Kubulat and W. B. Person, J. Phys. Chem., 1989, 93, 2917–2927.

87. H. D. Kaesz and R. B. Saillant, Chem. Rev., 1972, 72, 231–281.

88. T. Yoshida, K. Kojima, The Electrochemical Society Interface, 24 (2015) 45-49.

89. J. R. Varcoe, P. Atanassov, D. R. Dekel, A. M. Herring, M. A. Hickner, P. A. Kohl, A. R. Kucernak, W. E. Mustain, K. Nijmeijer, K. Scott, T. Xu, L. Zhuang, Energy Environ. Sci., 7 (2014) 3135-3191.

90. B. P. Setzler, Z. Zhuang, J. A. Wittkopf, Y. Yan, Nature Nanotechnology 11 (2016) 1020–1025.

91. A. Serov, N. I. Andersen, Sadia A. Kabir, A. Roy, T. Asset, M. Chatenet, F. Maillard, P. Atanassov, J. Electrochem. Society, 162 (12) (2015), F1-F5.

92. B. Britton, S. Holdcroft, J. Electrochem. Soc. 163 (2016) F353-F358.

93. E. H. Yu, X. Wang, U. Krewer, L. Lid, K. Scott, Energy Environ. Sci., 5 (2012) 5668-5680.

94. T. J. Omasta, X. Peng, C. A. Lewis, J. Varcoe, W. E Mustain, ECS Trans. 75, (14) (2016) 949-954.

95. J. Qi, N. Benipal, C. Liang, W. Li, Applied Catalysis B: Environmental 199 (2016) 494-503.

96. R. B. Kaspar, M. P. Letterio, J. A. Wittkopf, K. Gong, S. Gu, Y. Yan, J. Electrochem. Soc. 162 (2015) F483-F488.

97. S. Lu, J. Pan, A. Huang, L. Zhuang, J. Lu, PNAS 105 (2008) 20611–20614.

98. Q. Hu, G. Li, J. Pan, L. Tan, J. Lu, L. Zhuang, Int. Journal of Hydrogen Energy 38 (2013) 16264-16268.

99. R. Janarthanana, A. Serov, S. Kishore Pilli, D. A. Gamarra, P. Atanassov, M. R. Hibbs, A. M. Herring, Electrochim. Acta 175 (2015) 202-208.

100. M. G. Marino, K. D. Kreuer, ChemSusChem 8 (2015) 513 – 523.

101. H. A. Miller, A. Lavacchi, F. Vizza, M. Marelli, F. Di Benedetto, F. D'Acapito, Y. Paska, M. Page, D. R. Dekel, Angew. Chem. 128 (2016) 6108–6111.

102. M. Alesker, M. Page, M. Shviro, Y. Paska, G. Gershinsky, D. R. Dekel, D. Zitoun, J. Power Sources 304 (2016) 332–339.

103. A. Serov, T. Nedoseykina, O. Shvachko, C. Kwak, J. Power Sources 195 (2010) 175–180.

104. A. Serov, C. Kwak, Catal. Comm. 10 (2009) 1551–1554.

105. T. Asset, A. Roy, T. Sakamoto, M. Padilla, I. Matanovic, K. Artyushkova, A. Serov, F. Maillard, M. Chatenet, K. Asazawa, H. Tanaka, P. Atanassov, Electrochim. Acta 215 (2016) 420-426.

106. E. Antolini, Energy Environ. Sci. 2 (2009) 915-931.

107. A. Morozana, F. Jaouen, Energy Environ. Sci. 5 (2012) 9269-9290.

108. E. F. Holby, P. Zelenay, Nano Energy 29 (2016) 54–64.

109. K. Strickland, E. Miner, Q. Jia, U. Tylus, N. Ramaswamy, W. Liang, M.-T. Sougrati, F. Jaouen, S. Mukerjee, Nature Communications 6, Article number: 7343 (2015) doi:10.1038/ncomms8343.

110. A. Serov, M. J. Workman, K. Artyushkova, P. Atanassov, G. McCool, S. McKinney, H. Romero, B. Halevi, T. Stephenson, J. Power Sources 327 (2016) 557-564.

111. U.I. Kramm, A. Zana, T. Vosch, S. Fiechter, M. Arenz, D. Schmeisser, J. of Solid State Electrochemistry 20 (4) (2016) 969-981.

112. A. Serov, M. Min, G. Chai, S. Han, S. J. Seo, Y. Park, H. Kim, C. Kwak, J. Appl. Electrochem. 39 (2009) 1509–1516.

113. A. Serov, K. Artyushkova, N. I. Andersen, S. Stariha, P. Atanassov, Electrochim. Acta 179 (2015) 154-160.

114. A. Serov, K. Artyushkova, E. Niangar, C. Wang, N. Dale, F. Jaouen, M.-T. Sougrati, Q. Jia, S. Mukerjee, P. Atanassov, Nano Energy, 16 (2015) 293-300.

115. J. Durst, A. Siebel, C. Simon, F. Hasché, J. Herranz, H.A. Gasteiger, Energy Environ. Sci. 7 (2014) 2255-2260.

116. M. C. Biesinger, B. P. Payne, L. W. M. Lau, A. Gerson, R. St. C. Smart, Surface and Interface Analysis 41(4) (2009) 324-332.

117. J. Haetge, I. Djerdj, T. Brezesinski, Chem. Comm. 48 (2012) 6726-6728.

118. S. Kasztelan, J. Grimblot, J.P. Bonnelle, E. Payen, H. Toulhoat, Y. Jacquin, Appl. Cat. 7 (1983) 91-112.

119. Z. Zhang, Y. Liu, Z. Huang, L. Ren, X. Qi, X. Wei, J. Zhong, PCCP 17 (2015) 20795-20804.

120. J. Baltrusaitisa, B. Mendoza-Sanchez, V. Fernandez, R. Veenstra, N. Dukstiene, A. Roberts, N. Fairley, Appl. Surface Science 326 (2015) 151-161.

121. D. O. Scanlon, G. W. Watson, D. J. Payne, G. R. Atkinson, R. G. Egdell, D. S. L. Law, J. Phys. Chem. C 114 (2010) 4636-4645.

122. S. A. S Machado, L. A. Avaca, Electrochim. Acta 39 (1994) 1385-1391.

123. A. G. Oshchepkov, A. Bonnefont, V. A. Saveleva, V. Papaefthimiou, S. Zafeiratos, S. N. Pronkin, V. N. Parmon, E. R. Savinova, Topics in Catalysis 59 (2016) 1319-1331.

124. S. S Singh, Jason J. Williams, P. Hruby, X. Xiao, F. De Carlo, N. Chawla, Integrating Materials and Manufacturing Innovation 3(1) (2014) 1-14.

125. W. Sheng, H. A. Gasteiger, Y. Shao-Horn, J. Electrochemical Society 157 (2010) B1529-B1536.

126. Z. Zhuang, S. A. Giles, J. Zheng, G. R. Jenness, S. Caratzoulas, D. G. Vlachos, Y. Yan, Nature communications 7 (2016).

127. W. Sheng, Adam P. Bivens, M. Myint, Z. Zhuang, R. V. Forest, Q. Fang, J. G. Chen, Y. Yan, Energy & Environmental Science 7 (2014) 1719-1724.

128. J. Zheng, S. Zhou, S. Gu, B. Xu, Y. Yan, Journal of The Electrochemical Society 163, no. 6 (2016) F499-F506.

129. J. Greeley, T. F. Jaramillo, J. Bonde, I. B. Chorkendorff, J. K. Nørskov, Nature materials 5 (2006) 909-913.

130. Sene, Frank Ferrer, & Motta, Cláudio Costa. (2013). *Materials Research*, *16*(2), 417-423. Epub February 08, 2013.https://dx.doi.org/10.1590/S1516-14392013005000019

131. W. Sheng, M. Myint, J. G. Chen, Y. Yan, Energy & Environmental Science 6 (2013) 1509-1512.

132. S. Marini, P. Salvi, P. Nelli, R. Pesenti, M. Villa, Y. Kiros, Int. J. Hydrogen Energy 38 (2013) 11484-11495.

133. R. Solmaz, A. Döner, G. Kardaş, Electrochemistry Communications 10 (2008) 1909-1911.

134. A. G. Oshchepkov, P. A. Simonov, O. V. Cherstiouk, R. R. Nazmutdinov, D. V. Glukhov, V. I. Zaikovskii, T. Y. Kardash, R. I. Kvon, A. Bonnefont, A. N. Simonov, V. N. Parmon, E. R. Savinova, Topics in Catalysis 58 (2015) 1181-1192.

135. P. Quaino, G. Belletti, S. A. Shermukhamedov, D. V. Glukhov, E. Santos, W. Schmickler, R. Nazmutdinov, Phys. Chem. Chem. Phys. 19 (2017) 26812-26820.

136. Z. Zhuang, S. A. Giles, J. Zheng, G. R. Jenness, S. Caratzoulas, D. G. Vlachos, Y. Yan, Nature Communications. 7 (2016) 10141.

137. L.-k. Tsui, F. Garzon, Journal of Applied Crystallography 50 (2017).

138. H. Shi, J. N. Reimers, J. R. Dahn, J. Applied Crystallography. 26 (1993) 827-836.

139. C. R. Houska, B. E. Warren, Journal of Applied Physics 25 (1954) 1503-1509.

140. P. Quaino, F. Juarez, E. Santos, W. Schmickler, Beilstein Journal of Nanotechnology 5 (2014) 846-854.

141. O. A. Petrii, G. A. Tsirlina, Electrochimica Acta 39 (1994) 1739-1747.